Theoretical Probe to the Mechanism of Pt-catalyzed C-H Acylation Reaction: Possible

Pathways for the Key Acylation Reaction of Platinacycles

By

Elizabeth Fae Warden

December 2019

Director of Thesis: Dr. Yumin Li

Major Department: Chemistry

Transition metal-catalyzed C-H bond functionalization offers a variety of desirable transformations of simple hydrocarbons to more complex compounds with applications being applied in pharmaceuticals to material sciences. In 2017, Dr. Huo's research group reported a unique Pt-catalyzed acylation of 2-aryloxypyridines through direct C–H activation. The significance of this reported reaction is represented in the experiment occurring without any oxidants or additives; furthermore, presenting this relatively straight forward reaction mechanism which is initiated only in the presents of platinum. However, through computational analysis the key acylation step of the cyclometalated platinum complex has shown quite intriguing results. Utilization of the nudged elastic band (NEB) method followed by a min-mode optimization of the potential transition states has shown preference towards a nucleophilic substitution over the previously proposed electrophilic addition during the key acylation step. Theoretically, this DFT study at M062X/6-311g**/def2-TZVP-Pt level of theory was unable to simulate the initial formal electrophilic substitution reaction proposed as the arenium ion **C** could not be minimized. Therefore based on current results the preferred pathway is as follows: (1) nucleophilic substitution of the acyl chloride to form five-coordinate acylplatinum complex with a barrier of 21.7083 k

cal/mol (**B**), followed by (2) 1,2-migration of the acyl group from the platinum to the

metalated carbon to form a Pt-arene η2-complex or platinacyclopropane with a barrier of

15.0713 kcal/mol (**E**). Lastly, (3) Re-aromatization of **E** leads to the acylated product **P** with a

barrier of 35.3138 kcal/mol. Further probing and key mechanistic results will be presented.
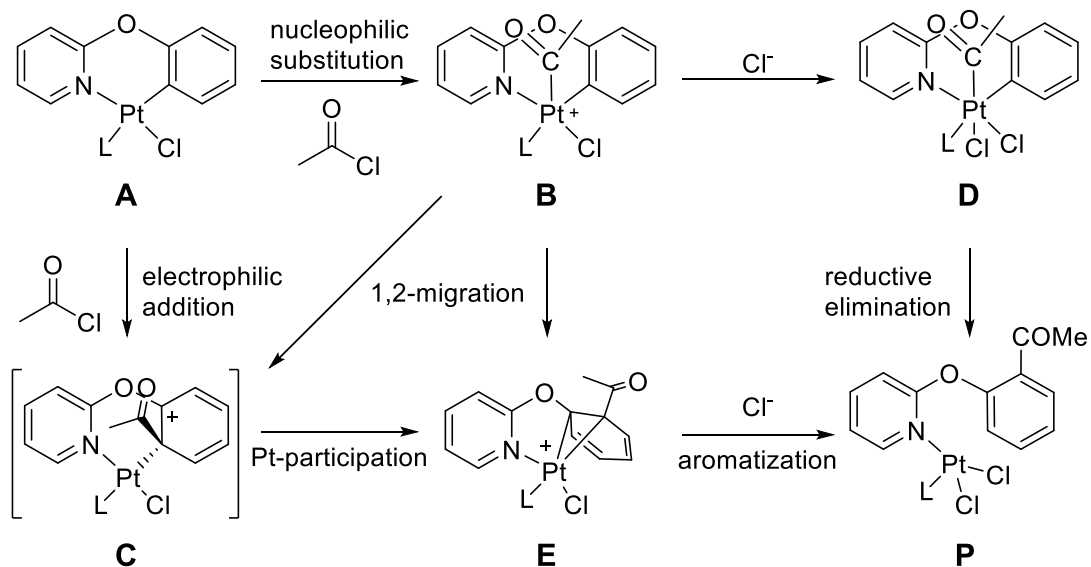
Proposed pathways for the acylation of complex A (L= acetonitrile).

Theoretical Probe to the Mechanism of Pt-catalyzed C-H Acylation Reaction: Possible

Pathways for the Key Acylation Reaction of Platinacycles

A Master's Thesis

Presented to the Faculty in the Department of Chemistry

East Carolina University

In Partial Fulfilment of the Requirements for the

Master's of Science Degree in Chemistry

by

Elizabeth Fae Warden

December 2019

Theoretical Probe to the Mechanism of Pt-catalyzed C-H Acylation Reaction: Possible

Pathways for the Key Acylation Reaction of Platinacycles

by

Elizabeth Fae Warden

APPROVED BY:

DIRECTOR OF
THESIS:_____
                                   Yumin Li, PhD

COMMITTEE MEMBER:_____
                                   Libero Bartolotti, PhD

COMMITTEE MEMBER:_____
                                   Shouquan Huo, PhD

COMMITTEE MEMBER:_____
                                   Baohong Zhang, PhD

CHAIR OF THE DEPARTMENT
OF CHEMISTRY:_____
                                   Andrew Morehead, PhD

DEAN OF THE
GRADUATE SCHOOL:_____
                                   Paul J. Gemperline, PhD

TABLE OF CONTENTS

LIST OF TABLES

LIST OF FIGURES

LIST OF SCHEMES

CHAPTER 1: INTRODUCTION AND BACKGROUND

1.1   C-H Functionalization

Activation/functionalization of the ubiquitous Carbon-Hydrogen bond into other functionalities is highly attractive field of study for organic syntheses in current studies.[1-4] Transformation of these C-H bonds gives way to new carbon-carbon or carbon-heteroatom bonds. Descriptively, the term functionalization encompasses the activation step. Activation is associated with the initial step of cleaving the C-H bond by formation of a carbon-metal bond, where the metal is a transition metal. The C-M bond then transforms into a C-X bond, where X denotes any functional group. This two-step process is coined C-H functionalization.
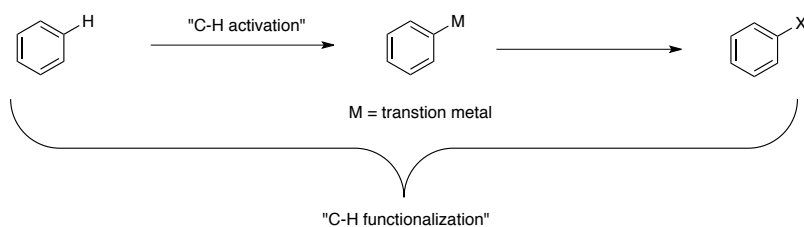
Scheme 1. C-H Functionalization visualization through a simple two step approach.

Often C-H functionalization mechanisms are mistakenly grouped with *Friedel-Crafts* alkylation or acylation. FC mechanisms are not C-H activation reactions, but in actuality defined as electrophilic aromatic substitution (EAS) mechanisms. Both mechanisms transform C-H bonds into C-C bonds, however the FC mechanism for the C-H cleavage does not require any activation. In EAS reactions, the C-H cleavage occurs after the substitution takes place on the arene ring, which in-turn shows the cleavage being driven by the aromatization. The C-H activation will either show cleavage of the C-H bond before or in the concerted pathway of arene-metal sigma bond formation.

1.1.1 Importance of C-H Functionalization

The selective conversion of inert C–H bonds found in alkanes and arenes into new functional groups is a powerful strategy for rapidly increasing the complexity of organic molecules.[6] C-H activation can tolerate highly functionalizing groups, which is enticing for efficient synthesis of molecules applicable in numerous drugs and natural products.[7] Not to mention the abundancy of simple hydrocarbons leading to the immense desire to easy convert these bonds into higher functionality at lower synthetic costs.

Methane functionalization is a prime example of why C-H activation is in high demand. To convert methane directly into methanol, one would be able to easy access methane as it is the primary component in natural gas, and much cheaper to obtain rather than buying methanol directly. Plants produce methane naturally, the challenge arising with this source would begin with isolating methane from ethane and propane which is secondary components in natural gas. Advancing past gas separation, methane functionalization to methanol is driven by C-H activation. The initial synthetic success from Shilov's group made the break through into the C-H activation field via methane activation, and only recently has this field become such a strongly sought out area for synthetic chemists who aim to obtain highly desirable functionalized complexes from abundant hydrocarbon systems. However, there are still numerous hurdles to overcome, especially in relations to the energy barriers associated with cleaving C-H bonds.

1.1.2 Challenges Associated with C-H Functionalization

Typical C-H bonds have large bond dissociation energy's that previously presumption these bonds as potentially inert. As shown in the table below, the bond dissociation energy of a H-CH$_3$

bond is 105 kcal/mol and a C-C bond in ethane is a drastic 15 kcal/mol lower. However,

cleavage of this bond was first reported and attributed to Joseph Chatt in 1965 for the first C-H

activation reaction. The advances were further pioneered by research groups tackling C-H bond

cleavage by the use of stoichiometric amounts of the transition metal catalysts alongside a large

number of reviews on the fundamental features involved.[8-9] Further elucidation into the fine-

tuned details of this mechanism are still unanswered.

The biggest challenge, as validated by the bond dissociation energies below, prevails from

the daunting energy barrier associated with C-H bond cleavage reactions. Most C-H bonds are

stronger than their corresponding C-X bonds.[10] Therefore, C-H functionalization is classified as

thermodynamically unfavorable. The activation barrier must be lowered and in doing so the

initiation of a transition metal is required.

Table 1. Specific C-H, C-X Bond Dissociation Energies.

Bond	Bond Strength (in kcal/mol)	Bond	Bond Strength (in kcal/mol)
C_{Methyl}-H	105	C-C (in ethane)	90
$C_{Isopropyl}$-H	99	C-O (in MeOH)	92
$C_{tertbutyl}$-H	97	C-N (in $MeNH_2$)	85
C_{allyl}-H	89	C-F (MeF)	115
C_{phenyl}-H	113	C-Cl (MeCl)	84
HCC-H (ethyne)	133	C-Br (MeBr)	72
		C-I (MeI)	58

Upon successful functionalization of the C-H bond, a new C-X bond is formed. However,

formation of C-X bonds is easier to further breakdown due to their lower bond strength. The

weaker C-X bonds are at risk for overreactions, as seen through catalytic inhibition. To adhere to

this concern, the topic of internal oxidants as directing groups has been recently reviewed.[11] In

addition to continuous reactions potentially occurring, the new C-X bond might change the

reactivity of the molecule. Altercations to aromaticity could be observed by the electron density

shift, which in turn could disorient ring formations or induce further overreactions.

An additional concern in using naturally abundant hydrocarbons is associated with their saturation. Most molecules, especially simple hydrocarbons, contain numerous C-H bonds of varying types. Therefore, the challenge of regioselectivity comes into play by employing a catalyst that will target the desired C-H bond solely for activation. In addition to catalyst choice, the site of activation may lead to another hurdle to overcome.

Stereoselectivity must be achieved in C-H functionalization mechanisms to avoid formation of stereogenic centers. Stereoisomers, especially in drug development, play a crucial role. Molecules of the same chemical formulas but vary by one spatial arrangement can perform drastically different functions in the body. Therefore, synthetic mechanisms must not only activate the desired C-H bond but yield the desired stereoisomer as well.

1.2 Transition Metal Catalysts

The transition metal catalyst is heavily involved throughout each stage of a C-H functionalization. They are broken down into two different categories based on the C-H cleavage mechanism.[12] Robert Crabtree distinguished these approaches being either coordination or organometallic chemistry. Which was further labeled as "outer-sphere" or "inner-sphere" mechanism by Melanie Sanford.[13] In the outer sphere mechanism the electron transfer occurs between complexes that do not undergo substitution, therefore no new bonds are broken or formed. Inner sphere mechanism aims to break and form new bonds by electron transfer between complexes through a bridging ligand. The ligand must be labile for this bridging to occur.

a. Outer-sphere mechanism/coordination chemistry

[C-H insertion]

[M]=X

[M]

X

[M]=X

H–C

[M]=X···H C

Functionalization

H–X–C

[M]

[M]–X··C H

[H atom abstraction/rebound]

- Reacts preferentially with weaker C-H bonds (tertiary, benzylic, allylic, α to heteroatoms>secondary>primary)
- No direct interaction between **[M] center** and **C-H** bonds

----

b. Inner-sphere mechanism/organometallic chemistry

[M]

X

H–C

[M]–C

X–C

C-H bond cleavage

[M]

Functionalization

- Reacts preferentially with primary>secondary>tertiary C-H bonds
- C-H bond cleavage results in the formation of a **C-[M]** bond

Scheme 2. Different approaches for the transition-metal catalyzed C-H functionalization.

In the outer sphere mechanism in **scheme 2a**, the alkane will first interact with a highly-activated ligand of a metal complex (X= carbene[14], nitrene[14c,15], oxene[5]) before the C-H bond functionalization occurs. This first initial interaction forms a precursor complex. Activation/reorganization of the precursor complex can proceed through a C-H insertion mechanism or by a H atom abstraction/radical rebound. In this step the electron transfer occurs without the formation of a metal-alkyl intermediate to a successor complex that quickly dissociates to the functionalized product. Both mechanisms show preference towards weaker C-H bonds (tertiary>secondary>primary) due to the radical and/or cationic character at the carbon center.

Following the organometallic approach, in the inner sphere mechanism the C-H bond cleavage forms a C-M intermediate that reacts to create the functionalized product. The Shilov mechanism shown in **scheme 2b** is initiated first by the C-H activation step. Activation proceeds by an agnostic interaction between the metal center and the C-H bond via either oxidative

addition (OA) or concerted metalation deprotonation (CMD), which leads to the formation of the activated organometallic complex.[12,5,6,2] The selectivity of the C-H bond trend is opposite as seen for the outer sphere mechanism, where preference is seen as C(sp2) H > primary > secondary > tertiary. Explanation as to why can be partially evaluated based on the basicity of the C-H bond to activate.[17] Transition metal-catalyzed C(sp2)-H bond activation are often favored over C(sp3)-H bonds, which is aligned with acidity of aromatic and vinyl protons being higher than aliphatic protons. On the contrary to C (sp2)-H preference, the C (sp3)-H bonds lack π-electrons which allows the π-metal pre-coordination to lower the energy barrier for the C-H activation step. Selectivity based on these two effects create a more challenging process for synthetic development of a transition metal to catalyze C (sp3)-H bonds during activation.[18]

1.2.1 Platinum Catalysts

Platinum has played a significant role in the advancements in C-H activation and functionalization chemistry.[19] The first well-defined example of intermolecular C-H activation catalyzed by Pt (II) was reported by Garnett and Hodges in 1967.[20] In this mechanism, the transition metal catalyzed the H/D exchange of arenes in an aqueous acetic acid. Often this groups work is denoted as a more trivial form of C-H activation, but has been classified as a functionalization stepping stone years later through experimental expansion seen by Shilovs group in 1969.[5,21]
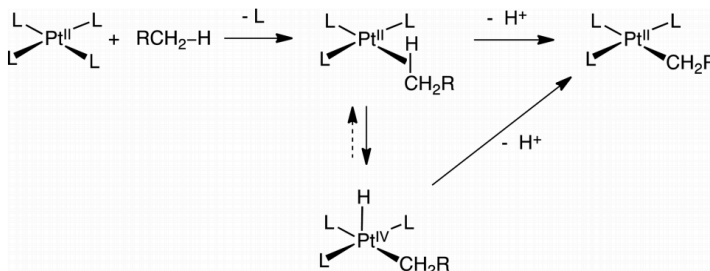
Scheme 3. Shilov Mechanism: Catalytic homogeneous alkane oxidation with Pt (II) complexes.

In **scheme 3**, the mechanism is proposed to initiate through an interaction of the Pt (II) complex to give an alkane-Pt complex (σ-complex). Moving forward, the C-M complex will follow a step-wise redox route or a straight forward non-redox route. In the redox pathway the Pt (IV) alkyl hydride complex is formed vis oxidative addition followed by proton loss. Through the nonreduction route the proton is lost directly from the Pt (II) σ-complex. However, a variation of this could involve the interaction between the leaving group on the initial Pt (II) complex (L) and the hydride denoted as a σ-complex-assisted metathesis (σ-CAM). To distinguish which route is actually occurring is not straightforward as the observed Pt (IV) hydride isn't necessarily an actual intermediate in the C-H activation since its shown as reversible in **scheme 3**. Computational tools have been sought out for application towards clearly distinguishing the exact mechanistic steps.[22]

As remarked above, advances in C-H activation studies began roughly 50 years ago. Key advances in this field has heavily relied on Pd-catalyst functionalization's. Research involving the Pt-catalyzed mechanistic studies are rarely published, the few examples presented should not set aside platinum as a weaker catalyst. In fact, Pt chemistry offers advantages for systematic investigations in the mechanistic features.

1.2.2 Intramolecular C-H Functionalization

C-H activation can be broken down into two main categories: intermolecular and intramolecular C-H activation. Our study will focus on intramolecular C-H activation, also referred to as cyclometalation, which is schematically represented below (**scheme 4**).
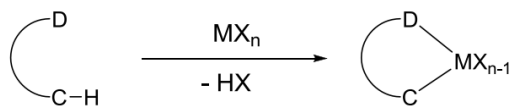
D = donor atom such as N, O, S, and P

Scheme 4. Schematic representation of intramolecular C-H activation.

The cyclometalated products from the intramolecular activation step can be isolated for characterization, and in turn confirm mechanistic steps. Typically intermediates obtained in C-H activation involve agostic complexes. Agostic interactions seen intramolecular activation display chelation stabilization for the unsaturated metal centers, which allow full isolation and characterization.[23,24]

Crepso and Love have reported extensive work involving cyclometalation of imines and other N-centered ligands.[25,26] There focus lied on determining the factors revolving around the regioselectivity in C-H activation.
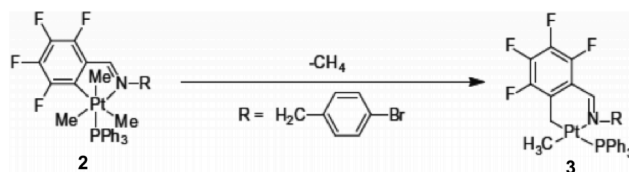
Scheme 5. Reproduced mechanism from Love's mechanistic studies.

In **scheme 5**, the depicted mechanism shows regioselectivity issues. The C-C bond formation beings with the imino-phenyl-Pt (IV) complex **2**, which slowly transforms to a Pt (II) complex **3** at room temperature in solution. The proposed stepwise involves the C(phenyl)-C(methyl) reductive elimination which is followed up by C-H activation at the benzylic position with latter methane loss. Activation of the sp^3 C-H bond to form the Pt (IV) complex must occur over activation of the ortho-sp^2 C-H bond in the imine substituent R, which would produce a five-

membered ring. Favoritism for the six-membered ring resulted from endo-metallacycle preferred over exo-metallacycle, where the C=N bond lies inside the chelate ring, in imine cyclometalations. Alternative preference could be argued for the C-F bond to activate based on an endo, five-membered ring formation, though this was not the observed preference.
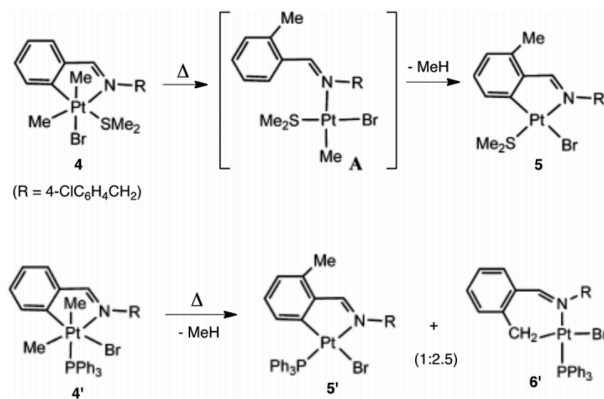
Scheme 6. Crepso Pt (IV) mechanism reproduced for studies.

A similar sequence studied in Crepso's laboratory is shown in **scheme 6**. Following the mechanism, Pt (IV) complex **4** converts to **5** by C-C reductive elimination producing intermediate **A**, which further actives the C-H bond prior to loss of methane. Pt (IV) complex **4** was refluxed in toluene to convert to **5**. The key difference from the previously discussed mechanism in scheme 4 is that the ortho-sp^2 C-H bond of the tolyl group is activated. Modifications to complex **4**, however, display a 1:2.5 mixture of sp^2 versus sp^3 activation. Replacement of the SMe2 with PPh3 and simultaneously joined with isomerization, leads to complex **4'**. The same experimental procedures were applied to complex **4'**, however the mixture of products **5'** and **6'** yield from sp^2- and sp^3- C-H activation. The product mixture yielded a ratio of 1:2.5, implicating the preference towards sp^3- C-H activation occurring from one ligand modification. The cyclometallation pathway clearly is heavily dictated by ligand effects as well

as factors such as aliphatic vs aromatic, the size of ring formation, and the energetics of the reaction coordinates.

1.3   Theoretical Studies on Platinum-Catalyzed C-H Functionalization Reactions

The fundamental steps in metal-centered reactions are observed during the transformation of the activated complex to the final product, which often follows an oxidative-addition/reductive elimination pathway.[27] The catalyzed functionalization of alkanes studied by the Shilov group was later employed under a computational study by Zhu and Ziegler.[22b] A density functional theory (DFT) was applied to investigate the rate-determining step (RDS) in which $PtCl_4^{2-}$ catalyzed the H-D exchange of alkanes in acidic aqueous solution. Their DFT analysis was based on the Becke–Perdew exchange-correlation functional, using the Amsterdam density functional (ADF) program. The basis set incorporated was the standard double-ζ STO bases with one set of polarization functions applied to H, N, and O atoms, and the standard triple-ζ basis sets for the Cl and Pt atoms. Computational studies were done to investigate the C-H activation and the methane uptake for assay in the RDS in the Shilov reaction. The possible mechanisms of methane uptake were examined as occurring either by a dissociative or associative mechanism. In the dissociative mechanism (**scheme 7**), the platinum complex loses one ligand first followed by methane's replacement at the leaving group site. On the other hand, in the associative mechanism (**scheme 8**), the leaving ligand and incoming methane are occurring simultaneously. This pathway forms a distorted trigonal-bipyramidal transition state that follows the ligand cleavage and product formation.
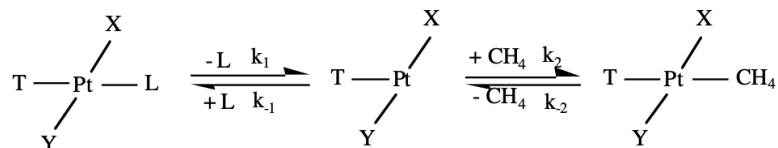
Scheme 7. Dissociative mechanism for the uptake of methane by a square planar platinum complex.
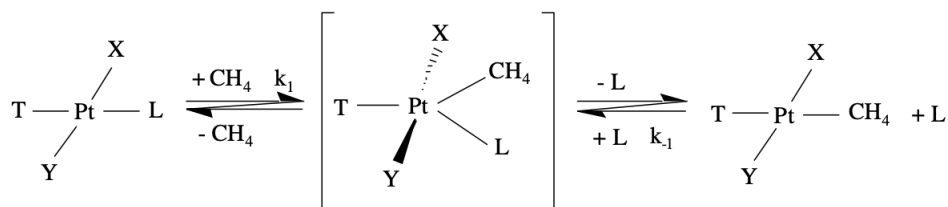
Scheme 8. Associative mechanism for the uptake of methane by a square planar platinum complex.

Their concluding results presented the RDS as the methane uptake step in the Shilov reaction. Both the dissociative and associative mechanisms were investigated, and they remarked that the dissociative mechanism favored slightly. However, they were unable to exclude the possibility that the associative mechanism was at play due to uncertainties in their calculated contributions in the free energies for the activation seen in both the entropy and solvation.

Hill and Puddephatt preformed a theoretical assay on the mechanism of methylplatinum complexes involved in the C-C and C-H bond formation and activation.[28] Their study honed into investigating the reductive eliminate (**scheme 9-10**) of methane or ethane from a five-coordinated intermediate ($[PtHMe_2L_2]^+$, or $[PtMe_3L_2]^+$) and the corresponding C-C or C-H bond activation in the alkane complexes ($[PtMe(CH_4)L_2]^+$ or $[PtMe(C_2H_6)L_2]^+$) by applying both an extended Huckel molecular orbital (EHMO) and DFT calculations using $L = NH_3$ and PH_3. In their DFT study, all calculations were performed at a B3LYP level with a LANDL2DZ basis set using a Gaussian-94 package. Their DFT results concluded that the C-H reductive elimination and oxidative addition were much easier than C-C reductive elimination and oxidative addition.

11

However, the activation energies for both C-H and C-C reductive elimination were the same for both ligands. The platinum (IV) complexes were more stable when L = NH₃, which showed higher activation energies for the oxidative addition step but not for the platinum (II) alkane complexes. In these Pt (IV) complex, either L being cis or trans were more stable in a square planar or pinched trigonal-bipyramidal conformation. All platinum (II) complexes were more stable in their trans form. Interestingly, this group reported the oxidative-addition/reductive-elimination reactions followed a concerted mechanism.
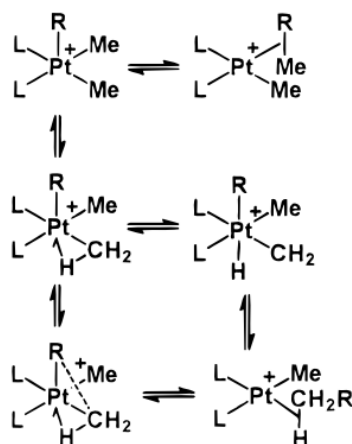
^a R = H or Me.

Scheme 9. Complexes of the type [PtMe₂(R)XL₂] (R = Me, H; X = Me, halide; L = neutral ligand or L₂ = chelating ligand) substrates for studying the Mechanisms of C-H and C-C bond reductive-elimination reactions from platinum (IV).

R
L\ |+ /Me
  Pt
L/ | \Me

1, L = NH$_3$, R = H
7, L = PH$_3$, R = H
13, L = NH$_3$, R = Me
17, L = PH$_3$, R = Me

→

     R
L\ + /
  Pt Me
L/   \Me

3, L = NH$_3$, R = H
9, L = PH$_3$, R = H
14, L = NH$_3$, R = Me
18, L = PH$_3$, R = Me

    Me
L\ |+ /R
   Pt
L/   \Me

2, L = NH$_3$, R = H
8, L = PH$_3$, R = H

     R
L\ + /
  Pt Me
L/   \L

4, L = NH$_3$, R = H
10, L = PH$_3$, R = H
15, L = NH$_3$, R = Me
19, L = PH$_3$, R = Me

→

      R
L\ + /
   Pt   Me
Me/   \L

6, L = NH$_3$, R = H
12, L = PH$_3$, R = H
16, L = NH$_3$, R = Me
20, L = PH$_3$, R = Me

    Me
L\ |+ /R
   Pt
Me/   \L

5, L = NH$_3$, R = H
11, L = PH$_3$, R = H
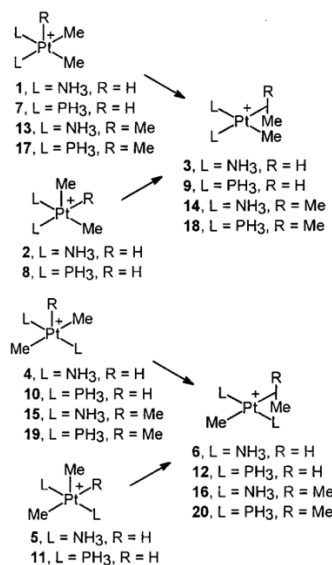
Scheme 10. Theoretical Studies input structures and their relationship to each other.

In the last decade, a computational study was performed on the mechanism and selectivity of the C-H bond activation and dehydrogenative functionalization in the synthesis of Rhazinilam.[29] Their study employed both M06 and B3LYP density functional approximation methods, with M06 using the 6-31G(d,p)/LANL2DZ-Pt basis sets in the Gaussian 09 ultrafine integration grid package and B3LYP was carried out in Gaussian 03 package. The study focused on simulation analysis in gaseous phase at 298 K, but their study additionally computed a solvation free energy assay for 2,2,2-trifluoroethanol with the IEFPCM-SDM solvent model. The reported asymmetric synthesis of (—)-Rhazinilam is presented in **scheme 11** followed by the energetic profile from the computational study in **figure 1**.
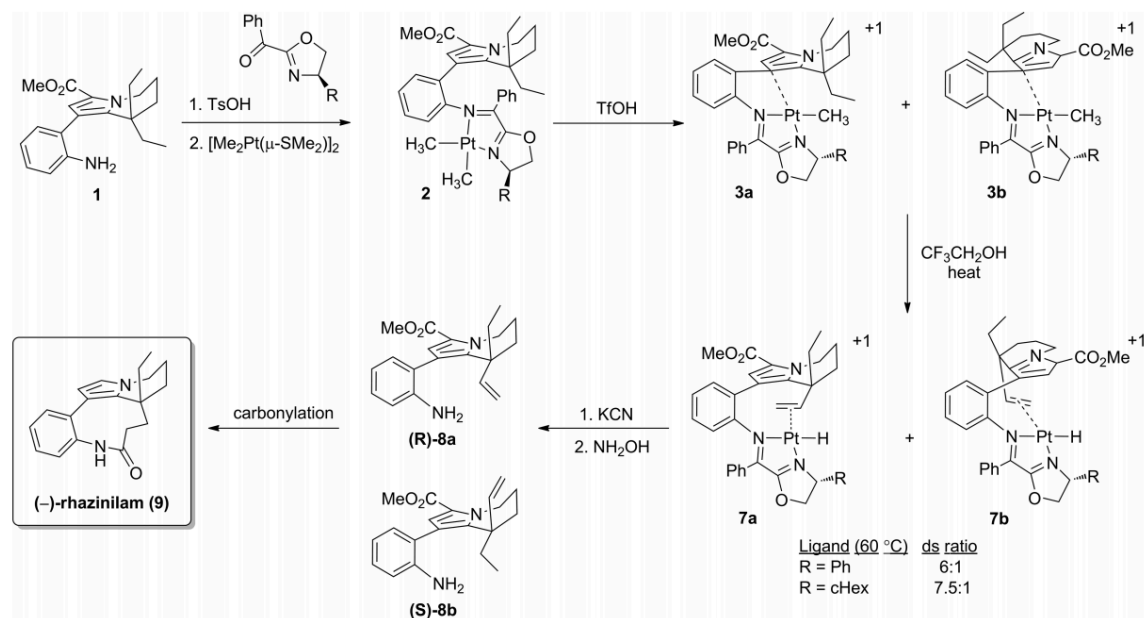
Scheme 11. M06 free energy (enthalpy) at 298 K profile.

From the full synthetic mechanism above, the computational study aimed to probe the mechanism and stereoselectivity in the conversion of the methyl platinum complexes **3a**, **b** into the platinum hydrides **7a**, **b.** The diastereomers **3a**, **b** were generated from protonation of complex **2** through an η-1 coordination of the pyrrole ring and the platinum metal center. Their basis set comparison on **3a**, **b** optimized structures energies displayed the same trends but with a slightly larger margin of error for the B3LYP functional.

14
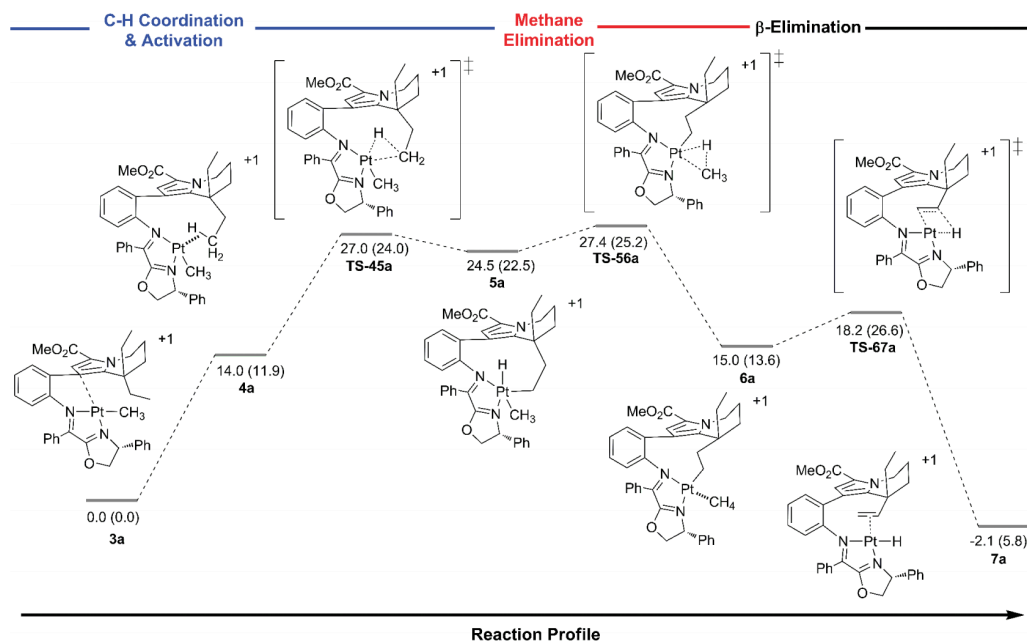
Figure 1. M06 energy profile at 298 K.

Following the mechanistic steps in the energy profile of **figure 1** displayed the research groups overall step-wise assay of the C-H activation of Rhazinilam. The initial activation begins with complex **3a**, when the pyrrole ligand dissociates from Pt to open a site for the C-H bond coordination. The favored agnostic C-H interaction resulted in complex **4a**, which then was probed for the most favorable transition state C-H bond cleavage either through insertion (oxidative addition) or σ-bond metathesis. The lowest energetic transition state, **TS-45a**, followed the insertion (oxidative addition) mechanism of the primary C-H bond in preference to activation of the secondary methylene C-H bond.[30] The short downhill decline from **TS-45a** to intermediate **5a** resulted from a C-H insertion that oxidized Pt(II) to a Pt(IV) complex. The Pt(IV) complex undergoes methane reductive elimination through **TS-56a**, which produced the methane coordination complex **6a**. Methane dissociates in **6a** to open a coordination site to platinum through **TS-67a**, which followed a methylene C-H bond β-hydride elimination to result

15

in the desired alkene platinum hydride complex **7a**. Their DFT study showed both the rate and selectivity determining step are seen during the methane elimination.

Investigation into previous mechanistic studies of platinum C-H functionalization reactions through utilization of the nudged elastic band (NEB) method were unable to be obtained from numerous databank searches. Several studies of alternative transition metal catalyst involved in predominately the activation step of C-H functionalization were found, but a rare few looked into the transformation step of forming the C-C bond or their analysis of the second step was brief.

CHAPTER 2: METHODOLOGY

2.1 Computational Chemistry

Computational chemistry is a set of techniques used to investigate chemical problems on a computer system. Commonly investigations include molecular geometries, energies of molecules and transition states, reactivity, and physical properties such as absorption or IR. A number of tools are available for computational chemist, and are often branched into two main views: (1) The classical mechanics approach which focuses on the macroscopic phenomena dealing with the ball and stick style assay, and the (2) Quantum – ab initio – mechanical approach which is used to explain the microscopic phenomena in terms of photon-atom interaction and the flow of electrons.[1]

As computational techniques continue to advance, the impact seen by theoretical work has be noted in numerous Nobel Prizes such as in 1998 to John Pople and Walter Kohn[2], and in 2013 to Martin Karplus[3], Nichael Levitt[4], and Arieh Warshel[4]. A computer software simulation can validate or predict chemical behaviors, which in turn cut costs experimental, save time, and offer a more environmentally friendly waste disposal. While simulations offer advantages to visualize, optimize and predict experimental results, these methods involved in the computational process are approximations. Methods vary in accuracy, but also in computer costs. Approximations of higher accuracy can require more time and more computational resources (such as memory and processing power). Therefore the user must take into consideration their systems size, the available computational resources, and the time allotted to obtain results.

Smaller molecular systems are simulated under the quantum mechanical view, as their size prevails the computational resources available to obtain deeper insight at subatomic levels. Quantum mechanics presents several levels of theory; Such theories discussed will included

Hartree-Fock theory, density functional theory (DFT), and hybrid DFT theory. Each method (theory) presented overall goal is to provide the best approximation to the Schrödinger equation. All ab initio methods do not incorporate empirical information, but rather rely on the established laws of nature (Quantum Mechanics).[5] Noting the numerous advancements over the last few decades, molecular modeling tools have advanced in their capability of accurately predicting structures, energetics, reactivities and other properties of molecules. Different levels of theories result in more accurate solutions of the Schrödinger equation.

2.2 Schrödinger Equation

Why do we need to accurately approximate this equation instead of accurately solving it? Let's take a deeper look into the mathematics. Most commonly the Schrödinger equation is applied in a time-independent non-relativistic formalism,

$$E\, \Psi = \hat{H}\, \Psi \qquad (1.1)$$

where E is the total energy, Ψ is the wave function, and $\hat{H}$ is the Hamiltonian operator of the total energy.[36] The term psi is a multi-particle wavefunction of the spatial coordinates of the electrons and nuclei. The Hamiltonian operator is the operator associated with the observable energy, therefore it expresses all terms that contribute to the systems total energy.[37]

$$\hat{H} = \hat{T} + \hat{V} \qquad (1.2)$$

T operator indicates the kinetic energy portion, which is an additive of the individual electron and nuclei kinetic energy operators. V operator is associated with the potential energy. The potential energy adds in the repulsion and attraction displayed between nuclei and electrons.[37]

$$\hat{V} = \hat{V}_{nn} + \hat{V}_{ne} + \hat{V}_{ee} \qquad (1.3)$$

In these simplest mathematical forms lies our answer; The reason that the Schrödinger equation is so difficult to solve for molecular systems is due to the chemical nature of particle interactions. For all systems with more than 1 electron, this equation advances in its mathematics to account for all interactions possible, therefore requiring accurate approximating methods. Single electron systems, such as the hydrogen atom, are non-interacting particles. Without interactions, the electric potential of the molecular system only influences each particle separately, so the total energy (shown in equation 1.1) can be expressed as the sum of energies for each particle, and the total molecular wavefunction can be written as a product of the individual particle wavefunctions. Therefore, systems displaying 2 or more electrons must intake every interaction to provide an accurate total energy for the system. When the number of electrons and nuclei in a system increases, the number of interactions increases. Additional interactions must be equated into the mathematics for the Schrödinger equation, which increases the difficulty associated with these computations.

2.3   Born Oppenheimer Approximation (BOA)

The Hamiltonian Operator as shown above incorporates 5 energy terms to the total energy of a system. Mathematically it states that these particles are correlated, so no particle moves independently. The operator is operating on a many electron wave-function, which is a function of nuclear and electron coordinates: $\Psi(R,r)$, where R is the nuclear coordinates and r is the electron coordinates.[32] Since the operator incorporates terms to take in the coupling contribution, to reduce this math an approximation was made. In terms of weight, the mass of a nuclei is approximately two thousand times the mass of an electron, so nuclei are essentially

stagnant. This is what is known as the Born-Oppenheimer Approximation; where nuclei appear to be stationary in comparison to electrons.[38-40]

$$\hat{H}_{el}\ \Psi_{el} = E_{el}\ \Psi_{el} \tag{1.1.2}$$

The electronic Schrödinger equation shown above is the outcome of the born-oppenheimer approximation. The wavefunction is now separated into a nuclear wavefunction and an electronic wavefunction, which mathematically is presented as:

$$\Psi = \Psi_N\ \Psi_{el} \tag{1.4}$$

The original Hamiltonian operator contained 5 sub-operators for each energy contribution. Once the BOA is applied, it is reduced to an additive of only 3 of the energy terms.

$$\hat{H} = \hat{T}_n + \hat{T}_e + \hat{V}_{ne} + \hat{V}_{ee} + \hat{V}_{nn} \tag{1.2.1}$$

$$\hat{H} = \hat{T}_e + \hat{V}_{ne+} + \hat{V}_{ee} + \hat{V}_{nn} \tag{1.5}$$

Equation 1.2.1 shows how the two energy terms are broken down individually and combined for the original Hamiltonian operator. Equation 1.5 applies the BOA, giving the electronic Hamiltonian operator. The kinetic energy of the nuclei is approximately zero since they are considered stationary due to their size, and the potential energy of the nuclei attraction term is presented but considered constant.[41]

2.4 Hartree-Fock Theory

As noted previously, there are various ab initio computational methods, with the lowest level approximation method being the Hartree-Fock (HF) theory.[42-44] This theory relies on 3 key approximations: (1) Born-Oppenheimer Approximation, (2) Independent electron approximation[45], and (3) Linear Combination of Atomic Orbitals (LCAO) approximation[46].

Often named the self-consistent field (SCF) method, it incorporates a variational approach to approximating the Schrödinger equation.

The independent electron approximation is where the Hartree wavefunction is derived. This takes the many-electron wavefunction and breaks it down into a product of individual, non-interacting, one-electron wavefunctions. These individual one-electron wavefunctions are the molecular orbitals. Since the electrons are withheld from instantaneous interactions, the electrons feel the averaged field of all other electrons in the system. This approximation neglects electron correlation due to the use of only a single slater determinant that expresses the electronic configuration.[47-50] Neglection of this electron correlation can give data that largely deviates from experimental, but provides less costs in comparison to more detailed approximating methods.

All the single electron wavefunctions are known as basis functions. These functions are built by the LCAO approximation that are represented mathematically as a slater determinant.[51-52] This ensures the electrons are indistinguishable so therefore associated with every orbital. The wavefunction is antisymmetric with respect to permutations (1 and 2) of both the spatial coordinates and spin, which further abides with the quantum mechanics postulate in reference to the total wavefunction being antisymmetric. Single orbitals are anti-symmetrized through the use of the slater determinate. The Hartree-Fock theory results when the wavefunction is approximated by the slater determinate. The initial starting slater determinate is a guess, and through each iteration the weighted coefficients of the LCAO are varied until the resultant energy is minimized. The lowest energy solution is obtained after numerous iteration till convergence is met, with computational time being based on the basis function utilized.

The variational approach is based on the variational theorem that say "The energy determined from any approximate wavefunction will always be greater than the energy for the

exact wavefunction".[32] Therefore through each iteration, the mathematics takes into account that the Hartree-Fock wavefunction energy must be minimized to give a more reasonable "exact" wavefunction of the system. The process of continuous trial and error to approach the lowest energy is the SCF process. SCF convergence is met once the molecular orbitals are all consistent with one another.

Hartree-Fock theory discussed so far has neglected the spatial and spin part of the MOs. Each spatial orbital has two spin orbitals. If the spatial part of the spin orbitals are the same, the system is referred to as restricted. If the spatial part of the spin orbitals are different, the system is unrestricted. In unrestricted systems, spin-polarization is taken into account. This is the process where unpaired electrons perturb paired electrons, and therefore gives realistic spin densities. Closed shell systems can remain in the restricted zone, but if a system is actually open-shelled then the unrestricted HF method should be applied as it provides a better model for unpaired systems.

In this approximation the single determinate wavefunction of electrons that move in the presence of the averaging field of all other electrons leaves out the energy associated with electron correlation. The electron correlation is made up of 2 components: (1) dynamic correlation which is key for bond breaking processes and (2) static correlation which is important for systems with bond stretching and low-lying excited states. HF theory will never be able to model a wavefunction with this degree of energy contribution. Several other methods are available to calculate this key component though, such as DFT.

2.5   Basis Sets

Atomic orbitals are described by atom-centered functions known as basis functions.

Basis sets are the combination of these mathematical functions (basis functions) used to describe the linear combination which yields the molecular orbitals. These functions are typically centered on the nuclei, and have several basis functions to describe the electrons surrounding the atomic-nuclei. The larger the basis set, the better the approximation to the atomic orbitals which create a less restricted wavefunction. However, this pay off will have higher computational costs.

The simplest basis set contains the minimum number of basis functions to accommodate all of the electrons in the atom, known as the Slater-Type Orbital (STOs). STOs are exact wave-functions for hydrogen-like atoms in non-relativistic cases. To decrease the costly computing tools required for STOs, Gaussian-Type Orbitals (GTOs) were developed as a way to express a single STO. Minimal basis sets are more favorable based on computational expenses compared to their larger counterparts, but typically they are far less accurate.

Split-valence basis sets intact more accuracy by modeling each valence orbital by two or more basis functions that have different exponents. These basis sets allow for orbital size fluctuation that occurs in bonding. For example, there are double and triple split valence basis sets denoted as double-zeta and triple-zeta, respectively. The most common basis sets were attributed from the Pople group; the 3- 21G, 6-31G, and 6-311G basis sets. Modifications can be made to these methods to add polarization and diffuse functions. Polarization functions have higher angular momentum. For example 6-31G(d) or 6-31G* both denote the inclusion of d functions on heavy atoms, where as 6-31G(d, p) or 6-31G** both denote the inclusion of d functions on heavy atoms and p functions on hydrogen atoms. Diffuse functions allow for better modelling of systems that have weakly bound electrons such as anions and excited states. They include both one diffuse s and a set of diffused p orbitals to provide a more accurate representation of the electron distribution at a distance from the nucleus. Denotation of diffuse

functions in basis sets are denoted by one (+) or two (++) plus signs, or by the prefix aug-. For example, 6-31+G basis set has diffuse functions on the heavy atoms and 6-31++G which has diffuse functions on hydrogen atoms and heavy atoms.

Dunning and coworkers designed the correlation-consistent basis sets to increase basis sets size to further provide improved simulated results. Once post-HF methods were released, the basis sets available were unable to optimize methods which included electron correlation. These Correlation-consistent (cc) basis sets are optimized using configuration interaction (CI) singles and doubles (CISD) wavefunctions. CI methods are based on solving the non-relativistic Schrödinger equation within the BO-approximation for a multi-electron system. The basis set abbreviations are denoted as: cc-pVnZ, where n = D, T, Q, 5, etc. Taking the abbreviated name and expanding, correlation-consistent polarized valence "n"-zeta. Where n indicated the splitting as either double, triple, quadruple, and so forth. Often diffuse functions will be added onto these basis sets, such as maug-cc-pvtz, where "maug" represents a truncated diffuse function. "Correlation consistent" in this basis set type implies that the exponent and contraction coefficients were variationally optimized not only for HF calculations, but those including electron correlation such as DFT. Dunning's basis sets, in general, give superior results to those in Pople sets, but the payoff is the computational time.

2.5.1 Effect Core Potential and Relativistic Effects

As the complexity of the molecule expands to third row elements of the periodic table, the number of electrons found in each of those atoms, the calculation slows due to the number of two-electron correlation integrals.[31] One method presented to overcome this problem is to consider the average effect the core electrons have upon the valence electrons. The average core

effect is rendered its own operator called an effective core potential (ECP) or a pseudopotential. This method simulates the effect on the valence electrons of the atomic nuclei plus the core electrons. ECPs are known to give reasonable results for molecules with third-row and beyond atoms by simulation the electronic relativistic mass increase. Atoms of the third-row and beyond, especially transition metals, have more significant relativistic effects at play, thus, ECPs are suitable for these atoms.

As the atomic nuclear charge (Z) increases, electrons penetrating the nucleus (s electrons) increase in speed and due to relativistic effects, their mass increases too. The penetrating s electrons (and the rare case of p electrons) are in smaller orbitals as a result of this effect. Heavier atoms hold their s electrons tighter and shield nuclear charge from other electrons more effectively, which in turn leaves d and f electrons to be loosely held in larger orbitals. Roughly, this effect can show Z^2 as a result. Therefore, the ab initio calculation for the Schrödinger equation, which includes relativistic equations, must be corrected for heavier elements. In regards to the transition metal invoked in the study, platinum is next to the end of the 5d orbital filling which heavily encounters the third transition series contraction effect, which in-turn exhibits maximum impact from the relativistic effects.[53a-m] To overcome these effects for platinum and achieve higher accuracy in calculations, the employment of a relativistic ECP (RECP) basis set (def2-TZVP[57]) or a zeroth-order regular approximation (ZORA[58a-c]) method is required.

2.6 Density Functional Theory

Density Functional Theory (DFT) is built based on the Hohenberg–Kohn theorem, where the ground state electronic energy is solely determined by the electron density (ρ). DFT provides

a balance of computational cost and accuracy for energies and structures. HF theory and DFT are both a 3 spatial coordinate problem, but DFT is able go beyond the abilities of HF because it contains electron-correlation. This greatly reduces the computational costs governing the wavefunction-based approaches as those involve a 3N spatial coordinates of a system of N electrons. However, the exact functional used in the mapping of the electron density to energy is unknown. This leads to a plethora of available approximations.

With various levels of approximations, the simplest level begins with the local density approximation (LDA) and the local spin density approximation (LSDA). The LDA/LSDA supposes a local behavior and evaluates energy of the exchange correlation directly from $\rho(r)$. Improvements were made to this baseline approximation by considering the gradient of the electron density at this point of evaluation, known as the General Gradient Approximations (GGA). These functionals not only aim to consider the exchange and correlation energy associated with the electron density, but also on its derivatives. To improve GGA accuracy, the meta-GGA included the dependency on the kinetic energy density as well with the addition of a second derivative.

As the improvement ladder prevails, various thoughts on approximations thus far were still comparative to HF methods approach. Therefore a hybrid approach was proposed that adds in a percentage of the exact HF exchange to the functional. At this level of approximation we see two denoted branches, global and range-separated functionals, which differentiate based on the percentage of HF exchange being constant versus varying as a function of distance.[54]

The M06-2X hybrid functional is a new hybrid meta exchange-correlation functional, which adds in a partial semi-empirical approach. This functional incorporates 54% exact exchange, and it is parametrized only for nonmetals. Zhao and Truhlar reported M06-2X

displaying excellent performance in their study alky bond dissociation energies; in particular the dissociation of methyl R-X dissociation with a BDE of 97.58 kcal/mol against its precursor M06 whose BDE was 94.47 kcal/mol.[55] Both, however, blew out B3LYP (91.58 kcal/mol), which has often been used in DFT studies.[55,56] In regards to their π system tests and hydrocarbons tests, this functional performed well for these difficult DFT calculations. From their concluding remarks, M06-2X functionals are recommended most highly for the study of main-group thermochemistry and kinetics and it's the best choice for a combination of main-group thermochemistry, kinetics, and noncovalent interactions.

2.7   Polarized Continuum Model

Computational modeling can incorporate the same experimental environment, which often call for the addition of a solvent to the system. Methods to evaluate the environmental effects can be broadly categorized into two groups: 1) individual solvent molecules (explicit) or, 2) continuous medium of solvent molecules (implicit).[59] A combination of these is possible, however our focus will lie on the second method category.

Continuum models[60] consider the solvent as a uniformed polarized medium, called implicit solvation. The medium has a dielectric constant ε, and the solute **M** is placed in a specially modified hole in the medium as shown in **figure 2**.[32]
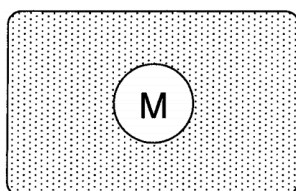
Figure 2. Reaction Field Model.

Solute **M** will polarize the medium from its electric charge by induced charge moments. This in

turn reacts back on the solute to create electrostatic stabilization. When employed in a self-

consistent field (SCF) procedure, the solvent model calculation is termed self-consistent reaction

field (SCRF). SCRF is a quantum chemistry approach, which models the solute M by either a

semi-empirical or ab initio calculations. Several SCRF models exist, and deviations pertain to the

size and shape description of the solute hole, the cavity/dispersion contribution calculation, the

representation of the charge distribution of **M**, and the description of the dielectric medium.

The Polarized Continuum Model (PCM) employs a van der Waals cavity with a detailed

description of the electrostatic potential, and parameterizes the cavity/dispersion contributions

based on the surface area.[61,62] Since the charge distribution of **M** polarizes the solvent continuum

of the cavity wall, this solvation method was termed PCM. The final interaction energy is

calculated iteratively, which deems this as an SCRF style calculation.[31] By using a continuum

solvation model over individual solvent molecules, it not only decreases computational costs but

gives a averaging effect of a large pool of solvent molecules. If the overall goal of a

computational study was to pinpoint the solvent effects on a specific process, the explicit model

would be best. However, continuum calculations are the easiest and most popular approach to

computing simulations in alignment with experimental whose sole purpose does not pertain to

solvent effects.

2.8 Minimum Energy Pathway (MEP)

Most all captivating chemical or physical processes involve transitions from one state to

another. The mechanism involved in these processes isn't necessarily stated for verbatim by a

drawn reaction, therefore theoretical studies can provide clarity by locating the transitions

minimum energy pathway (MEP). As its name states, the MEP is the lowest-energy pathway between two minima on a potential energy surface (PES). A PES is a surface defined by the potential energy at each point in configuration space. This is a high dimensional surface, which is often converted for visualization in a flat 2D energy reactant coordinate as shown in **figure 3**.
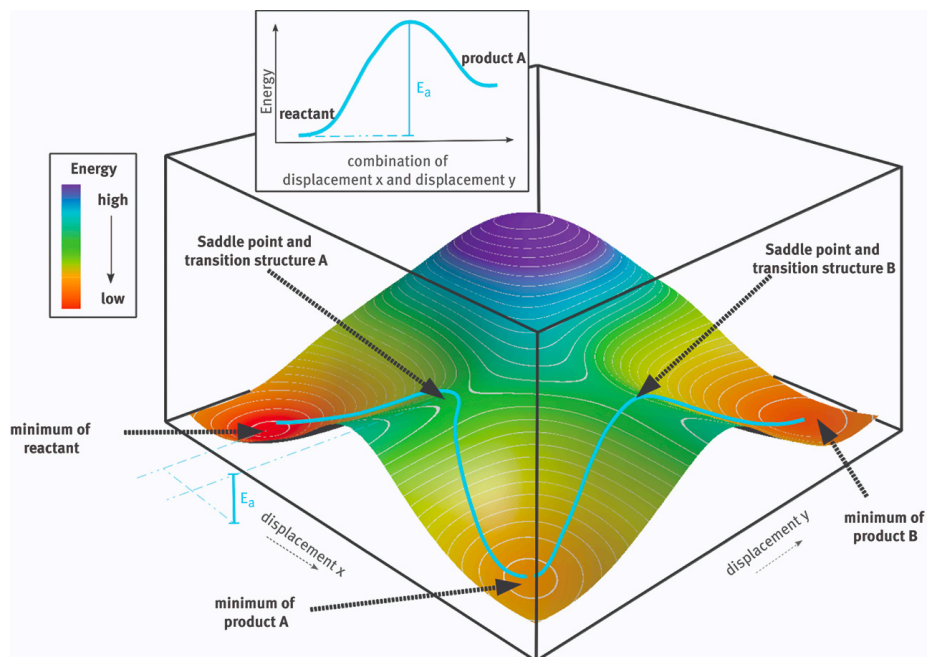
Figure 3. Potential Energy Surface example from a 2D Energy Diagram.[63]

In **figure 3**, the PES can be thought of as a topographical landscape map, where the motion is typically described as climbing up or sliding down the potential. If we consider each minimum as a location, we look to map out the easiest route to get from A to B (reactant to product). Different routes require different amounts of energy, or varying usage of gas if one considers the landscape mapping analogy. To get from A to B, the lowest amount of gas usage is preferred, as in traveling or computational context, it costs less. The points shown in **figure 3** labeled saddle points, are 1st ordered saddle points or transition states. According to the transition

state theory (TST), in between a reactant state and product state process, there is state known as a transition state. It is defined by the maximum of the lowest-energy path between two minima on the PES. The transition state formation occurs by the combination of thee minima's to form a species called an activated complex.

The activated complex is assumed to be in chemical equilibrium with the minima's, though this is not always the case. The overall rate of the reaction, if all species lie on the same PES, can be calculated from the concentration of the transition state and its rate of decomposition. Approximating this calculation in terms of vibrational frequencies of the initial state and the transition state gives :

$$k = \left(\prod_{j=1}^{N} \nu_j \right) \left(\prod_{j=1}^{N-1} \nu'_j \right)^{-1} e^{-\Delta^{\ddagger} G / k_{\mathrm{B}} T}$$

(1.6)

In equation 1.6, $\Delta^{\ddagger}G$ denotes the Gibbs free energy forming for the transition state from the initial state, and ν_j and $\nu_j{}'$ denotes thee vibrational frequencies of the initial potential minimum and thee transition state, respectively. True 1st order saddle points are transition states that are associated with a single negative frequency, which comes from there being only a single direction driving the system away from the saddle point rather than towards it. By simulating a system over time, we can observe the reaction rate and in principle calculate the reactions energetic barrier $\Delta^{\ddagger}G$. Several methods exist in locating the Minimum Energy Reaction Path (MERP), but we will only detail the technique used in this computational study.

2.8.1   Nudged Elastic Band (NEB) Method

A reliable method used to obtain transition state localization along a MERP is coined the Nudged Elastic Band (NEB) method. In this chain-of-states method, a series of equally spaced

intermediate states, called images, form a band between two minima, and are energetically

optimized. Equal spacing between the images is ensured by the chain formed from spring forces.

The images optimization along the NEB are converged by relaxation to the MERP through a

force projection scheme in which potential forces act perpendicular to the band, and spring

forces act along the band (**figure 4**).
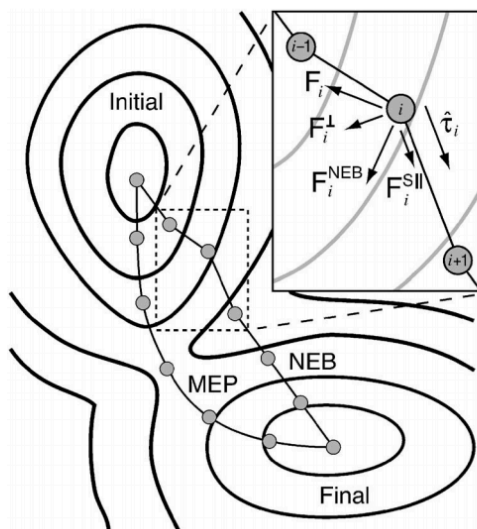
Figure 4. NEB visualization of the two components that make up the nudged elastic band force
F^{NEB}.

These projections are made by the tangent along the path $\hat{\tau}$ which is a defined unit vector for the

higher energy of the neighboring image.[64] The upwinding tangent improves the stability of the

NEB and avoids kink development.[64] In Figure 4, the details of NEB on a single image i is

examined. The NEB force is made up of two components (egn 1.7), the perpendicular force from

the potential and the parallel force from the spring.

$$\mathbf{F}_i^{NEB} = \mathbf{F}_i^{\perp} + \mathbf{F}_i^{S\|},$$

(1.7)

The saddle point characterized in NEB convergence to the MEP as the highest energy image provides a good estimate of the transition state between the two minima. Based on this rough estimate, a min-mode following saddle point search[65] from the highest energy image will pinpoint the transition state.[64,66] An additional mode to turn on during NEB to apply a better saddle point estimate is to use the climbing-image NEB (CI-NEB).[67] In this method, the highest energy image l feels no spring forces and climbs to the saddle via a reflection in the force along the tangent as shown in equation 1.8.

$$\mathbf{F}_l^{CI} = \mathbf{F}_l - 2\mathbf{F}_l \cdot \hat{\tau}_l \hat{\tau}_l. \tag{1.8}$$

Upon retaining the highest image saddle point via either method, the normal mode frequencies of the following transition state optimization will verify the activated complex versus a minima.

2.8.2 Dimer Optimization

The Dimer method[65a] alone can be used to find possible transition states without knowledge of the final structure or to refine a qualitative guess of a transition states structure. The "dimer" is formed from two images very close to each other on a PES. These two images, replicas R_1 and R_2, are shown in **figure 5** as the two larger circles.
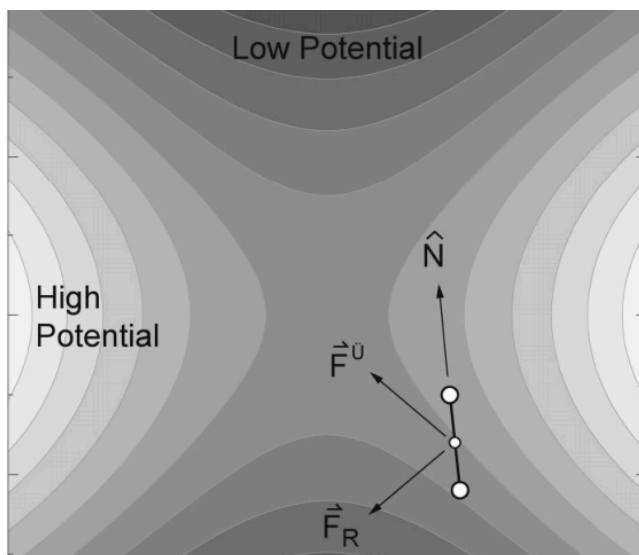
Figure 5. Schematic representation of the Dimer method.

The dimer has the same 3n coordinates, but are displaced a small distance from a common midpoint (smaller circle in **figure 5**). During the saddle point search, the algorithm involves moving the dimer uphill on a PES. This "move" involves two parts: rotation and translation. Every time the dimer is translated, it has to also rotate in order to find the lowest curvature mode (lowest energy orientation). A rotational force, $\vec{F}_R$, is defined as the difference in the force on the two replicas. By minimizing the energy with respect to the rotational force allows the dimer to align with the lowest curvature mode. The saddle point lies at a maximum along the lowest curvature direction. So as the dimer is being rotated it also is being translated and moved up the PES. The overall net force acting on the center of the dimer (small circle) pulls it towards a minimum. To avoid this pull, the effective force $F^{\ddagger}$ acts upon the center of the dimer, and is denoted as the true force. In the true force, the potential acting upon the midpoint of the dimer is defined as the opposite of the component along the dimer. Minimization of the true force brings the dimer to the saddle point.

The NEB method in several ways is complimentary to the dimer method. Initiating the NEB method not only finds the entire MEP between two minima, but also provides a qualitative guess of the saddle point. On the other hand, the dimer can find saddle points from an initial state, but the NEB finds the entire pathway between an initial state and a known final state. From the initial dimer paper[65a], it was suggested to apply these two computational tools. First by simulating a NEB, then by incorporating two images near the projected transition state of the NEB to be refined by dimer optimization.

2.8.3 Synchronous Transit-Guided Quasi-Newton (STQN) Method

Alternatively, transition state optimization can employ a gaussian based method. Categorized as one of the quasi-Newton methods, the use of a Synchronous Transit-Guided Quasi-Newton (STQN) Method[68] can locate transition state structures. These methods have been used extensively in ab initio calculations of molecules and empirical potential calculations of atomic and molecular clusters.[69] Gaussian STQN uses a quadratic synchronous transit approach to get closer to the quadratic region of the transition state, which then uses a quasi-Newton or eigenvector-following algorithm to complete the optimization. This method can be employed using 2 or 3 images, incorporating either the QST2 or QST3 option respectively. Initially this method was intended to use the reactant and product structures for the QST2, and an additional image of the transition state structure for the QST3. However, by employing this method as a complimentary method to NEB to refine the transition state geometry, the two imputed structures can be pulled from the NEB images as done during dimer calculations.

Quasi-Newton methods have been referred to as mode following methods. In comparison to dimer, denoted as a min-mode following method, the key difference lies in the number of

derivatives required for the evaluation of the Hessian matrix. The initial geometry or the system of coordinates used to represent each molecules is denoted as the initial Hessian. Quasi-Newton methods require the evaluation and inversion of the second derivative of the Hessian matrix, and in turn scale poorly with the number of degrees of freedom in a system.[65a] Second derivatives are not only costly in terms of computational time/power, but are considered unavailable for DFT calculations.[65a] The dimer method evaluates only the first derivative of thee potential energy, and incorporates the key qualities of the mode following algorithms.

Gaussian transition state STQN method falls under a combination of both a global and local approach. Global approaches interpolate between two stationary points, whereas the local approach has an initial hessian very close to the true transition state. Gaussians STQN method involves a combination of these approaches, but also offers a local method which employs the Berny algorithm.[70]

2.9 Vibrational Mode Analysis

Vibrational mode analysis is becoming increasingly important in catalytic and mechanistic research. These analysis can give questionable mechanistic steps a more detailed visualization of bond breaking or making to further validate or disproof suggested transitions. Theoretical simulation of vibrational spectra is performed through frequency calculations, which computes force constants, vibrational frequencies and intensities.[71] From this calculation, we can further differentiate between local minima versus maxima. Confirmation of any optimized saddle point comes from obtaining single negative frequency and simulation of its vibrational mode.

In Gaussian software[71], by default, the forces are analytically determined if possible by either a single numerical differentiation for methods that compute the first derivatives or by a

double numerical differentiation for methods that compute only energies. Vibrational frequencies as well as force constants, on the other hand, are calculated by determining the second derivatives of the energy with respect to the cartesian nuclear coordinates. For stationary points, this second derivative of the cartesian nuclear coordinates is transformed to mass-weighted coordinates.

CHAPTER 3: COMPUTATIONAL STUDY

3.1 Introduction

C-H bond activation is a key chemical transition that could globally reduce the use of natural hydrocarbon resources and create extensive energy conservation.[72-73] Organometallic C-H bond activation has been a popular area of research for over 50 years, and this area has seen tremendous success.[74-77] In particular, these cycloplatinated complexes were synthesized using a unique platinum-catalyzed C-H acylation reaction that does not require the use of any oxidants or other additives.[78]

Platinum catalyzed C-H acylation was shown to involve two distinct steps, cyclometalation and acylation of the cyclometalated complex, which was seen in previous results.[79-80] From the overall proposed mechanistic pathway, the formal electrophilic addition portion will be studied by incorporation of the Nudged Elastic Band (NEB) method. The exact mechanism for the formal electrophilic addition is still unclear, and two possible pathways are proposed in **scheme 12** below.[78] Incorporating the nudged elastic band method upon both mechanistic pathways, nucleophilic substitution and/or oxidative-addition, will lead to discovery of identifying local minimums versus transition states.[81] This studied reaction, in comparison to typical metal-catalyzed reactions, displays a completely different mechanism.[82-85] Either pathway will offer a form of direct C-H acylation that introduces a carbonyl group to an aromatic ring selectively.[79] Carbonyl groups are a key functional group based on its universal role in pharmaceuticals and its ability to easily transform into several other functional groups.[78] Along with being able to synthesize these structures without any oxidants or additives this could be ground breaking for pharmaceuticals.
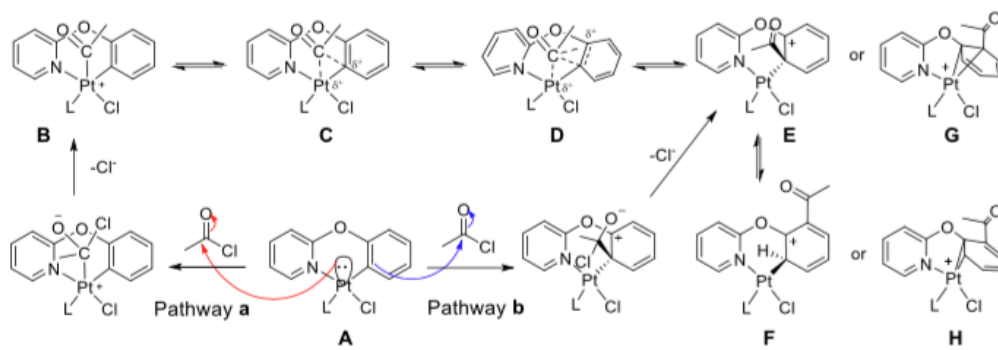
Scheme 12. Proposed pathways for acylation reaction

Experimentally, the mechanistic studies of transition metal catalyzed reactions are extremely difficult to observe, but with the aid of computational modeling further evidence can justify the proposed pathways.[80] Theoretically dealing with competing pathways of very similar potential energy surfaces will have its own level of difficulty as a simulation is done, essentially by trial and error, to match the experimental data.[81] Utilizing NEB in the mapping process will offer potential creditability to the proposed mechanisms or discovery of a different order of feasible reaction steps. Once two local minima's have been optimized, NEB can find the minimum energy pathway (MEP) that connects these two intermediates.[81] NEB is a chain-of-states method, where several states (images) are connected in a step-wise manner to map out a path.[86] Each image will have a parallel force applied to keep all images evenly placed along the MEP as well as a perpendicular force to enhance convergence of the minima.[86] Once a theoretical pathway has been simulated, the experimental mechanism proposed can confirm structures as either intermediates to transition states, and observe any overlooked stationary points. The chain of images will connect all local minimums to their adjacent transition states in between two initial structures used as the end points.[86]

3.2 Computational Methodology

Geometry Optimization. Structures were built using material studios[87] and optimized with Gaussian 16 (G16)[88] software on linux work stations. A hybrid functional, M06-2X, will be applied for the entire DFT study. Two basis sets were incorporated: For platinum, both f and g polarization functions were included from utilizing def2-TZVP basis set, and all other atoms were simulated with 6-311+g** and MAUG-cc-pVTZ basis set. To incorporate experimental environment to the theoretical study a polarizable continuum model (PCM) was used in default for the self-consistent reaction field (SCRF) method. The solvent effects how these structures optimize due to their overall positive charge. Chlorobenzene was the medium used in all calculations to match the experimental environment. The structures presented in the mechanistic pathway were optimized as complexes to ensure equivalent atom to atom match-up for NEB employment. All final geometry optimizations were verified as minima or maxima through their frequency analysis.

Frequencies. Force constants and vibrational frequencies for each optimized structure were assayed. Both force constants and vibrational frequencies are computed from the second derivative of the energies with respect to cartesian nuclear coordinates. Vibrational frequencies are only valid for stationary points, therefore if a structure cannot be optimized then its frequency will be skewed. The completed frequency calculation will include numerous types of data such as frequencies, intensities, associated normal modes, the structure's zero-point energy, and various thermo-chemical properties. The same level of theory applied in optimizations was applied in the frequency calculations too. Since some structures optimized were local maximum instead of minimums, the number of imaginary frequencies validated if true saddle points were found. A structure with n number of imaginary frequencies is an nth order saddle point.

Therefore, a 1st order saddle point will be characterized by one imaginary frequency. This negative frequency implies a negative force constant, further meaning that in one direction, in nuclear configuration space, the energy has a maximum, while in all other (orthogonal) directions the energy is a minimum.

Potential energy profile simulation using NEB. The Nudged Elastic Band (NEB) method maps the reaction pathway between to stationary points on a potential energy surface. A fire optimizer was selected to manipulate the NEB, which followed with either a min-mode following method or a mode following method. Each NEB calculation aimed to initially incorporate 20 images between two stationary points (total of 22 images), but upon additional reactions added to the study the total images was cut down to 13 for time constraints. NEB calculations were performed using G16[88] or Gaussian 09 (g09)[89] software at a M06-2X/6-311+g**/def2-TZVP-Pt level of theory. All calculations employed the same polarizable continuum model used in optimization/frequency calculations. Further refining of the qualitatively obtained transition state structures will be performed and then validated through their vibrational mode.

Transition State Refining. Upon reaching convergence to the MEP through a NEB calculation, the obtained reaction pathway will provide qualitative cartesian coordinates of images close to or right on the NEBs projected transition state. A min-mode following method, denoted as the dimer method, will improve the projected hessian matrix of the transition state structure by taking two images (replicas) on the reaction pathway near the transition state for extrapolation. Through several translational and rotational movements, the dimer will extrapolate to a third point which corresponds to a more reasonable transition state. Dimer only evaluates the gradient, or first derivatives, unlike the alternative Synchronous Transit-Guided Quasi-Newton

(STQN) Method transition state searching tool. In addition to taking two images close to the transition state along the project MEP for dimer, they were also simulated using a QST2 option in the STQN method. The 2 in QST2 option states two images must be used, and are originally stated to be the two local minima rather than two lower ordered saddle points. However, in this presented research QST2 simulations were ran using the same images used in the dimer. The gaussian optimizations incorporated the CalcFC option to calculate the force constants at the first points since it generally will improve convergence. Gaussian TS optimizations will stop if there are more than one negative force constant calculated, so eigen test was turned off to avoid potential job termination. All transition state optimizations were ran on either G16 or G09 using the M06-2X/6-311+g**/def2-TZVP-Pt level of theory. The original project proposed allotted time for the comparison of basis sets, so further transition state optimization was done on the optimized 6-311+g** geometry using the MAUG-cc-PVTZ basis set. This larger basis set optimization was performed either by re-running a dimer with the optimized restart files or through a Gaussian TS optimization that applied the Berny algorithm.

Vibrational Mode Analysis. All optimizations were validated based on their G16 or G09 frequency calculations. The optimizations level of theory matched in their associated frequency calculation. For optimized reactants and products the frequency analysis was straight forward, provided all positive frequencies, and the retained zero-point correction was applied to their corresponding optimization energies. Verification of the nature of true transitions states optimized were validated from only the first frequency being negative. The frequencies vibrational mode was animated to provide insight into the steps of the mechanism at play and if the theoretically predicted transition state was plausible or not.

3.3 Results and Discussions

3.3.1 Optimization of Stationary Points

In the original presented reaction scheme (**scheme 12**) investigated, we first aimed to optimize every structure proposed as complexes. In order to simulate a theoretical reaction mechanism study, thee two connecting points in a chain-of-states method must have identical atom counts. Therefore, each species had to have a total of 36 atoms. The addition to **scheme 12** lead to the studies presented reaction in **Scheme 13**, which is represented below, and is illustrated as structure's rather than complexes.
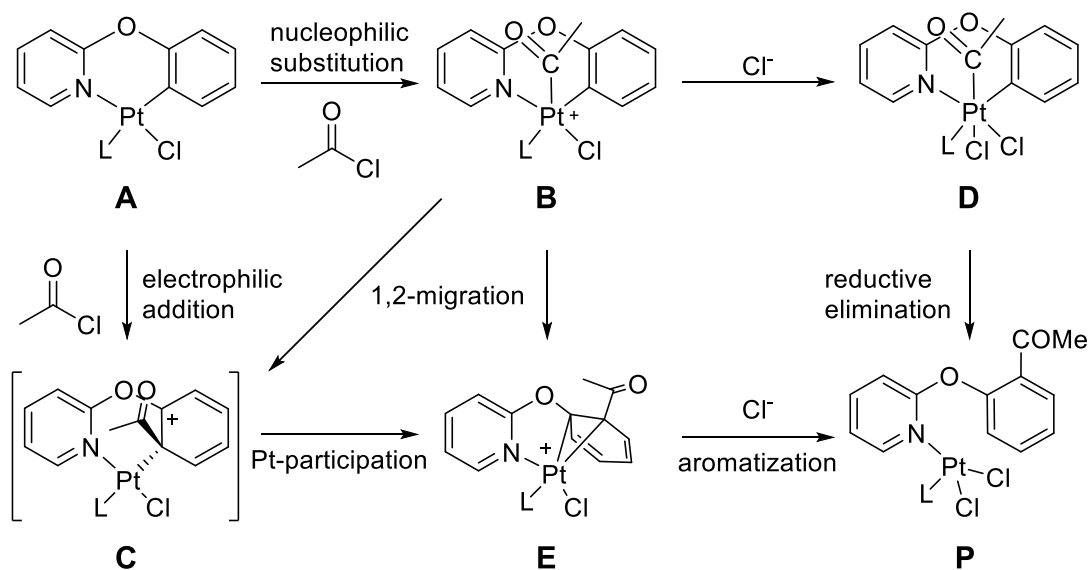
Scheme 13. Proposed pathways for the acylation of complex A (L= acetonitrile).

Reactant **A**, for example, was optimized by strategically placing the acetyl chloride structure in associating range with the reactant. Optimizing complex **A** required several trial and error runs to align the carbonyl carbon in the acetyl chloride in a non-bonding, yet not completely lost, range to the platinum in **A**. The numerous spatial arrangements available for the acetyl chloride group not only created optimizing challenges, but all computational calculations

were also ran in a PCM model. Complex **A** optimization challenges were minute compared to obtaining complexes **B**, **C**, **E**, and **D**. In all 4 of these structures, the atom count is 35. Therefore, for the reaction pathway studies, the lost chlorine had placed around each structure. The location of this Cl^- ion created challenges in obtaining convergence in these optimizations. Electron dense regions tended to stabilize this chlorine for the complexes convergence, but the location for reaction pathway studies was not always optimal. In addition to placing the leaving group in an optimal reaction study location, several spatial arrangements of the acyl group were identified too. Modifications with both of these features lead to optimized structures varying in energies. Assumption to use the lowest energetic complex was not necessarily plausible for the mechanism being studied. Connection between two reasonable minima were sometimes preferred over lower connection of the lowest energy minima. The challenges of numerous possibilities was only enhanced by the solvent effects too. All structures presented in **scheme 13**, aside from complex **C**, were optimized and verified by their frequency calculations as minima.

Complexes **D** and **P** were added later to this study, which lead to further complications. Complex **D** associated challenges were the same as seen in complex **B**, and **E**. However, optimization of complex **P** showed the ligand preferred to be swapped with the Cl in the platinum structures illustrated in **scheme 13**. A third challenge was now shown to exist based on the placement of the coordinating L and Cl on the platinum. Additionally Optimizing the cis confirmation of complex **P**, however, did not eliminate this new prompted challenge. Due to time constraints on this study, the optimization of the L and Cl swap on platinum in the previous complexes was unable to be performed. All optimized structures obtained for each complex are displayed below (**figures 6-11**), with their corresponding geometric parameters following in **tables 2-6**.
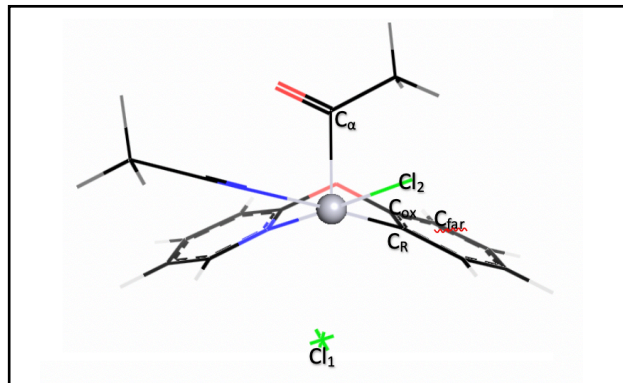
Figure 6. Atom Labeling System for all Proceeding Structures.

a. A1

b. A2

c. A3

Figure 7a-c. All Complex A Structures Optimized and Labeled Accordingly.

Table 2. Geometry Parameters of all Optimized A Complexes.

Bond Length (Å)	A1	A2	A3
Pt - L	2.2049	2.2022	2.0029
Pt - N	2.0578	2.0562	2.0452
Pt – C_R	1.9578	1.9588	1.9683
Pt - Cl_1	2.3576	2.3619	2.5186
Pt - C_a	3.4841	3.4051	3.4736
Pt – Cl_2	3.8782	4.0594	3.9424
C_a - C_R	4.5167	4.1258	3.8225
C_a - Cl_2	1.8283	1.8224	1.8227
Pt - C_{ox}	2.9074	2.9125	2.9150
Pt - C_{far}	4.2363	4.2407	4.2424
Bond Angles (°)			
C_a - Pt - Cr	108.9	96.8	84.4
L - N - C_R - Cl	1.1	0.2	-1.0

Figure 8a-c. All Complex B Structures Optimized and Labeled Accordingly.

Table 3. Geometry Parameters of all Optimized B Complexes.

Bond Length (Å)	B1	B2	B3
Pt - L	2.2386	2.2266	2.2355
Pt - N	2.0627	2.0604	2.0718
Pt – C_R	1.9788	1.9788	1.9769
Pt - Cl_1	2.3303	2.3245	2.3229
Pt - C_a	2.0546	2.0488	2.0968
Pt – Cl_2	7.7192	5.1905	5.9854
C_a - C_R	2.9468	2.9395	2.9720
C_a - Cl_2	8.1624	6.4048	3.9720

Pt - C_{ox}	2.9111	2.9130	2.9101
Pt - C_{far}	4.2350	4.2368	4.2360
Bond Angles (°)			
C_a - Pt - Cr	93.9	93.7	93.7
L - N - C_R - Cl	-1.5	-1.1	0.3

a. E1

b. E2

Figure 9a-b. All Complex E Structures Optimized and Labeled Accordingly.

Table 4. Geometry Parameters of all Optimized E Complexes.

Bond Length (Å)	E1	E2
Pt - L	2.0158	2.0335
Pt - N	2.0437	2.0430
Pt – C_R	2.2993	2.2924
Pt - Cl_1	2.3328	2.3336
Pt - C_a	3.0504	3.0304
Pt – Cl_2	5.2174	3.5228
C_a - C_R	1.5225	1.5202
C_a - Cl_2	6.5049	5.7605

Pt - C_{ox}	2.3422	2.2926
Pt - C_{far}	3.1423	3.0808
Bond Angles (°)		
C_a - Pt - Cr	29.0	29.2
L - N - C_R - Cl	9.2	6.0
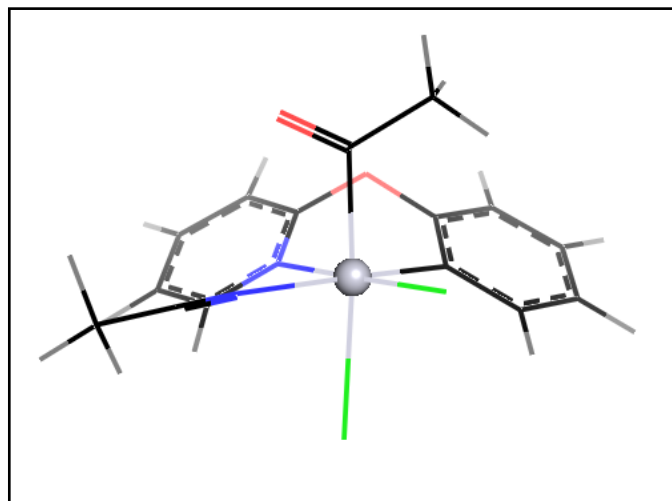
Figure 10. Complex D1 Optimized.

Table 5. Geometry Parameters of the Optimized D Complex.

Bond Length (Å)	D1
Pt - L	2.2473
Pt - N	2.0648
Pt – C_R	1.9758
Pt - Cl_1	2.3344
Pt - C_a	2.0260
Pt – Cl_2	2.5864
C_a - C_R	2.8667
C_a - Cl_2	4.6089
Pt - C_{ox}	2.9106
Pt - C_{far}	4.2343
Bond Angles (°)	

C$_a$ - C$_R$ - Pt	91.5
L - N - C$_R$ - Cl	-1.7

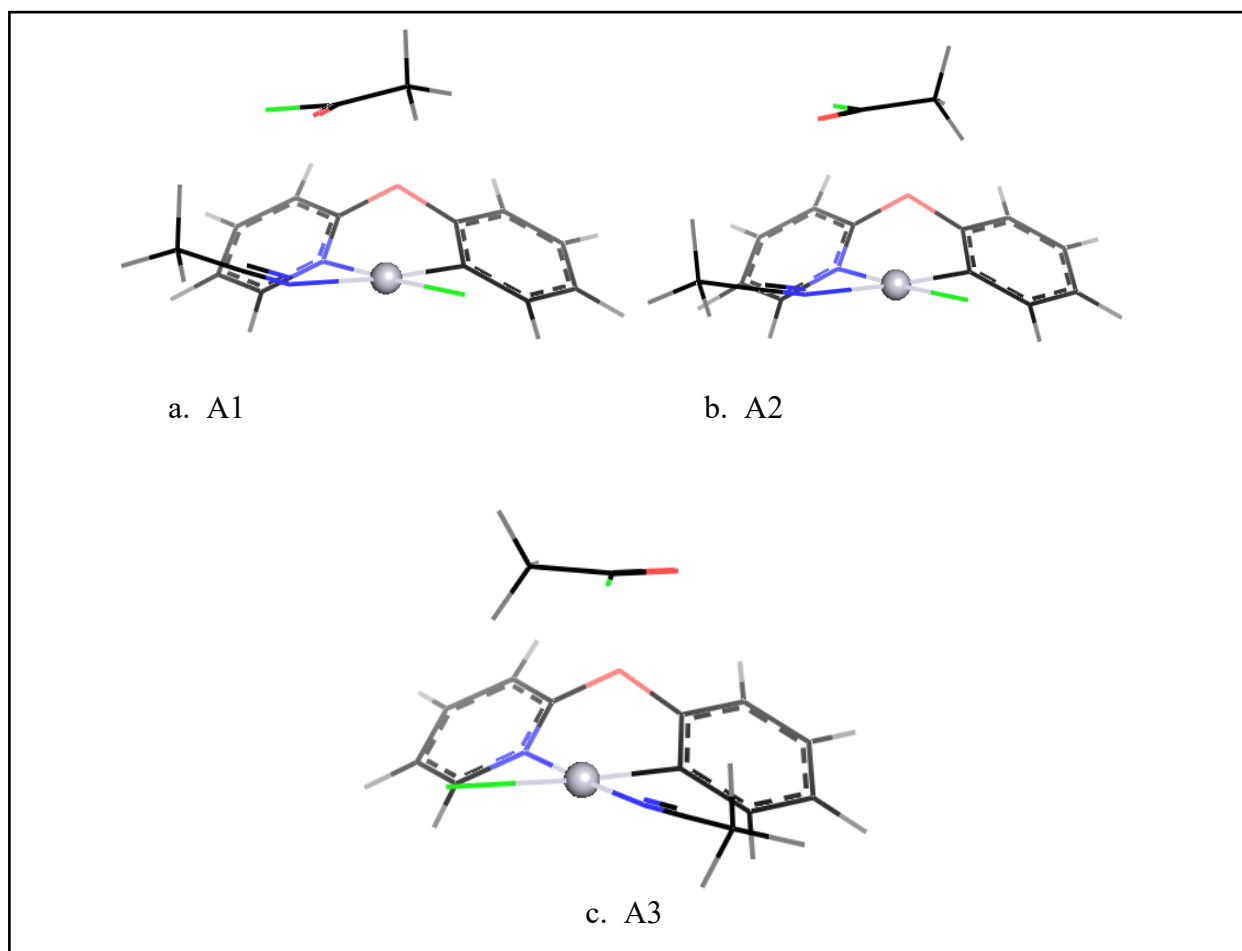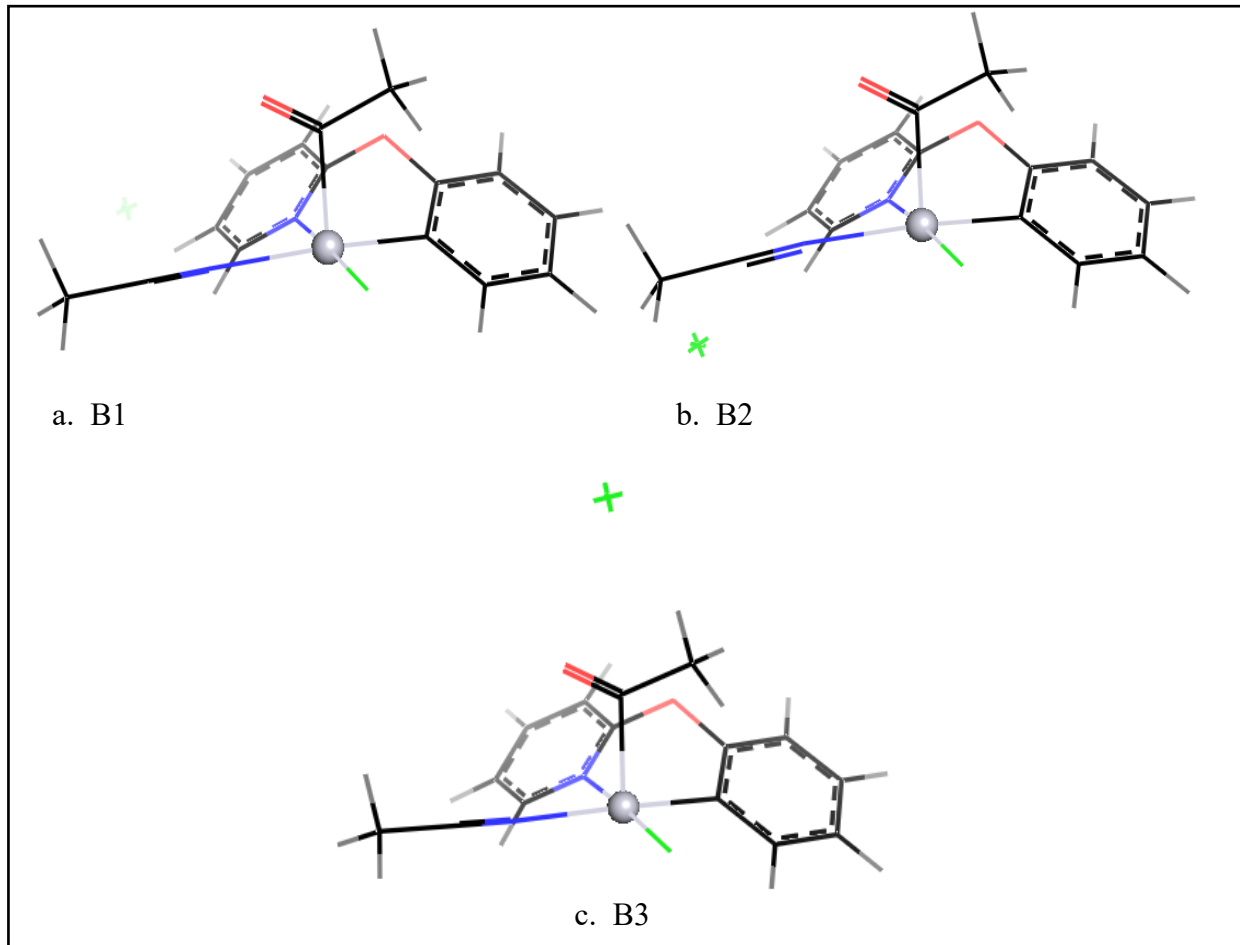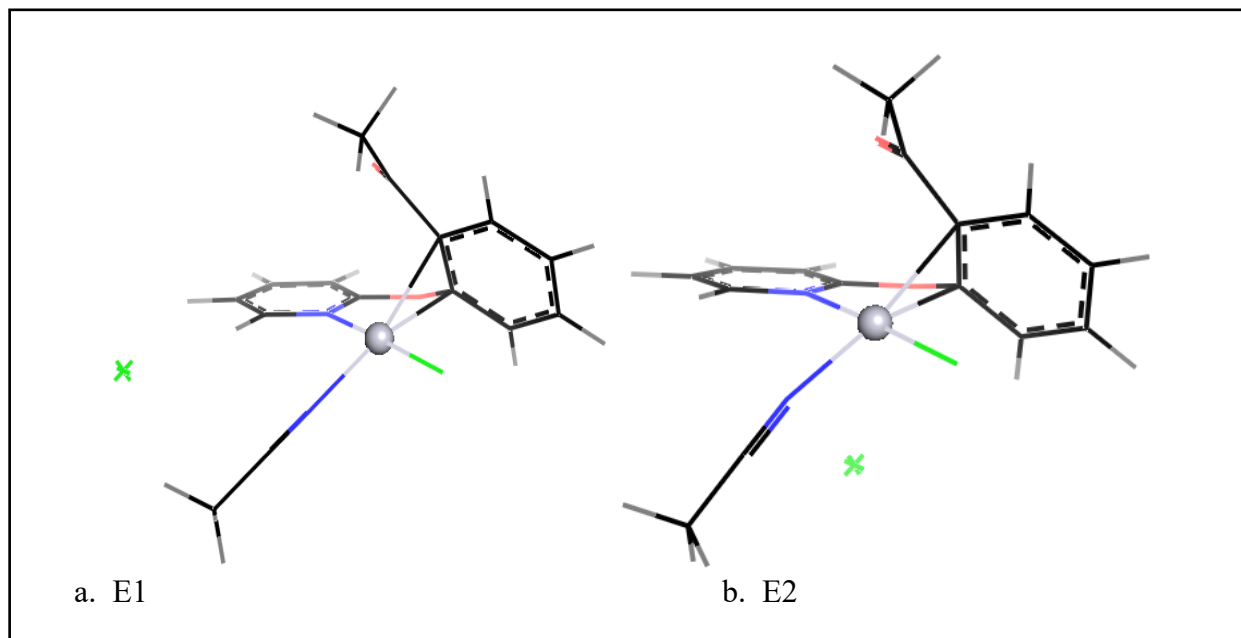a. P1

b. P2

c. P3
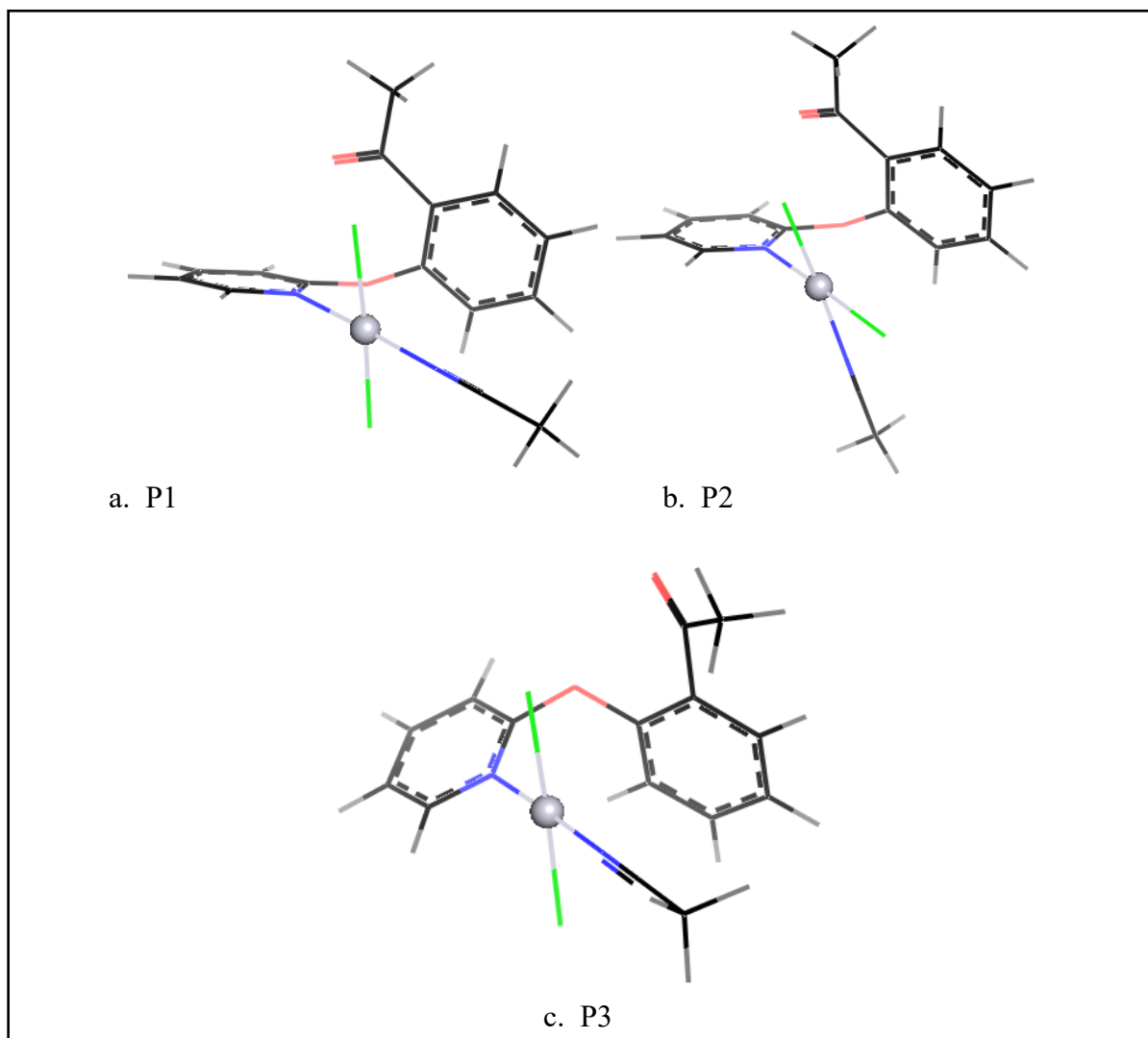
Figure 11a-c. All Complex P Structures Optimized and Labeled Accordingly.

Table 6. Geometry Parameters of all Optimized P Complexes.

Bond Length (Å)	P1	P2	P3
Pt - L	1.9966	2.0119	1.9932
Pt - N	2.0443	2.0795	2.0501

Pt – C_R	3.4220	3.3627	3.5814
Pt - Cl_1	2.3506	2.3304	2.3503
Pt - C_a	4.0353	3.9886	4.1572
Pt – Cl_2	2.3506	2.3236	2.3452
C_a - C_R	1.4992	1.4981	1.5024
C_a - Cl_2	3.4996	3.5150	3.3351
Pt - C_{ox}	3.0711	3.0640	3.1469
Pt - C_{far}	3.4718	3.4809	3.4929
Bond Angles (°)			
C_a - Pt - C_R	21.2	21.4	20.7
L - N - C_R - Cl	45.6	-41.5	46.3

After all optimizations converged, their corresponding frequency calculation was

performed. Each complex presented was verified as local minima based on all positive

frequencies obtained. The zero-point correction factor was taken from the frequency calculation

to correct the optimized energy to the zero-point correction corrected energy. Each complex

structures associated energy is presented in **table 7**.

Table 7. HF energies from optimization, Zero-Point Correction factor, and their combined Zero-Point Correction Energy value in units of Hartee/Particle.

	A1	A2	A3
HF	-1879.5971	-1879.5964	-1879.6981
ZPC	0.2626	0.2628	0.2636
HF-ZPC	-1879.3344	-1879.3336	-1879.4345
	B1	B2	B3
HF	-1879.5653	-1879.5747	-1879.5964
ZPC	0.2630	0.2635	0.2628
HF-ZPC	-1879.3024	-1879.3112	-1879.3336
	E1	E2	D1
HF	-1879.5732	-1879.5684	-1879.5924

ZPC	0.2636	0.2637	0.2635
HF-ZPC	-1879.3096	-1879.3048	-1879.3289
	P1 - trans	**P2 - cis**	**P3**
HF	-1879.6176	-1879.6125	-1879.61499
ZPC	0.2648	0.2645	0.264592
HF-ZPC	-1879.3529	-1879.3480	-1879.3504

Ligand Cl swap energy assay for complex A and P. From energy analysis in **table 7**, it clearly shows complex **A3** (**figure 7c**) is the lowest energetic complex optimized. In **A3**, the ligand is swapped with the Cl based on their coordination the platinum. **A3** in reference to both **A1** (**figure 7a**) and **A2** (**figure 7b**) is 62.75 kcal/mol lower in energy. Unfortunately, this **A3** complex was discovered later in this mechanistic study so the initial complex comparison was based on **A1** versus **A2**, in which **A1** was only 0.5 kcal/mol lower in energy. However, the validation in the ligand swap on platinum being lower in energy holds true largely regards to complex **A**, but also competitive in complex **P**. The latter found complex **P3** (**figure 11c**), where the ligand and Cl are swapped, is 1.56 kcal/mol higher in energy to **P1** (**figure 11a**). Complex **P1**, which was ran in the mechanistic study, is the lowest energy complex. However **P1**, in reference to all other structures used, has the ligand on the opposite side. Comparison of **P1** (trans) to its cis conformation **P2** (**figure 11b**) is 3.07 kcal/mol lower in energy.

B complexes energy assay. Three different **B** complexes were optimized, **B1** (**figure 8a**) being the first structure obtained and initially ran in NEB. The latter found **B3** (**figure 8c**) complex, where the Cl is stabilized above **B** is largely more energetically stable. In reference to **B1** and **B2** (**figure 8b**), complex **B3** is 19.62 kal/mol and 14.01 kcal/mol lower in energy, respectively. However, from the NEB between complex **A2** and **B3**, the following QST2 optimized transition state obtained (**figure 31c**) has lower in energy than complex **B3**; Therefore complex **B2** was the preferred structure for the **B** complex in the mechanistic studies. This

simulation will be discussed later. **B2** is 5.52 kcal/mol lower in energy than **B1**. Interestingly the main difference structurally between these two is the location of the Cl⁻. In the **B2** complex, the Cl⁻ is stabilized between the nitrogen ring and the ligand, whereas in complex **B1** the Cl⁻ is stabilized between the two hydrogens on thee farther side of the nitrogen ring. The location of the Cl⁻ being farther away in complex **B1** created a lengthy travel for the leaving group, which is seen in its NEB calculation. Another interesting insight was found when optimizing a **B** structure with the Cl⁻ placed below the Pt complex; The complex obtained was identical to the complex **D** (**figure 10**).

      D complexes energy assay. Only one complex of **D** (**figure 10**) was optimized, as there weren't any conformation possibilities to trial. However, as mentioned in the assay of complex **B**, by placing the Cl⁻ below the platinum structure the leaving group converged into the same bonding distance to Pt as in the complex **D** originally optimized. This leaving group's bonding to platinum in complex **D** is 2.5864 Å, which is arguably more of an interaction than an actual bond. Several optimizations were trialed, but the only converged structure of **D** was associated with this bond length. This bond length continuously optimizing to this length could be due to relativistic of both Pt and Cl⁻, and may require trials of different level of theories to create a more plausible bond length between the two.

      E complexes energy assay. The initially optimized E complex simulated gave complex **E1** (**figure 9a**). The latter trialed **E2** (**figure 9b**), where the Cl⁻ was placed below the Pt ring, was found to be 3.04 kcal/mol higher in energy than complex **E1**. In complex **E1**, the Cl⁻ was stabilized in the same region as in **B2** (**figure 8b**), which was between the nitrogen ring and the ligand. Since this similarity was noted, it made it interesting to see the placement of Cl⁻ in **E2** did not converge in similar reference to the interaction of Pt and Cl⁻ seen in complex **D** (**figure 10**).

Though on the other hand, this is more plausible considering that in the **E** complex the platinum is experiencing a coordination of 5. The single positive charge of platinum is stabilized by the negatively charged Cl in the system, so this could be the sole reason Cl⁻ stays at a bond length of 3.523 Å to Pt.

3.3.2 NEB Simulations

All neb calculations were initially ran using 22 images. However, with additional reaction paths added and multiple complexes optimized, the newest neb calculations were ran using 13 images. The only exception to this was **A2** to **E2**, and this reaction is currently still in the transition state refining step.

A to B neb mappings. The formation of B can be considered either as the first step of oxidative addition or as a classical nucleophilic substitution of the acyl chloride Initially, all NEB simulations began with our first few optimized orientation complexes. Both **A1** and **A2** complexes were ran to **B1**. The NEB simulation for **A1** to **B1** ran 402 cycles total, but the dimer optimization was initiated earlier using cycle 72. These NEB curves are shown in **figure 12** below. In **figure 12b**, the given transition state image 9 and image 11 were used to create the dimer. Upon dimer optimization, the obtained transition state was confirmed as a first order saddle point from the single negative frequency obtained (-236.4268). The NEB ran to our initial default max cycles (450), yet the molecular force and neb force did not lower into the ideal convergence range. From cycles 402, both the molecular force and neb force was 0.0148 h/b, with the molecular force denoted by image 12. Ideally, the dimer optimization would be pulled from neb simulations where convergence of the force from the highest energy image is around 0.005 or lower. Also, at cycle 354 the climbing image feature was turned on for the remaining cycles, and still the force convergence was not seen in the ideal range.

a.

b.
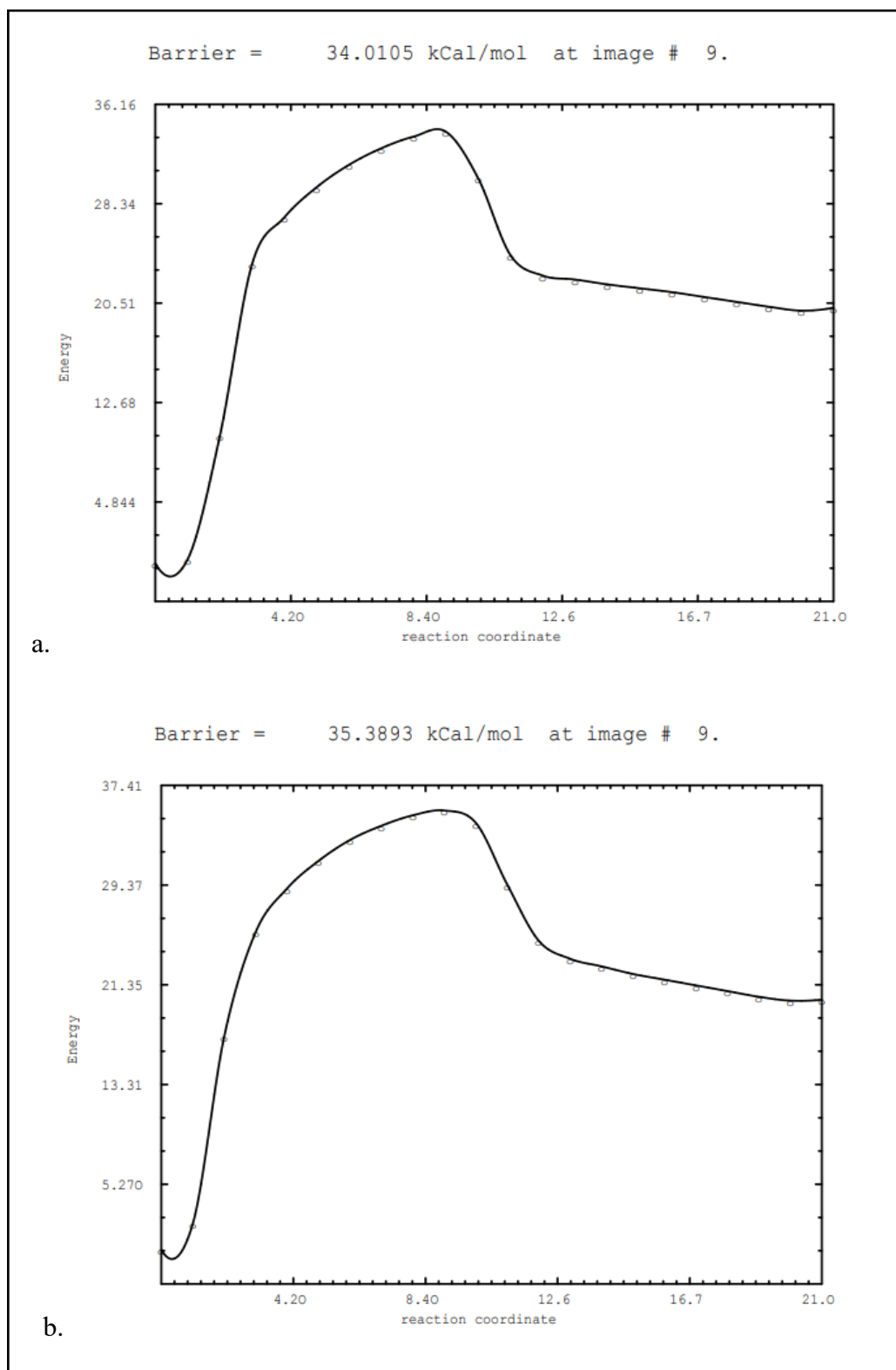
Figure 12ab. A1 to B1 NEB simulations. 6a displays cycle 402, and 6b displays cycle 72 from which the dimer was created.

Additionally, **A2** to **B1** was ran to the maximum defined cycles in NEB – 450 (**figure 13**). The dimer was pulled directly from the last cycle ran, which showed a drastically lower convergence in terms of molecular and neb force (0.00143, 0.00141). This neb incorporated the climbing image feature as well from cycle 391 to 450. The dimer optimization used two of the images surrounding the neb's suggested transition state (image 7). Since image 6 and 8 were used to create the dimer, it was indicated in the dimer set up that the images, R_1 and R_2, were surrounding transition state images. Whereas, in A1 to B1 dimer the transition state image from the neb was used, so the default R_0 and R_1 was kept. The transition state obtained from dimer had two negativity frequencies, but the second being so small it was classified into the numerical noise range. The first negativity frequency was -294.6959, and the second -12.9025.
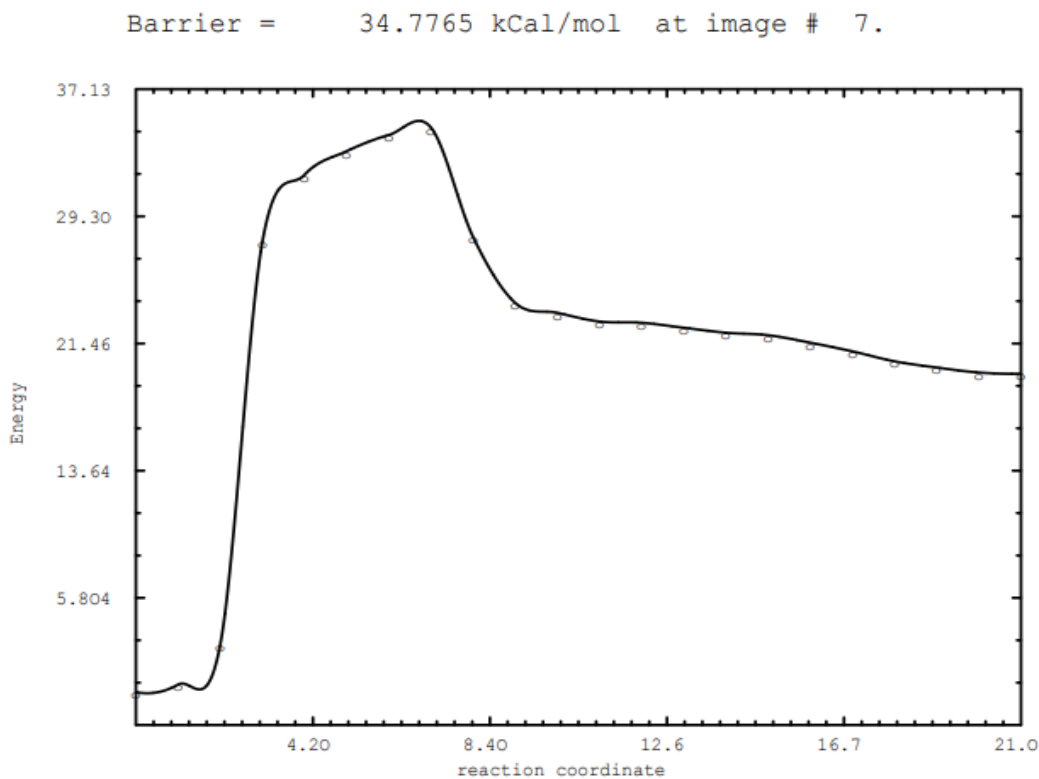
Figure 13. A2 to B1 NEB curve after running 450 cycles.

Both **A1** and **A2** to **B1** NEB curves (**figures 12 and 13**) are not the ideal smooth hill type curves that are desired. From analysis of both curves projected pathways, the same overall process occurred. Images 1- 4 showed the bond breaking of the chloride in the acetyl chloride group above the platinum ring, followed by the shorter rise that was due to both the carbonyl carbon of the acyl group and platinum coming in closer to each other as the Cl^- ion continued to leave. The long trailing of images to the product is a result of the long travel for the Cl^- ion to be in the optimized location of **B1**.

Later on in this study, an alternative **B2** complex was optimized in which the leaving Cl^- ion was converged in a closer location. This modification to B eliminated the lengthy traveling seen in both previously presented neb curves. Complex **B2** was optimized by Dr. Bartolotti, and was ran between **A3** and **B2**. The neb curve he obtained in shown in **figure 14**. Based on his neb curve and optimized transition state, it was determined that complexes **B1** and **B2** were interchangeable in regards its transition state being on the same MEP as all other A to B reaction mechanisms found. Therefore, later on in this discussion the shown energy diagrams will interchange the **B1** for **B2** complex, regardless of which neb mapped the presented transition state.
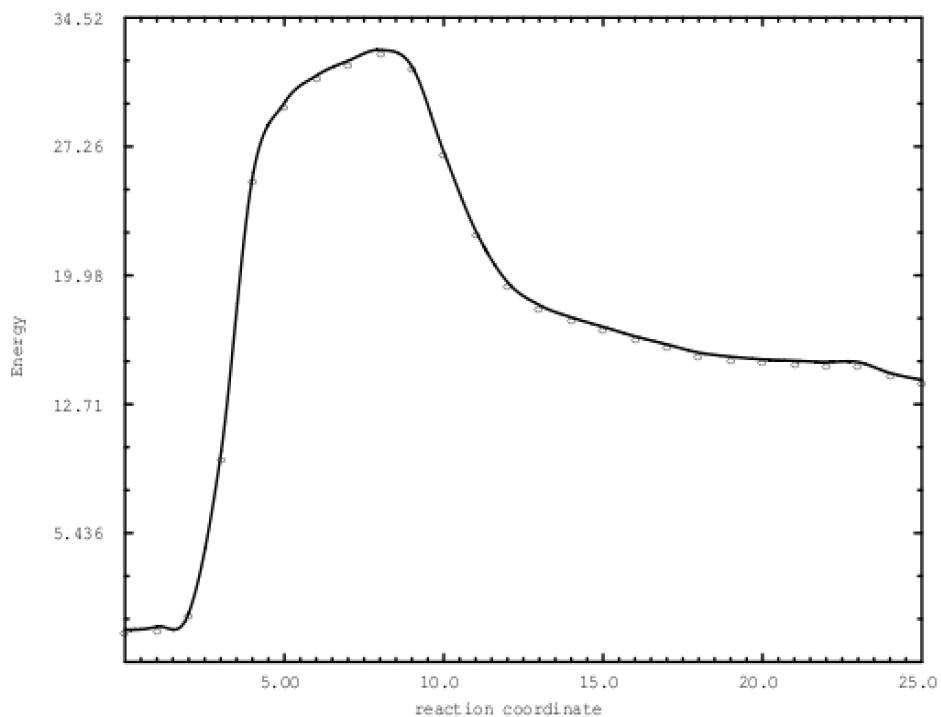
Figure 14. A3 (L and Cl swap) to B2 neb curve simulated by Dr. Bartolotti.

In addition to the newest B structure, **B2**, further optimization of alternative **B** complexes was researched based on the experimental environment having free Cl⁻ ions immersed all in solution. Therefore, our investigation later added in optimizations of several free Cl⁻ ion locations, which led to the optimized **B3** complex. A neb was ran between **A2** and **B3** (**figure 15**) and the molecular and neb forces converged at 0.00129 and 0.00112, respectively. This neb was ran for 311 cycles, but the climbing image feature was never enabled. Also, the total image count was cut from 22 to 13 to save on computational costs with multiple neb simulations added in later.

Barrier =   27.3463 kCal/mol   at image # 6.
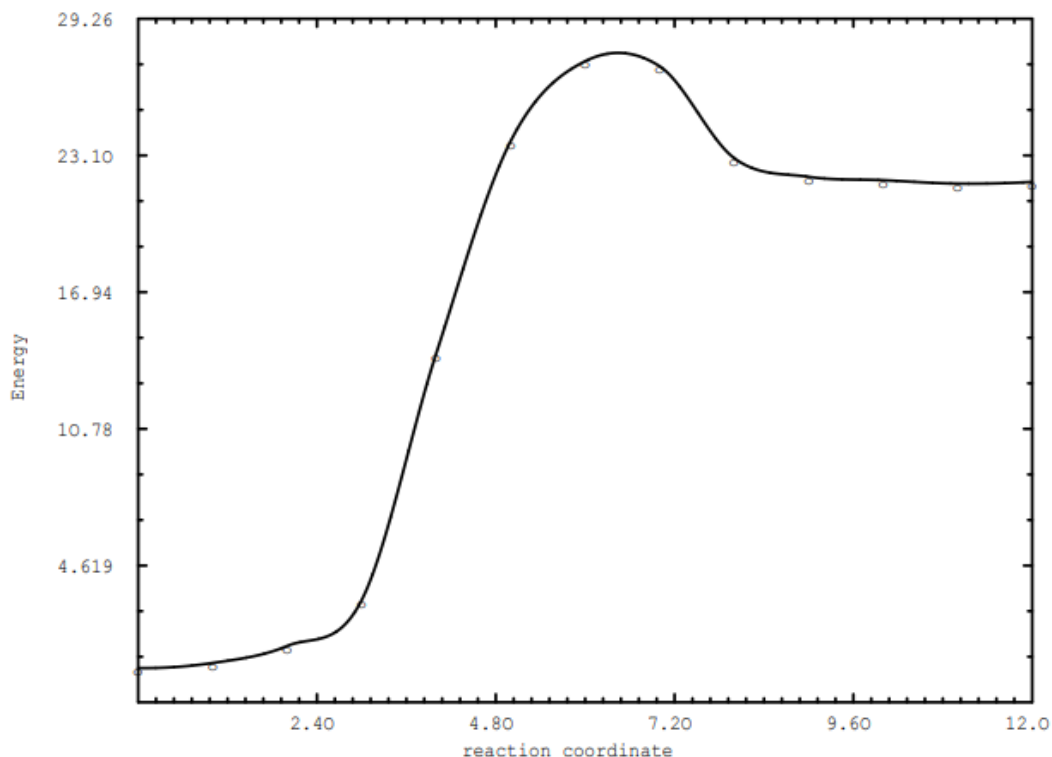
Figure 15. A2 to B3 neb curve.

Interestingly, the transition state search in the **A2** to **B3** neb mapping led to a transition

state lower in energy than complex **B3**. In the neb mapping, there is a clear display of a transition

state higher in energy than **B3**. However, from a QST2 optimization using images 6 and 7, the

refined transition state was 0.27 kcal/mol lower in energy than complex **B3**. Due to time

constraints, only a QST2 transition state search was performed. From the obtained results, no

further reaction pathways were mapped using **B3**, but further analysis using a dimer method

should be done in the future to confirm if a reasonable transition state exists between the two.

A to E neb mappings. From the initial proposed mechanistic study, **scheme 12**, the

alternative for **A** to **B** was **A** to **E**. This pathway involves the nucleophilic attack of the metalated

carbon (electron-rich) at the carbonyl group. Since neb mapping can identify potential local

minima, this simulation also aimed at obtaining a potential new intermediate or the complex **C**

structure. Upon initially discovering **A2** as the lower energy complex, the majority of the neb

simulations that follow use this structure as one of the stationary structures. The initial neb of **A2**

to **E1** was extended its maximum cycles, so it was ran to 460 as shown in **figure 16**. Climbing

image was used from cycle 296 to 460, but the forces did not converge. In cycle 460, the

molecular force was 0.0107 and the neb force was 0.0102. Nearly 2x the ideal convergence

range, which could be associated with the rough curve obtained. Again, in the first few images

leading up to image 10, we observe the chlorine leaving the acyl group prior to C-Pt formation.

The orientation of the acetyl chloride rotates for the Cl leaving to face the direction of its

location in complex **E1** as well. From images 10 - 12 we observe Cl⁻ leaving as the acyl group

displays a somewhat linear C=O bond that shifts towards the metalated carbon region, then

following with images 13-15 the metalated carbon and the acyl carbon both mediate towards

each other. Between image 13 and 14, a notable kink in a small peak is noted. In image 13 the

acyl group is no longer linear, and its conveying downward toward the rings metalated carbon,

which is simultaneously arching upwards to interact. The jump to image 14 gives insight to the

C-C bond formation, which occurred from another large upward bend of the ring carbon towards

the acyl carbon that has bent farther inward as well.
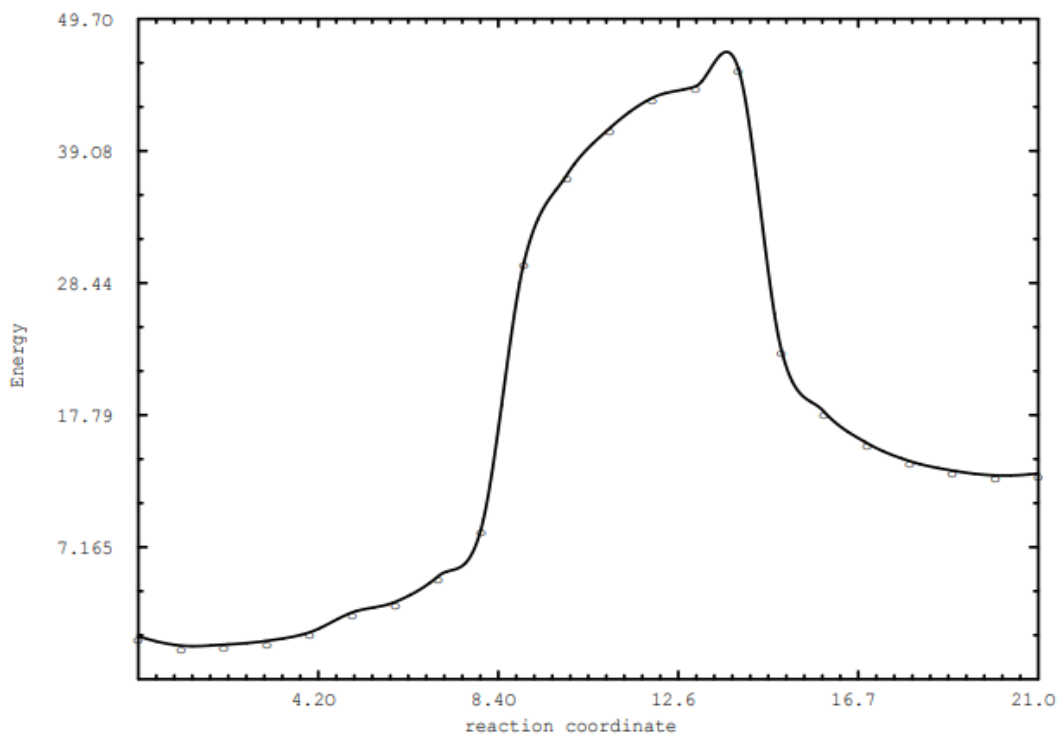
Figure 16. A2 to E1 neb curve.

Investigation of this strange neb curve has also be suggested to be a result of two different MEPs overlapping. Since the neb mapping between **A** and **E** was initially done to identify the nucleophile and further offer possible intermediates in this step, the theoretically obtained curve may not actually be predicting a true MEP. In fact, we could be observing a leap from one MEP to another, as suggested by the small hump between images 13 to 14.

Dimer optimization was still performed on the projected neb from **A2** to **E1** by using images 13 and 14. The transition state obtained had 2 negative frequencies, the first being -297.5442 and the second being -3.9105. The second negative frequency is extremely small, so it was considered numerical noise. Further validity to the possibility of hoping MEPs could be associated with the transition state found being nearly identical to the transition state between complex **B** and **E** (discussion below).

Complex **E2**, which was later optimized with the Cl⁻ ion below the platinum ring, was

recently initiated in a reaction study from complex **A2**. Interestingly, this neb simulation has

given insight to two transition states and a local minima (**figure 17**).

Barrier =   39.8321 kCal/mol   at image # 7.
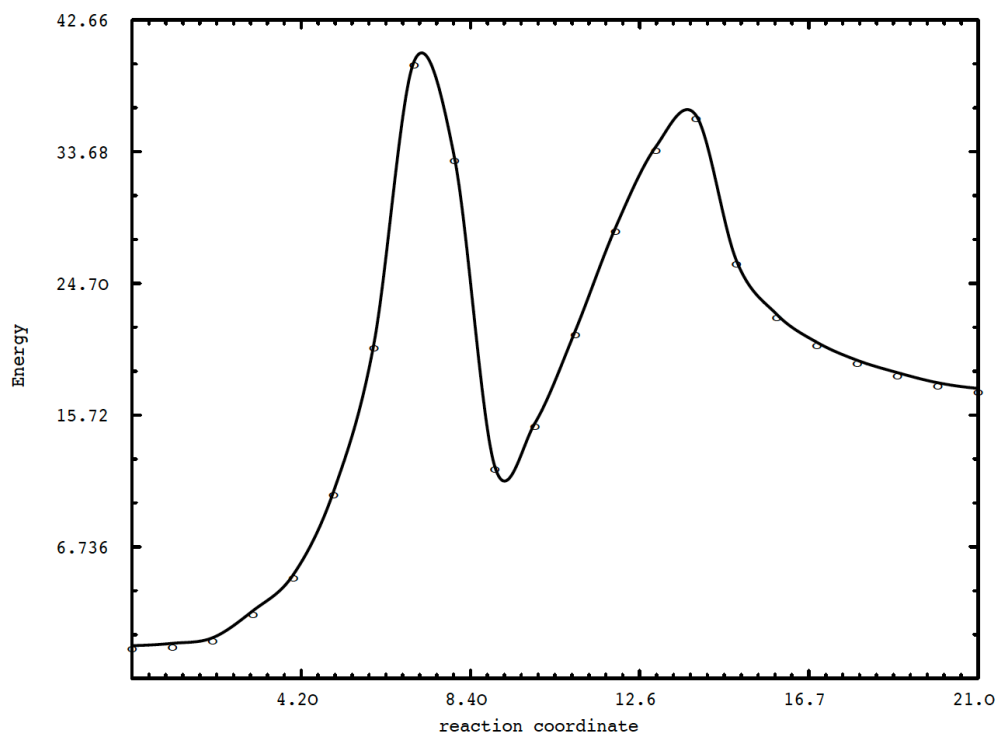
Figure 17. A2 to E2 neb curve.

Following along the images from the neb curve, the transitions occurring from image 1 -

6 are largely noted in the coordinating species. The ligand L shows rotation of the methyl group,

the coordinated chlorine to platinum is slowly getting longer and moving downwards below the

platinum ring as shown in **E2** by the Cl⁻ ion, and both ring systems coordinated to platinum are

bending upward. The acetyl chloride group has rotation of the chlorine towards the direction of

the previously coordinated chlorine to platinum's' location and with a small inward movement of

the methyl group toward the metalated carbon's ring. The Pt-Cl bond is clearly broken and more

of an interaction in image 6, with the bond length being 2.404 Å compared to its length of 2.379 Å in image 5. The large leap from image 6 to the first predicted transition state at image 7 is associated with the C-Cl bond in the acetyl chloride lengthening from 1.826 Å to 1.945 Å, respectively.

Approaching the minimum, following images 7 to 9, the C-Cl bond in acetyl chloride breaks and simultaneously Cl⁻ bonds to platinum. Following this new bond formation, the acyl group bends inward to the upward rising platinum to form the C-Pt bond. The projected minimum of image 9 displays similar characteristics to complex **D**, except Cl below the platinum ring is clearly dissociated from its 2.608 Å bond length. Image 9 was optimized and confirmed from a frequency calculation as a local minimum. Complex **D** was found to be only 0.07 kcal/mol lower in energy than image 9, and structural comparison showed their RMSD to be 0.567. The leaving chloride of the acyl group in this pathway switches places with the originally coordinated Cl in the transitioning to **E2**.

Moving towards the second predicted transition state at image 14, both ring systems are twisting upward, specifically the metalated carbon towards the carbonyl carbon of the acyl group. This transition state displays the 3 member ring between Pt-C-C(ring), which further dissociates into the desired C-C bond in the product **E2**. The second transition state, which is still under refinement, was strikingly similar to the transition state found from simulations of complex **D** to **E**, which will be discussed soon.

A to D neb mappings. As a comparison, the NEB simulation was applied for the concerted oxidative addition from **A** to complex **D**. Both **A1** and **A2** were trialed in this reaction to produce complex **D**. Only one **D** complex was able to be optimized, and the obtained structure is arguably more of a 5 coordinated platinum species with an additional interaction with one of

the two chlorines rather than a 6 coordinated complex. However, in our investigation we regarded the "interaction" as a bond in hopes to simulate the pathway without taking extra steps to account for any relativistic effects at bay from the platinum and the Cl⁻ ion. The initial mapping between **A1** to **D** was ran for 364 cycles, which led to the curve shown in **figure 18**. Climbing image was turned on at cycle 299, and the convergence seen in cycle 364 showed a molecular force of 0.00481 and a NEB force of 0.00648.

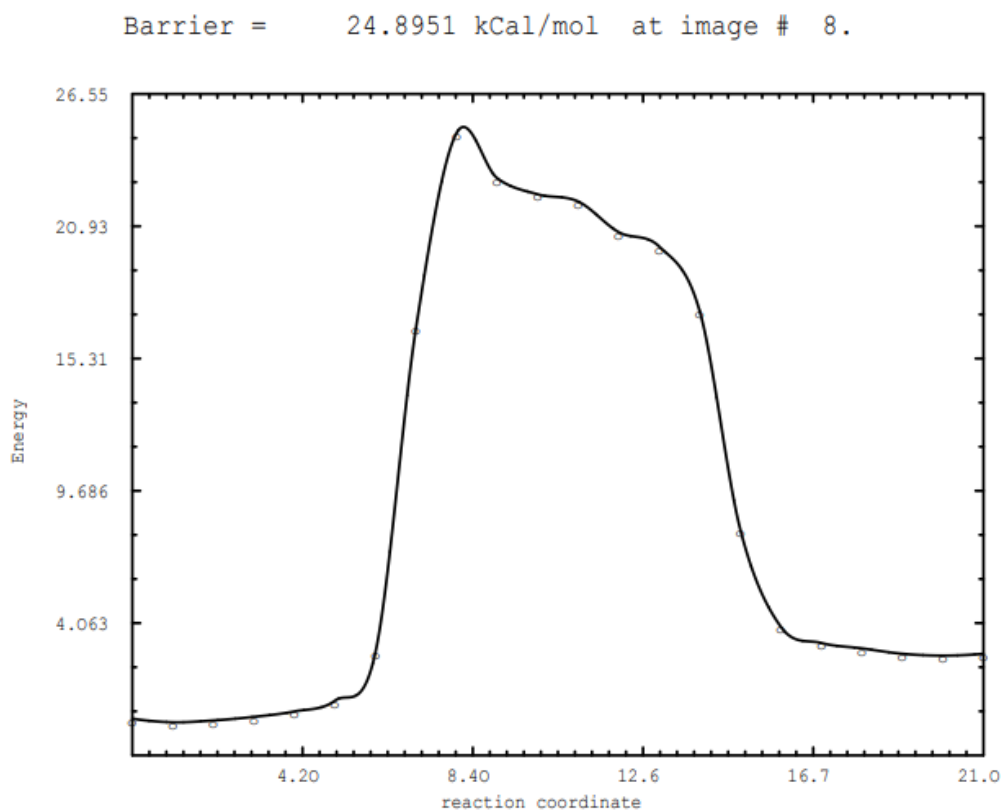Barrier =   24.8951 kCal/mol at image # 8.

Figure 18. A1 to D neb curve.

The first few image approaching the uphill climb, there is very small rotation of the methyl group on ligand L, and a slight rotation of the acetyl chloride group. Images 7 - 9 is where the C-Cl bond in acetyl chloride breaks, and the positively charged carbon remaining is

bending inward, down towards platinum. Continuing down the neb curve, images 10-12 shows the C-Pt bond has basically formed, averaging at a distance of 2.1 Å and the Cl⁻ ion leaving is circling downward between the nitrogen ring and the ligand which is in turn shifting the nitrogen of ligand L upward. Stronger C-Pt bonds are observed in images 13 - 15 and the remaining images are associated with the chlorine migrating towards the platinum to create the second Pt-Cl bond seen in complex **D**. This pathway was reevaluated using **A2** since this first obtained MEP was very rocky, therefore no further transition state refining was ever performed.

By swapping out **A1** for **A2**, the neb simulation to complex **D** was much smoother (**figure 19**). The maximum cycles were ran, but the convergence was bordering the ideal range with a molecular force of 0.00629 and a NEB force of 0.00624. Interestingly, this relatively smooth neb curve was extremely difficult once transition state refining was applied. The neb curve showed only images around the transition state location, so the images (R_1 and R_2) were ran as a dimer. The first refining optimization the default was left on, which told the dimer that R_0 and R_1 were the images imputed. However, dimer should be able to readjust in a few extra steps. This transition state obtained had 2 negativity frequencies: the first being -164.1731 and the second was -35.1507. The dimer was also re-started by turning off this default setting, but almost the same transition state was obtained with very similar negative frequencies. The key difference noted was that the two alternated which chlorine was interacting with platinum, while the other chlorine was completely dissociated.
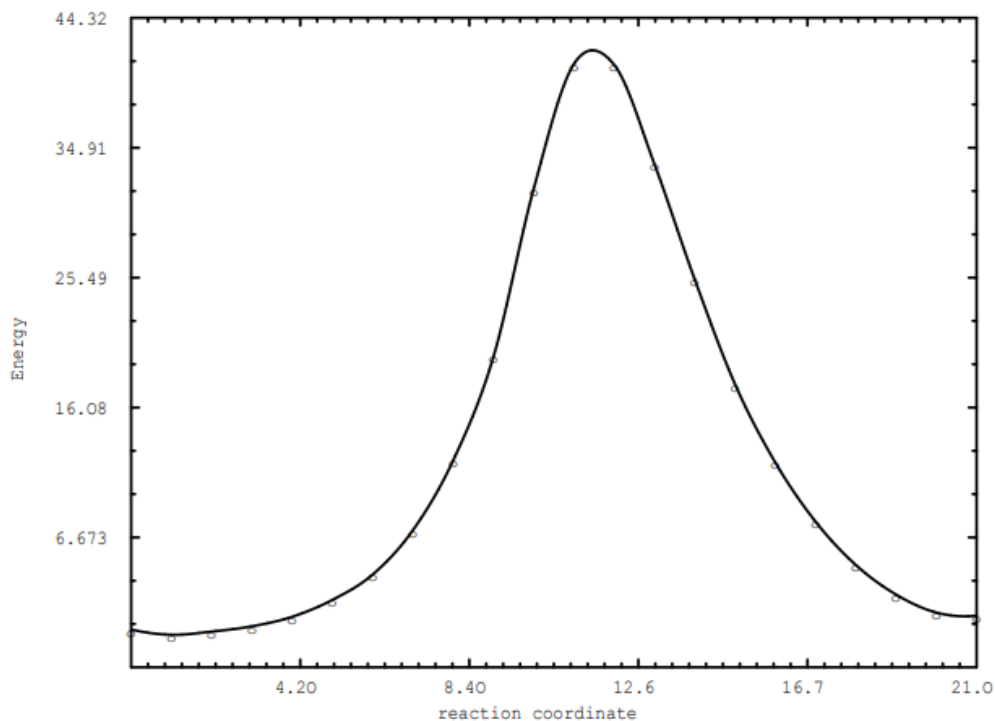
Figure 19. A2 to D neb curve.

B to E neb mappings. Formation of the desirable C-C bond occurs from the migration of the acyl group from Pt to the metalated carbon. The collaborating experimental research group study of regiosepecific acylation of cycloplatinated complexes confirmed that the acylation occurs at the metalated carbon. Therefore the simulation of complex **B** to **E** should display the 1,2 migration mechanism. The NEB was initially ran from complex **B1** to **E1**, and resulted in a very smooth neb curve (**figure 20**). The maximum cycles were ran and climbing image was turned on at cycle 288. The convergence was met, as shown by the molecular force of 0.00277 and the NEB force of 0.00265. The transition state refining from dimer was confirmed as a first order saddle point. This pathway mapping process was relatively the easiest step to map out of all the mechanistic steps in this study.

```
Barrier =      18.6905 kCal/mol   at image # 11.
```
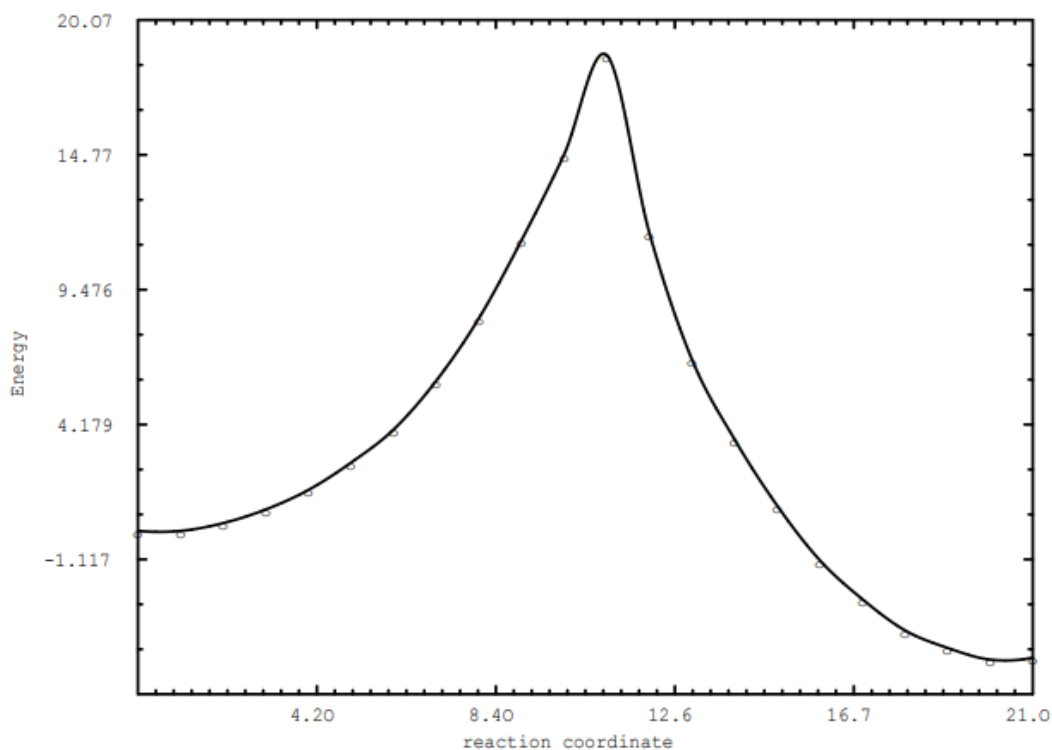
Figure 20. B1 to E1 neb curve.

Since the newest **E2** complex was later found, the additional neb simulation from **B1** to **E2** was ran using 13 images instead of 22. The neb (**figure 21**) was ran for only 179 cycles, with no climbing image incorporated, and converged fairly fast. The molecular force and neb force were 0.00337 and 0.00377, respectively. To save time, the transition state refining was done using QST2 method, and confirmed with one negative frequency (-302.9779). The projected MEP curve is much broader than the original simulation, which can be correlated to less images, less cycles ran, and no usage of thee climbing image feature.
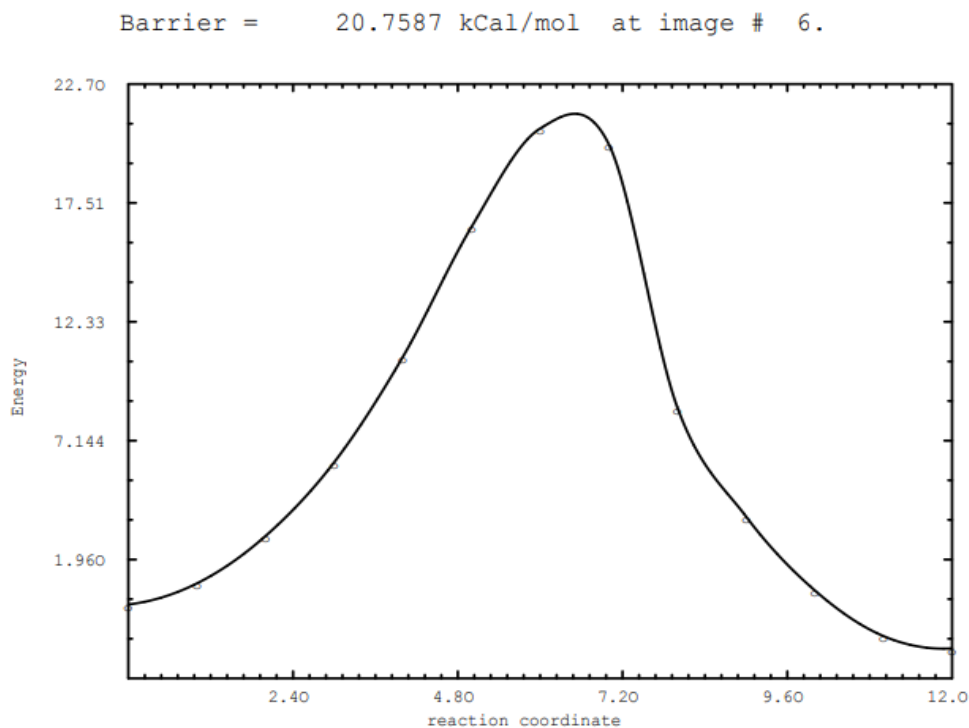
Figure 21. B1 to E2 neb curve.

In addition to running the above two neb simulations, the same runs were ran using complex **B2**. The neb for **B2** to **E1**, shown in **figure 22** below, ran 352 cycles with no climbing image enabled. This simulation had the best convergence, with a molecular force of 0.00156 and a NEB force of 0.00300. Dimer optimization obtained a 1st order saddle point using images 5 and 7, R_1 and R_2, with a single negative frequency of -298.9843. the decision to optimize the transition state with images surrounding the projected transition state at image 6 allowed for a better pull between a more reactant and more product like species.

Barrier =   18.4607 kCal/mol   at image # 6.
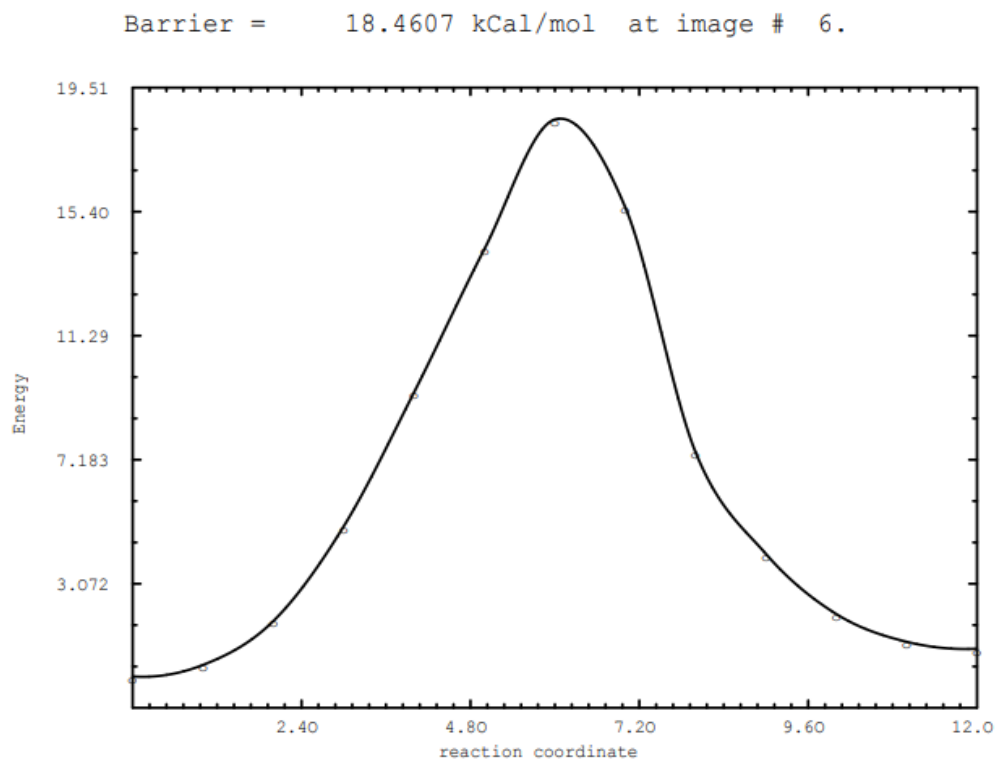
Figure 22. B2 to E1 neb curve.

Lastly, **B5** to **E2** was ran with 13 images for 243 cycles (**figure 23**). The neb convergence

criteria was met with a molecular force of 0.00231 and a NEB force of 0.00255. As noted in the

additional **B** to **E** neb simulations, all calculations aside from the first neb was ran with 13

images and without usage of the climbing image feature. Therefore, all these curves are much

broader. In this neb, the two images near the projected transition state were used, images 6 and 7,

in a dimer optimization. The conformation frequency calculation, however, gave 2 negative

frequencies (-308.024 and -26.5108). The latter of the two is small enough to assume its

numerical noise though.

69
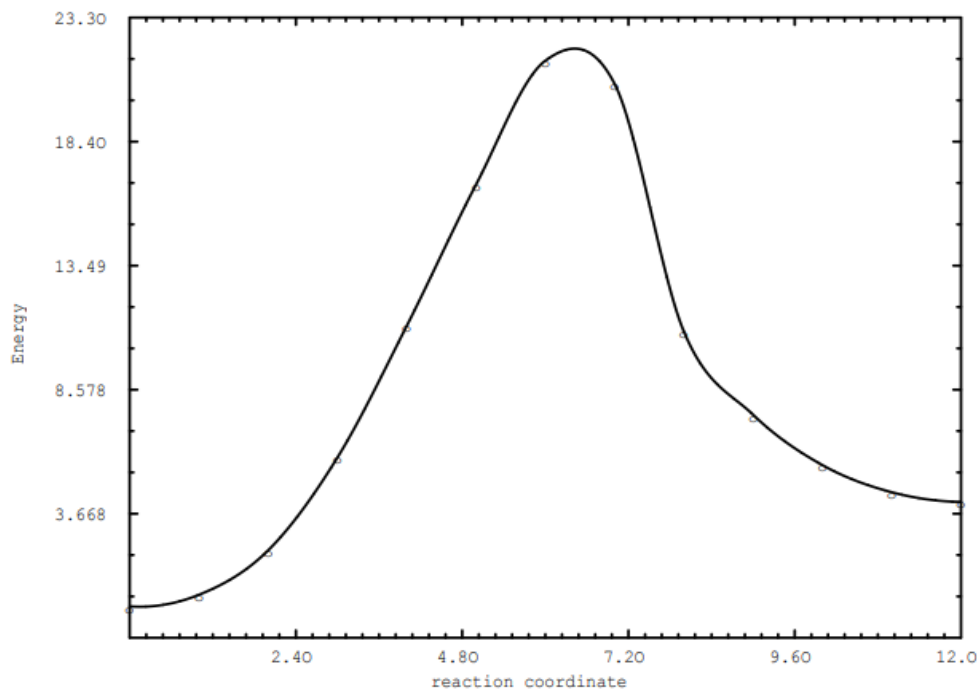
Figure 23. B2 to E2 neb curve.

B to D neb mappings. Trapping of five-coordinated intermediate **B** by a chloride produces the oxidative addition product **D**. The first neb was ran between **B1** and **D**. In this pathway, the Cl⁻ ion is migrating from its stabilized location in complex **B1** to bond to platinum in complex **D**. Using only 13 images, a very low barrier MEP was obtained in **figure 24**. 241 cycles were ran, without using the climbing image feature. Convergence was met, as the molecular force was 0.00120 and the neb force was 0.00241. several transition state refining techniques were employed, but the best numerical calculation was observed from the dimer optimization between images 4 and 5. However, the very low negative frequency of -34.9526 is arguably numerical noise. Therefore we cannot confirm identification of a true first order saddle point transition state from this MEP.

70
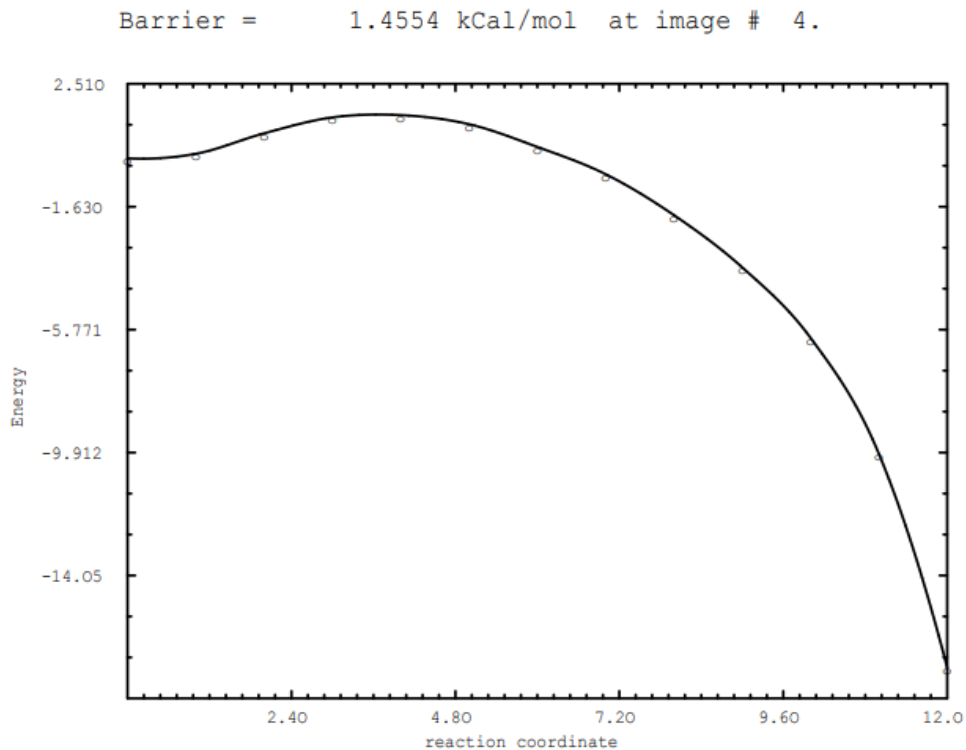
Figure 24. B1 to D neb curve.

Employing 22 images for an alternate simulation between **B2** and **D** was ran and observed an somewhat better MEP (**figure 25**). Only 117 cycles were ran, but convergence was met without using climbing image. Both the molecular force and neb force was 0.00204. Dimer optimization was performed using images 8 and 9, and obtained a better transition state than the previous simulation of **B1** to **D**. Based on the single negative frequency, -62.3069, we are borderline to the numerical noise region (0 to -60). The QST2 optimization resulted in an even lower single negative frequency (-31.5885). Mapping of the chloride trapping step has been quite a challenge, and so far we haven't seen success from alternating between different transition state refining tools. This may indicate an alternative level of theory and basis set may need to be trialed to overcome the strong relativistic effects of platinum and the Cl^- ion. Unfortunately, this would need to be performed in future work as this would require all calculations to be re-

71

optimized starting at the complex optimization step. Also, employment of larger basis sets and

more images is computationally expensive, so the means to perform this work may exceed

current computational tools at the university.
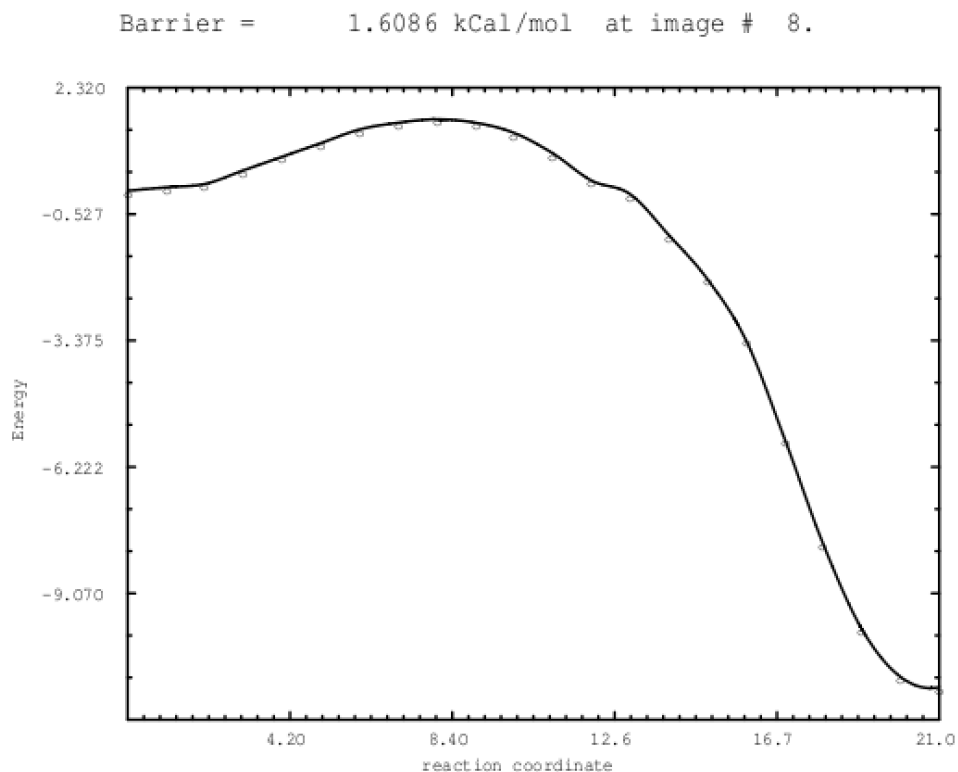
Figure 25. B2 to D neb curve.

D to E neb mappings. From speculation of complex **B** and **D** varying based on Cl⁻

location, and that complex **D** Pt-Cl bond is arguably an interaction, the mapping of complex **D** to

E was performed. **D1** to complex **E1** is mapped below in **figure 26**. A total of 450 cycles were

ran, using climbing image starting at cycle 306. The neb converged at a molecular force of

0.00237 and an neb force of 0.00367. The neb produced an image, image 6, associated with R_0,

so it was refined using a Berny algorithm calculation first. This optimization was pulled from an

earlier neb cycle, but this method failed as no negative frequencies were obtained. From cycle

450, another Berny algorithm was performed, but the obtained transition state had a low single

negative frequency (-76.3233). Additional utilization of the dimer method may produce a more

reasonable transition state, however this calculation has not yet been performed. Instead the

alternative **E2** complex was employed for a neb simulation.

Barrier =   30.1805 kCal/mol   at image #   6.
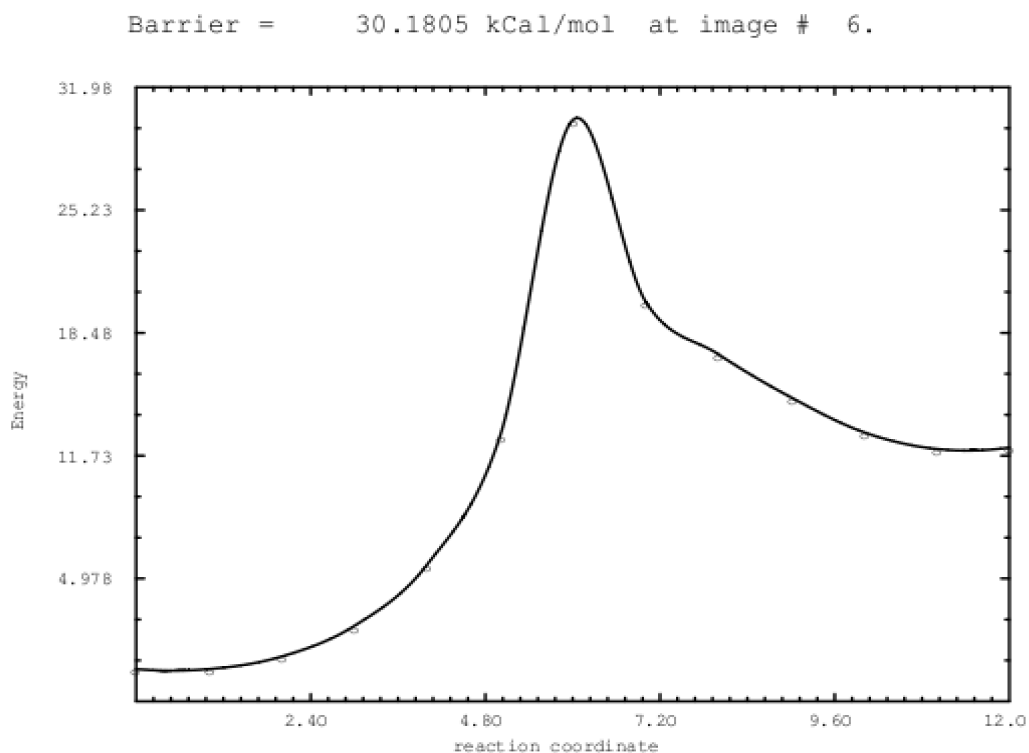
Figure 26. D1 to E1 neb curve.

With the same amount of images, the neb between **D1** and **E2** was ran for 200 cycles and

no climbing image usage (**figure 27**). Convergence was met; The molecular force was 0.00354

and the neb force was 0.00240. The mapped images near the projected transition state lied on

either side of the true transition state, so both a dimer and QST2 refining methods were applied.

Both verified a first order saddle point with single negative frequencies of -319.5134 and -

318.4235, respectively. The two transition states differed only by 0.12 kcal/mol, the QST2

method giving the lower energy structure.
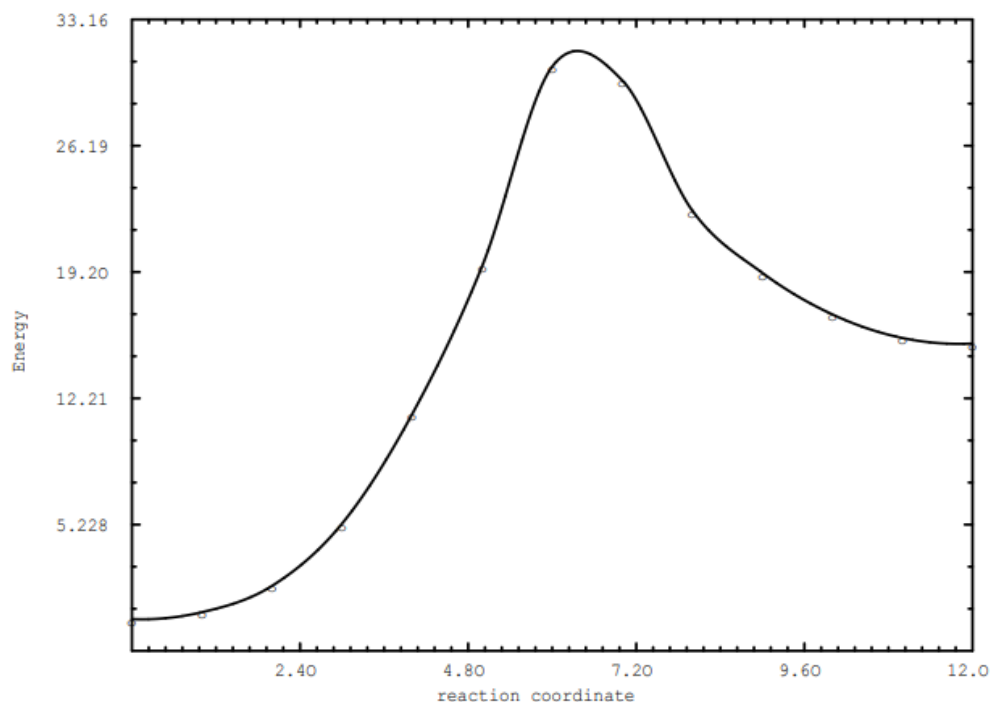
Figure 27. D1 to E2 neb curve.

E to P neb mappings. One of the last connecting piece to this mechanism was the reaction from **E** to **P**, where aromatization is re-established. This occurs through reductive elimination of platinacyclopropane (**E**) or a ligand substitution of the Pt-arene complex with a chloride. The biggest challenge associated with this neb simulation comes from complex **E** and **P** having the ligand L and the coordinated chlorine bonded to platinum on opposite sides. The first neb was ran in reverse, from complex **P1** to **E1** (**figure 28**). A total of 360 cycles were ran, and convergence was reached based on the molecular and neb forces (0.00138, 0.00226). However, with only 13 images were used, the mapped MEP may have missed a potential minima. From the neb curve, a dimer optimized transition state was produced with a single negative frequency (-147.0385). Based on its structure and vibrational mode assay, this isn't the true transition state for this step.
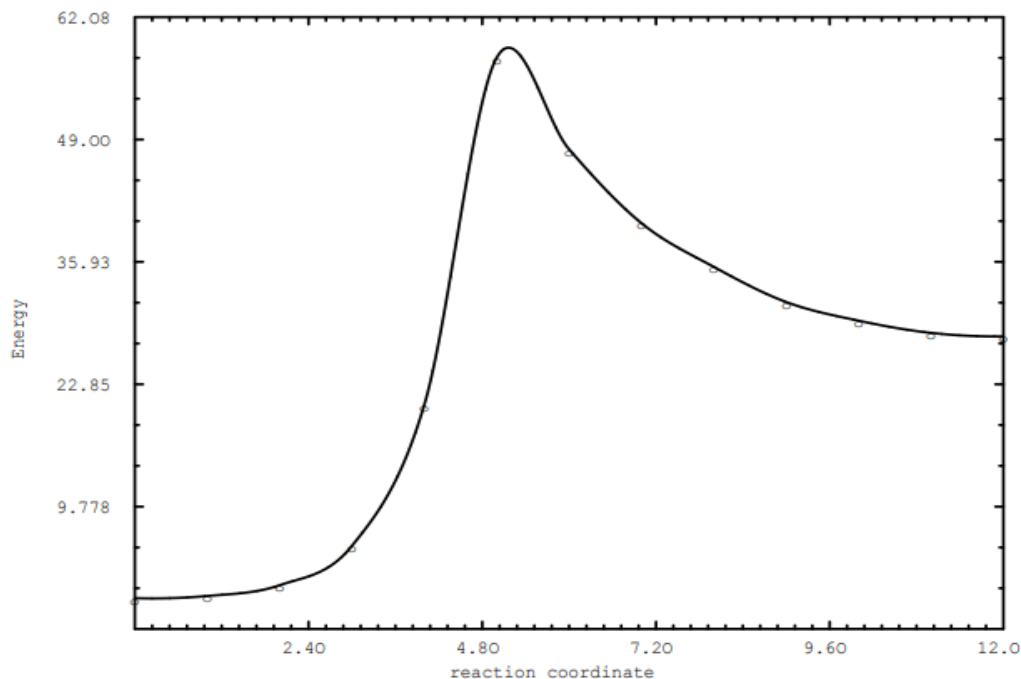
Figure 28. P1 to E1 neb curve.

Another trial using complex **E2** was ran, this time directly from **E2** to **P1** (**figure 29**). The maximum cycles were ran, no climbing image was turned on, and convergence of both molecular and neb forces were met (0.00192, 0.00289). Images 5 and 6, lying on either side of the predicted transition state, were optimized using dimer. Unfortunately, a very similar structure, as seen in **P1** to **E1** simulations, was found. The first order saddle point was verified, and interestingly its single negative frequency was comparable to the other (-134.0394). Another interesting note was the QST2 optimization of the same images gave all positive frequencies.
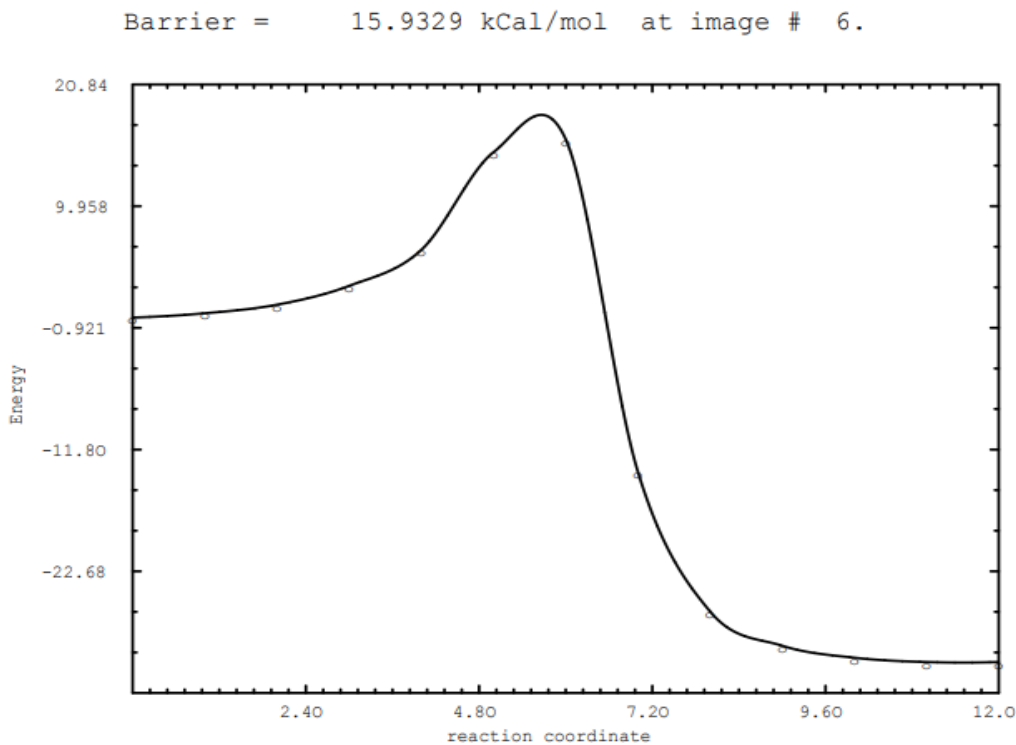
Figure 29. E2 to P1 neb curve.

Due to neither of these simulations re-aromatization pathway mappings leading to true transition states, current calculations are being performed. The main challenge currently being faced is the ligand L location in all optimized structures as depicted in **scheme 13**, versus its location in complex **P**. The initial built **P** structure was created as shown in **scheme 13**, yet through numerous optimization trials the structure finally converged with the L and Cl swapped. The overall energy of this swapped structure is the lowest energy species by over 10 kcal/mol, but the addition of these reactions came months after the structures were optimized in the initial conformation and ran through numerous MEP mapping and transition state localizations.

D to P neb mapping. Reductive elimination often follows oxidative addition, and its frequently proposed in literature for metal catalyzed C-H activation. The oxidative addition product denoted as complex **D** is transformed to complex **P1** through reductive elimination. This

step was simulated below in **figure 30**. The maximum cycles were ran, with climbing image started at cycle 334. The neb converged as seen from its molecular force and neb force of 0.00396. A dimer optimization was ran using the barrier image 10, and the second closet image 9. Both offered a more reactant like species and more product like species based on the images structures. Image 8 shows the acyl group migrating towards the metalated carbon, and simultaneously the Pt-C bond starts lengthening slightly. This Pt-C bond shows the C shifting upward towards the acyl group as Pt shifts up and away. A confirmed first order saddle point was obtained, with a negative frequency of -319.4287. The vibrational mode observed showed only the migration of the carbonyl acyl carbon towards the metalated ring occurring. The transition state favors the previously observed 3 member ring formation between Pt-C(acyl)-C(ring), which is noted in several obtained transition states.

Barrier =   45.7304 kCal/mol   at image # 10.
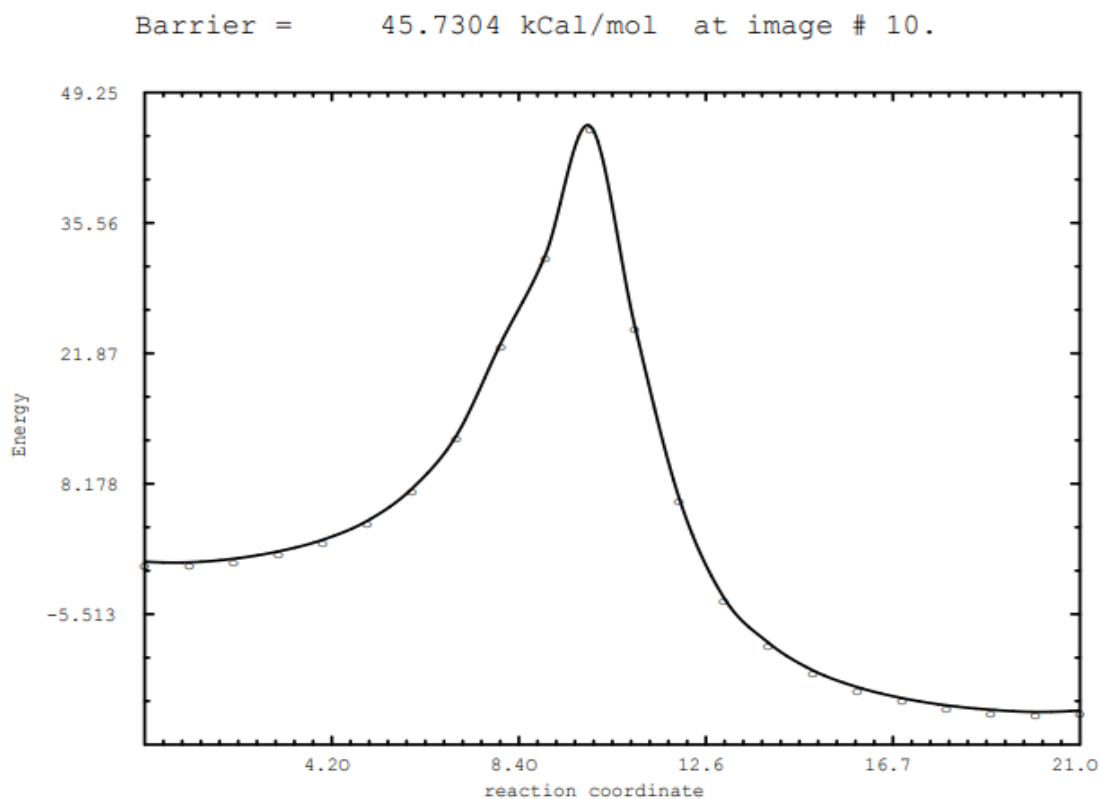
Figure 30. D to P1 neb curve.

3.3.3 Transition State Localizations

Only the most reasonable optimization transition states are presented for discussion. The presented transition states are all confirmed by their single negative frequencies, and/or kept if their second negative frequency can be classified as numerical noise. Any invalidity of true transition states based on vibrational mode analysis or unreasonable transitions between two stationary points will be evaluated in each steps section for discussion. However, all the transition states, regardless of the prevailing vibrational mode assays, are still presented in **table 8**. All mapped MEP have only one of the optimized transition state structures presented for discussion. The most reasonable and/or lowest energetic structures were chosen and their energy profiles are shown in **table 8**.

Table 8. Evaluation of Each Mapped Neb's Optimized Transition State Energy Profiles. HF energies from optimization, Zero-Point Correction factor from frequency, and their combined Zero- Point Correction Energy value in units of Hartee/Particle.

Transition States Indicated by the Two Stationary Points used in their Simulation			
	A1-B1	**A2-B1**	**A2-B3**	**A2-E1**
HF	-1879.563208	-1879.561116	-1879.561591	-1879.542167
ZPC	0.262671	0.262091	0.262586	0.262284
HF-ZPC	-1879.3005	-1879.2990	-1879.2990	-1879.2799
	A2-D	**B1-E1**	**B1-E2**	**B2-E1**
HF	-1879.537863	-1879.542545	-1879.543094	-1879.54171
ZPC	0.262627	0.262466	0.262728	0.262643
HF-ZPC	-1879.2752	-1879.2801	-1879.2804	-1879.2791
	B2-E2	**B2-D**	**D-E1**	**D-E2**
HF	-1879.537859	-1879.573516	-1879.575077	-1879.537716
ZPC	0.262239	0.262926	0.26347	0.262434
HF-ZPC	-1879.2756	-1879.3106	-1879.3116	-1879.2753
	P-E1	**E2-P**	**Bart-E-P**	**D-P**
HF	-1879.540470	-1879.541002	-1879.626231	-1879.537711
ZPC	0.263126	0.263352	0.2645616	0.262396
HF-ZPC	-1879.2773	-1879.2777	-1879.3617	-1879.2753
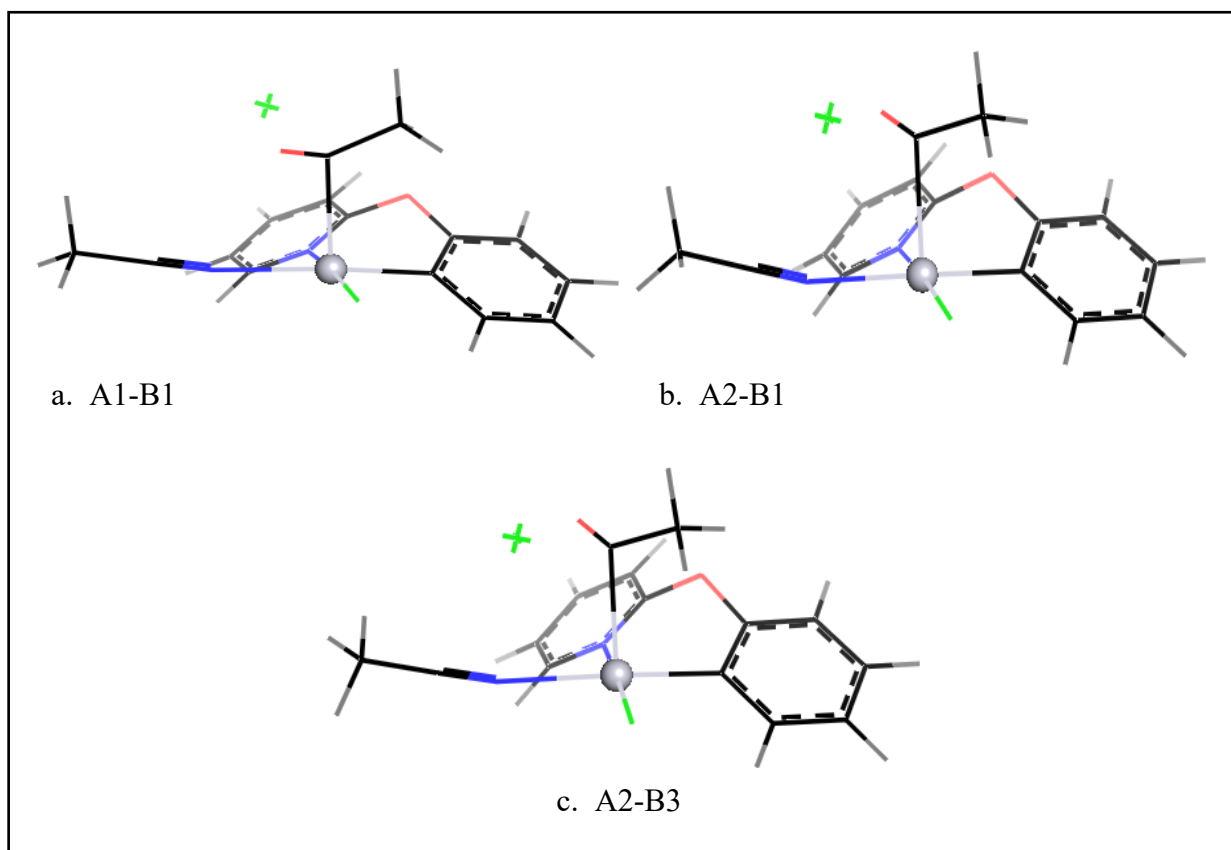
Figure 31a-c. All Transition State Complexes between A and B located, Optimized and Confirmed through Vibrational Mode Analysis.

Table 9. All Transition States Localized Between A and B Complexes.

Bond Length (Å)	A1-B1	A2-B1	A2-B3
Pt - L	2.2309	2.2051	2.2062
Pt - N	2.0621	2.0713	2.0763
Pt – C_R	1.9745	1.9750	1.9755
Pt - Cl_1	2.3481	2.3267	2.3283
Pt - C_a	2.3343	2.3735	2.3391
Pt – Cl_2	3.6935	3.8871	3.7961
C_a - C_R	3.3024	3.1907	3.1652
C_a - Cl_2	2.5579	2.5466	2.5058
Pt - C_{ox}	2.9344	2.9205	2.9236

Pt - C$_{far}$	4.2572	4.2449	4.2501
Bond Angles (°)			
C$_a$ - Pt - C$_R$	99.7	94.0	94.0
L - N - C$_R$ - Cl	1.0	2.2	1.4

In terms of both structure (**figure 31, table 9**) and energy (**table 8**), all transition states found are inherently similar. Even with modifications to the initial stationary points used to initiate the trajectory of the MEP, their refined transition states are roughly the same. For transition state between **A1-B1** (**figure 31a**), it resulted in the lowest energy. However, the energy difference in reference to the other two transition states was only about 1 kcal/mol. The energy difference between **A2-B1**(**figure 31b**) and **A2-B3** (**figure 31c**) transition states was even smaller, with a difference of 0.0127 kcal/mol.
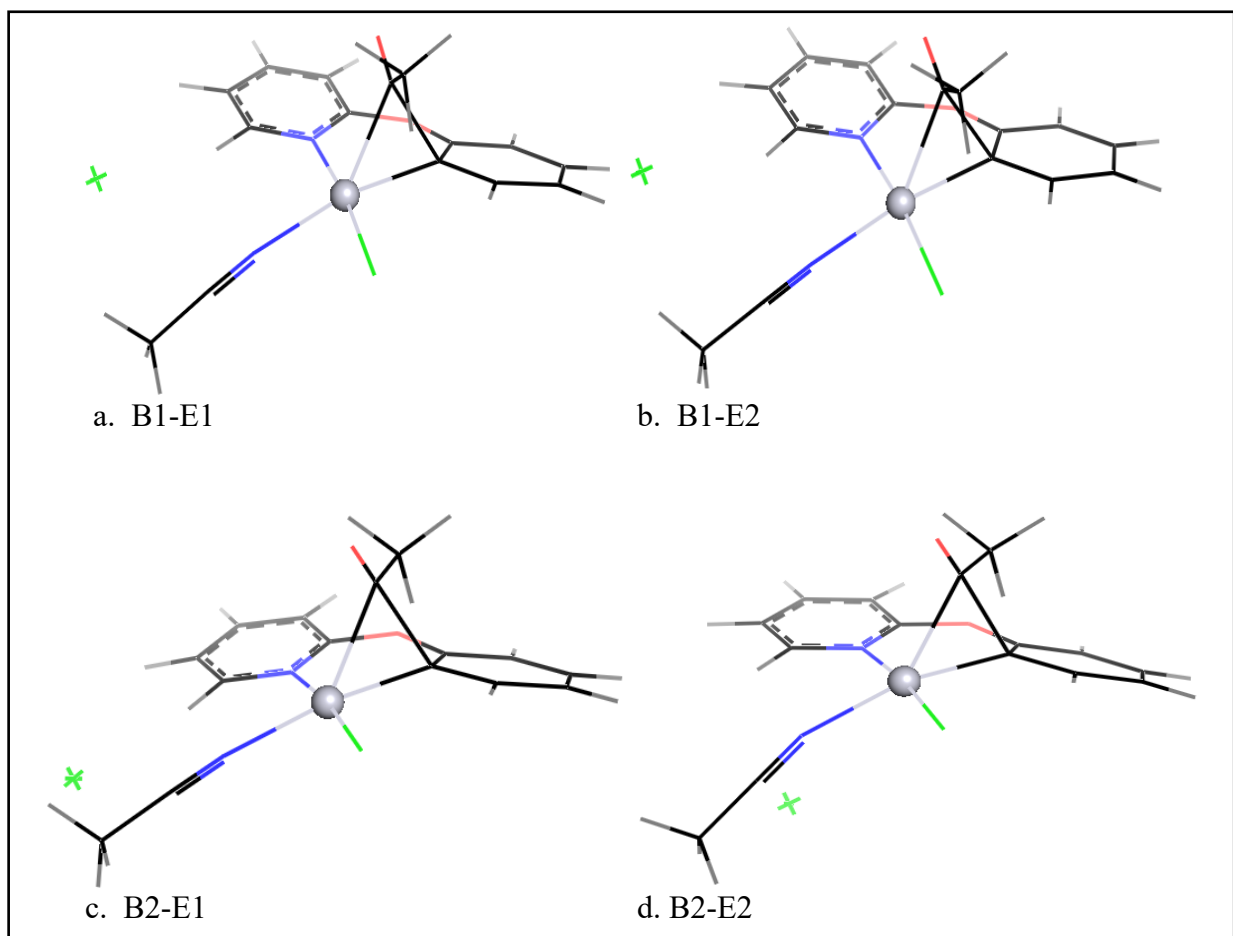
Figure 32a-d. All Transition State Complexes between B and E located, Optimized and Confirmed through Vibrational Mode Analysis.

Table 10. All Transition States Localized Between B and E Complexes.

Bond Length (Å)	B1-E1	B1-E2	B2-E1	B2-E2
Pt - L	2.1111	2.1124	2.1191	2.1191
Pt - N	2.0597	2.0632	2.0924	2.0872
Pt – C_R	2.0397	2.0423	2.0439	2.0430
Pt - Cl_1	2.3492	2.3422	2.3432	2.3453
Pt - C_a	2.2965	2.3166	2.2964	2.2898
Pt – Cl_2	5.1950	5.2556	5.2833	4.2746
C_a - C_R	1.9269	1.9117	1.9028	1.9028
C_a - Cl_2	6.4326	6.2888	6.9483	6.2816
Pt - C_{ox}	2.9528	2.9566	2.9929	2.9819
Pt - C_{far}	4.2377	4.2443	4.2740	4.2603

Bond Angles (°)				
C_a - Pt - C_R	52.4	51.6	51.6	51.7
L - N - C_R - Cl	-8.1	-4.3	-3.4	-9.0

We have refined several transition states for the 1,2-migration mechanism between complex **B** and **E**. Predominately, the investigation zoned into identifying the preferred location of the Cl⁻, and how to best isolate this ion in two connecting stationary points. In **B1** versus **B2** (**figure 8a-b**), the Cl⁻ ion is optimized father around the nitrogen ring, whereas in **B2** it is found between thee nitrogen ring and the ligand. **E1** (**figure 9a**) has the Cl⁻ ion optimized in a similar position shown in **B2**, whereas **E2** (**figure 9b**) has this ion placed below the platinum ring. Based on the geometries of all transition states localized, we can assume the transition state of the 1,2-migration does involve the formation of a 3-membered cyclic ring. This ring formation is essentially the second step of C-H functionalization where the M-C bond transforms to a C-C bond. Formation of the 3-member ring in turn causes the metalated carbon ring to lose aromaticity.

The differences with these structures is mainly location of the Cl⁻ ion, and its effect on the coordinated ligand (acetonitrile) relativity effect. The Cl⁻ ion tends to optimize in about 2.5 Å to a hydrogen in almost all optimizations, therefore the bending of this ligand's methyl group could be a result of this noted trend. In terms of energy (**table 8**), the transition states found between **B1** complexes were of lower energy. The highest energy transition state was seen from the mapping of **B2** to **E2** (**figure 32d**), and this state was 2.98 kcal/mol higher in energy than the transition state from **B1** to **E2** (the lowest energy TS; **figure 32b**). Additionally, the energy difference may largely be in association to the Cl⁻ ion's location, as this ion seems to dictate the key structural differences.

Figure 33. The Located Transition State Complex between A2 and E1 Optimized and Confirmed through Vibrational Mode Analysis.

Table 11. Current Confirmed Transition States Found Between A2 and E1 Complexes.

Bond Length (Å)	A2-E1
Pt - L	2.1049
Pt - N	2.0579
Pt – C_R	2.0402
Pt - Cl_1	2.3441
Pt - C_a	2.3289
Pt – Cl_2	4.9120
C_a - C_R	1.9166
C_a - Cl_2	5.6796
Pt - C_{ox}	2.9479
Pt - C_{far}	4.2349
Bond Angles (°)	
C_a - Pt - C_R	51.5
L - N - C_R - Cl	-4.9

Only one transition state is presented between **A** and **E** complexes. Currently, two additional transition states are being refined from mapping of **A2** to **E2**, as shown from the neb curve in **figure 17**. In regards to the presented transition state (**figure 33**), it has been confirmed

by its vibrational mode analysis, but in reference to its neb curve in figure 16 may indicate the

TS obtained was as a result of a transition state from a different MEP. Originally, we assumed

the initial trajectory of A-E would display two local maxima and a local minima during

simulations. However, as seen in **figure 16**, the curve seems to jump around images 13 and 14. A

possible indication of transitioning onto a close lying MEP for different connecting stationary

points, possibly the points of B-E. Further insight into this can be based on the strikingly

resemblance of this intermediate to the ones seen from the reaction of **B** to **E**. Both transition

states formed this 3-member ring, which showed loss of aromaticity in the metalated carbons

rings. Also, both A-E and B-E transition states resemble the proposed complex **C**, which was

never able to be optimized. The newest data will hopefully provide further insight to this theory
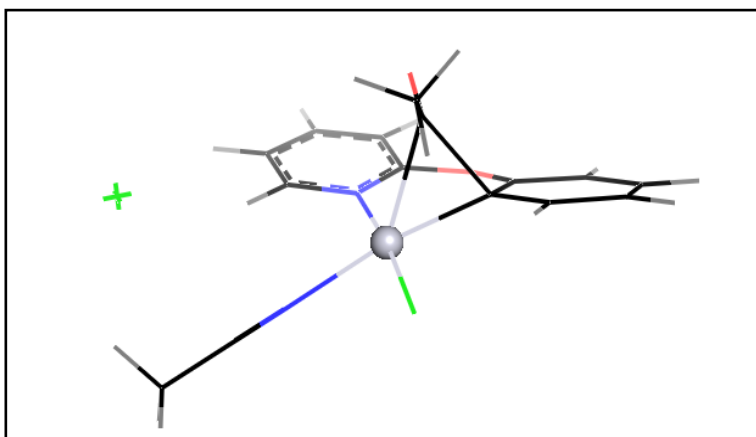
and if there is an actual minima in-between A-E.

Figure 34. The Located Transition State Complex between A2 and D1 Optimized and
Confirmed through Vibrational Mode Analysis.

Table 12. Transition State Between A2 and D1.

Bond Length (Å)	A2-D
Pt - L	2.2358
Pt - N	2.0410

Pt – C_R	1.9764
Pt - Cl_1	2.5109
Pt - C_a	2.1888
Pt – Cl_2	2.8946
C_a - C_R	3.0281
C_a - Cl_2	2.3997
Pt - C_{ox}	2.9342
Pt - C_{far}	4.2566
Bond Angles (°)	
C_a - Pt - C_R	93.1
L - N - C_R - Cl	30.7

Only one transition state was localized between the concerted oxidative addition pathway

from complex **A2** to complex **D1** (**figure 34**). From the transition states vibrational mode

analysis, it shows the Pt-C bond breaking and the Cl⁻ ion leaving simultaneously. Once the Cl⁻

ion is out of interaction range of the acyl carbon, then the Cl⁻ comes closer towards the Pt. As

this movement occurs, the nitrogen ring seems to pull in closer into Pt. The transition state was

confirmed with its single negative frequency of -164.1731. However, this Pt – Cl_2 bond distance

(**table 12**) isn't even in range of considered interaction. It could be in association to the large

relativistic affects at play not only on platinum, but this negatively charged chloride ion as well.
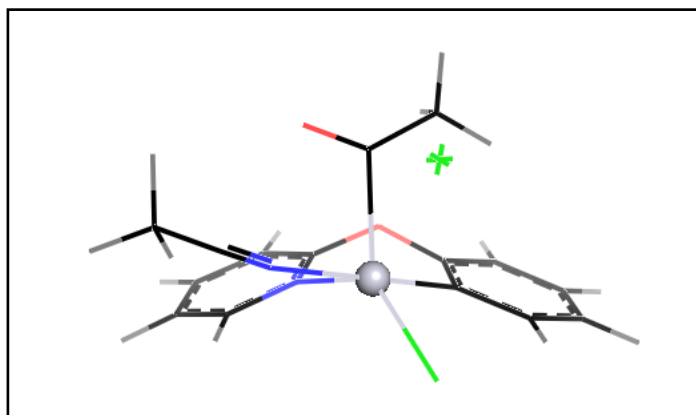
Figure 35. The Located Transition State Complex between B2 and D1 Optimized and Confirmed through Vibrational Mode Analysis.

Table 13. Transition State Between B2 and D1.

Bond Length (Å)	B2-D
Pt - L	2.2292
Pt - N	2.0605
Pt – C_R	1.9808
Pt - Cl_1	2.3277
Pt - C_a	2.0455
Pt – Cl_2	3.9342
C_a - C_R	2.9027
C_a - Cl_2	5.7296
Pt - C_{ox}	2.9116
Pt - C_{far}	4.2372
Bond Angles (°)	
C_a - Pt - C_R	92.2
L - N - C_R - Cl	1.4

Mapping of the ligand substitution/trapping of five-coordinate Pt(IV) complex **B** to obtained complex **D** has been extremely challenging. First, an neb was mapped between **B1** to **D1** (**figure 24**), which showed an extremely low barrier prior to any transition state refining.

Upon refining any of the projected transition states, the MEP displays a higher barrier than the one obtained after further optimization. Therefore, working with a MEP barrier from neb of about 1.5 kcal/mol has had little success. The **B1-D1** transition state structurally was unreasonable, as the Cl⁻ ion was essentially lost and it had a very lower single negative frequency of -34.9526.

A step up from **B1-D1** was seen in the mapping of **B2-D1** (**figure 25**). In complex **B2** (**figure 8b**) the Cl⁻ ion is optimized in a more reasonable location for the migration over to platinum to create complex **D1** (**figure 10**). Whereas, complex **B1** (**figure 8a**) had to have the Cl⁻ ion travel across the nitrogen ring to even get in close proximity of platinum. The obtained transition state (**figure 35**) shows the best projection for this reaction obtained thus far. However, based on its negative frequency being -62.3069, it boarders being validified by this numerical conformation of first order saddle points. For a more solidified transition state, multiple basis sets and methods should be applied to map this heavily relativity step.
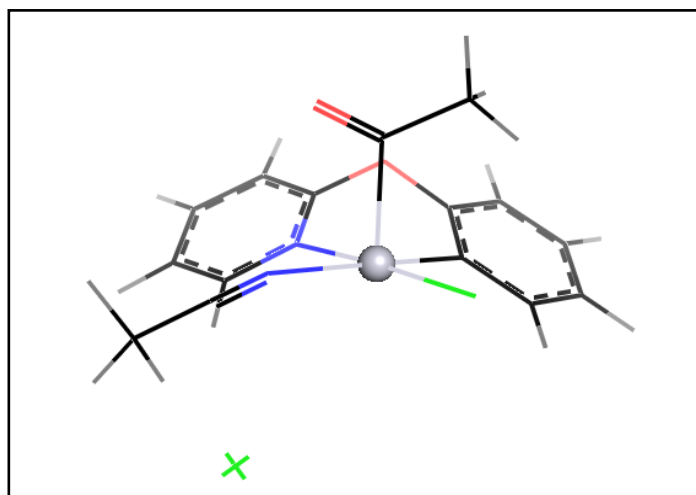

Figure 36. The Located Transition State Complex between D1 and P1 Optimized and Confirmed through Vibrational Mode Analysis.

Table 14. Transition State Between D1 and P1.

Bond Length (Å)	D-P
Pt - L	2.1289
Pt - N	2.0670
Pt – C_R	2.0376
Pt - Cl_1	2.3510
Pt - C_a	2.2628
Pt – Cl_2	3.2097
C_a - C_R	1.8749
Pt - C_{ox}	2.9467
Pt - C_{far}	4.2228
Bond Angles (°)	
C_a - Pt - C_R	51.2
L - N - C_R - Cl	-8.6

Observation into the reductive elimination between **D1-P1** shows some interesting features similar to the **B-E** (**figure 32**) and **A-E** (**figure 33**) simulations. In all 3, the observed transition state has this 3-member ring interaction prior to isolating of the C-C bond. However, in **D1-P1** transition state (**figure 36**), the Cl⁻ ion is seemingly lost rather than in a closer interaction to Pt. Loss of this ion is not a reasonable projection for mapping **D-P**, as the **P** complex should have both chlorines attached. Even though this transition state is confirmed as a first order saddle point from its frequency calculation (-319.4287), it may not be the transition state lying on this MEP.

In the vibrational mode analysis, the lost chlorine shows no movement, therefore we can assume from this state that product **P** may not connect. We do observe the acetonitrile's N-Pt bond strengthen as the Pt-C_a bond weakens, which is the result of the Pt-C bond transformation to the C-C bond in this step. However, platinum's bond to the metalated carbon barely fluctuates and could assume no breaking is observed by such small movements.

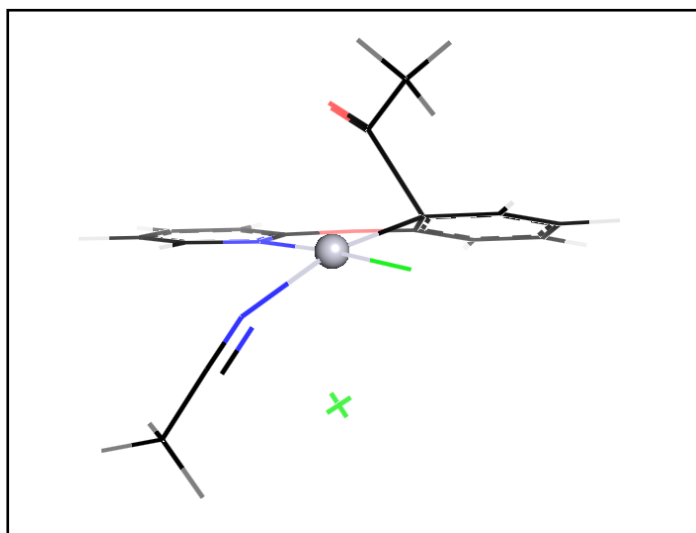a. P1-E1   b. E2-P1
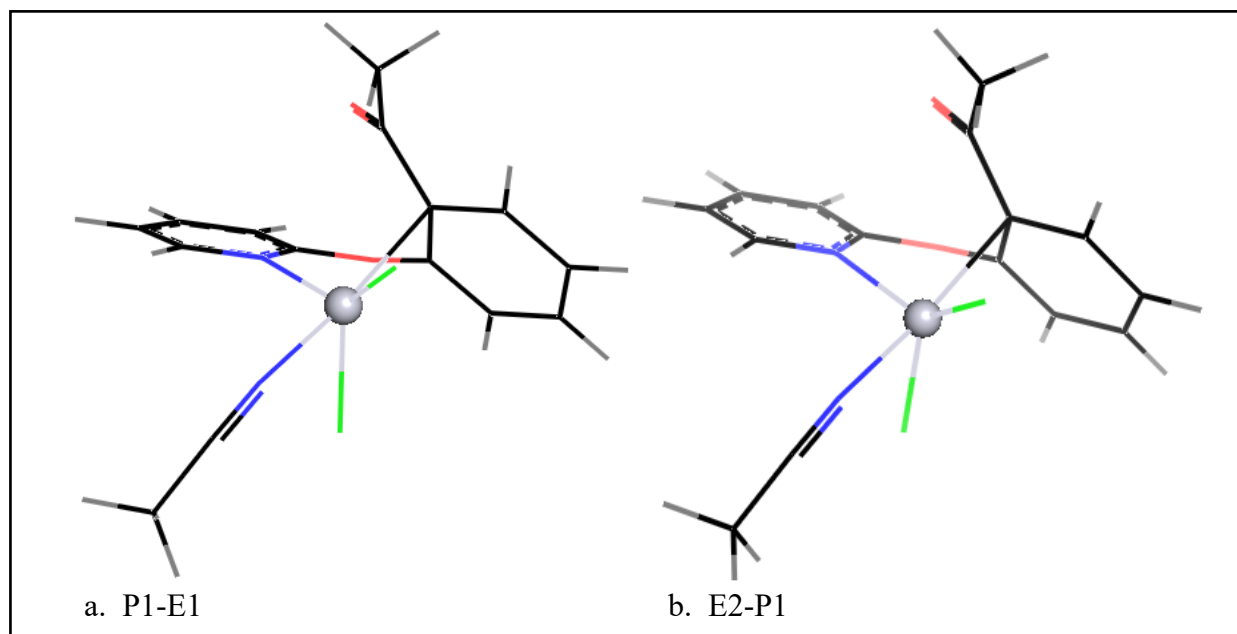
Figure 37ab. All Transition State Complexes between P and E located, Optimized and Confirmed through Vibrational Mode Analysis.

Table 15. Transition State Between P and E.

Bond Length (Å)	P-E1	E2-P
Pt - L	1.9395	1.9395
Pt - N	2.4661	2.4654
Pt – C_R	2.4248	2.4111
Pt - Cl_1	2.3335	2.3334
Pt - C_a	3.1712	3.1482
Pt – Cl_2	2.772	2.7816
C_a - C_R	1.5177	1.5186
C_a - Cl_2	5.0734	5.0664
Pt - C_{ox}	2.834	2.8714
Pt - C_{far}	3.5626	3.619
Bond Angles (°)		
C_a -Pt - C_R	27.6	27.9
L - N - C_R - Cl	-20.7	-21.4

In hindsight, we simulated the re-aromatization in **scheme 13** (**E-P**) in reverse; connecting **P-E** to join the two tailing studies. The final product, complex **P**, is the lowest energy species optimized. However, with complex **P** being a later addition to the theoretical investigation, the optimized location of its ligand L gave insight to a feature that was not investigated in the beginning of this study. Now, in addition to all the encountered challenges so far in the mapping process, the addition of the location of coordinated ligand and chloride added in to the difficulty.

The projected MEP from **P1** to **E1**, shown in **figure 28**, is relatively smooth and we would assume a simple refinement of the projected transition state would result in a reasonable optimized transition state. Based on the vibrational mode assay, the only movement observed is in relation to all other irrelevant ligands except the de-aromatization of platinum interacting with two carbons in the metalated carbon ring. When mapping **P1** to **E1**, we should observe de-aromatization from the metalated carbon and its neighboring C_{ox} interacting with platinum, prior to full bond formation as seen in complex **E1**. Additionally we should observe the swapping of the ligand L with the coordinated Cl. The movement observed seems to be in relation to platinum re-establishing its coordination with the nitrogen in the ring, which may have been lost from the ligand swapping. The transition state shows Pt-C_R in a reasonable interacting bond distance (**table 15**), but the second needed Pt ring interaction (Pt-C_{ox}) shows a distance too large to assume interaction is occurring. This **P1-E1** transition state (**figure 37a**), in fact, may be relatively reasonable in terms of both 1st order saddle point conformation (-147.0385) and the combined vibrational mode and geometry parameters. The thought behind the combined evidence connects as follows: 1) Platinum seems to be re-establishing its coordination to the nitrogen in the ring from the vibrational mode could indicate once this bond is back in tact, its

90

strength could initiate the slightest shift of platinum towards the ring further inducing a closer pull to interact with the carbon ring. Additionally, as the leaving Cl$^-$ ion is migrating towards its optimized location in complex **E1**, its shift away from the ring would additional draw the platinum closer to avoid as much steric hindrance as possible. 2) Platinum is already interacting to the metalated carbon, and would only be defined as bonded to the nitrogen in the ligand L. Its overall large movement to re-establish coordination could be a sort of tug-a-war phenomena; and as the coordination species re-bond to platinum they will in-turn shift the further distanced species in closer interaction.

Upon optimization of complex **E2**, the mapping of the direct pathway involving re-aromatization was trialed with the newer complex (**figure 29**). This neb protectory not only confirmed that either direction results in nearly identical results, but can be seen in the structural parameters and energy of the transitions states too. **E2**-**P1** transition state (**figure 37b**) is only 0.19 kcal/mol lower in energy than **P1**-**E1**. While the noted difference in **E** complexes, the lower energy associating with the **E2** trial can come from the shorter traveling distance of the leaving group Cl$^-$ ion. This transition state also displayed the same movement in its vibrational mode as previously noted in **P1**-**E1**.

Indication of a possible intermediate step has been considered plausible as the transition from E to P involves a lot of disruption. Since the neb mapping performed used only 13 images between both trials, we may have overlooked a short-lived intermediate. In **figure 29**, moving from images 5 and 6, a small hump in the curve could suggest this species exist. The newest insight to the swapping of ligands may add in an additional step prior to re-establishing aromaticity. Conformation of this theory would require extensive computational tools to not only

increase the images mapped, but the largest relativistic effects noted so far from the disturbance

in all the coordinating ligands and platinum.

a. D1-E1   b. D1-E2
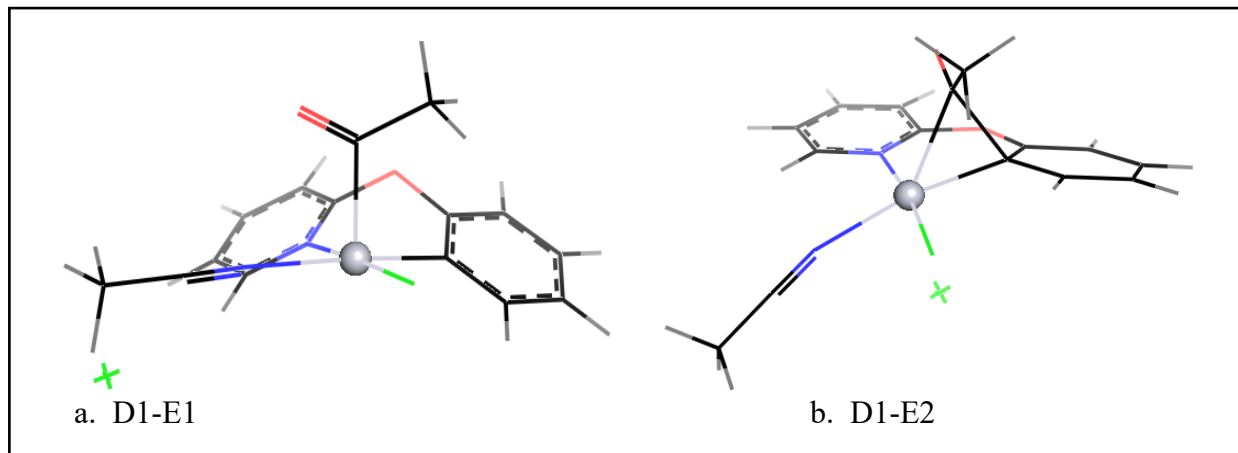
Figure 38ab. All Transition State Complexes between D1 and E located, Optimized and Confirmed through Vibrational Mode Analysis.

Table 16. Transition State Structures Between D and E complexes.

Bond Length (Å)	D-E1	D-E2
Pt - L	2.2189	2.1337
Pt - N	2.0604	2.0732
Pt – C_R	1.9823	2.0398
Pt - Cl_1	2.3294	2.3506
Pt - C_a	2.0492	2.271
Pt – Cl_2	5.1508	3.1548
C_a - C_R	2.9228	1.8578
C_a - Cl_2	6.3022	4.9877
Pt - C_{ox}	2.9184	2.958
Pt - C_{far}	4.2428	4.2361
Bond Angles (°)		
C_a - Pt - C_R	92.9	50.7
L - N - C_R - Cl	-0.7	-6.8

The reasonable shown transition state above is from the mapping from **D1-E2** (**figure 38b**). Two transition states are shown in **figure 38** for a few different points. The first transition state found from mapping **D1-E1** (**figure 38a**) produced a considerably unrealistic transition state. It's frequency calculation gave a borderline numerical noise value of -76.3233, and its structure is notable the same as complex **B**. From its vibrational mode analysis, the only movement seen is of thee ligand L's methyl group rotating. This not only discredits **D1-E1** transition state, but could also raise speculation that complex **B** does truly exist in the mapping towards complex **E** to further justify the 1,2-migration step in this proposed mechanism.

Prior to canceling out the possibility of this transition, complex **D1** to **E2** was simulated (**figure 27**). The smooth projected MEP lead to a refined transition state strongly confirmed as a first order saddle point (1st frequency value of -319.5134). A dimer optimization was performed and the obtained transition state seems to be the favorable 1,2-migration intermediate. The 3-membered ring formed seems to enable thee Pt-C bond dissociation to allow for the C-C bond formation. In addition to observation of thee vibration mode, the shift towards the C-C bond formation strongly displays the metalated carbon's sharp shift upward, which simultaneously pulls platinum in closer. From **table 16**, the noted Pt-C_R bond is well intact, so the sharp shift of the carbon ring upward would require a stronger pull on platinum's back-end. However, this backwards pull of platinum may be handicapped from the trans affect from the metalated carbon onto the lengthening Pt-N bond of ligand L. This may speculate complex **D** and **E** do not actually lie on the same MEP as well.

3.4 Conclusions

Several versions of the small steps within this overall mechanism were simulated in this investigation. To summarize the work, the confirmed steps are connected between all optimized structures and displayed in energy diagrams below. The diagrams associate to the relative energy in reference to complex **A1**. Optimized structure **A1** was the lowest energy structure out of all the optimized A complex's, and whose structural orientation had the chlorine pointing towards the direction it would go once dissociated from acetyl chloride.

Table 17. Data Used to Generate the Energetic Diagram in **Figure 39**.

A1 - TS(a2b1) - B2 - TS(b2e1) - E1 - TS(p1e1) - P			
basis set	Optimized ZPC-E (Hartree)	relative E (Hartree): $E - E(A_1)$	Relative E (kcal/mol)
A_1 ZPC - E	-1879.334449	0	0
TS_{A2B1} ZPC - E	-1879.299025	0.0354236	22.22862781
B_5 ZPC- E	-1879.311212	0.023237	14.58142663
TS_{B5-E} ZPC- E	-1879.279067	0.0553823	34.75289169
E_1 ZPC - E	-1879.309602	0.0248469	15.59165337
TS_{E1P} ZPC-E	-1879.277344	0.0571053	35.8340897
P_1 ZPC- E	-1879.352878	-0.0184285	-11.56404961
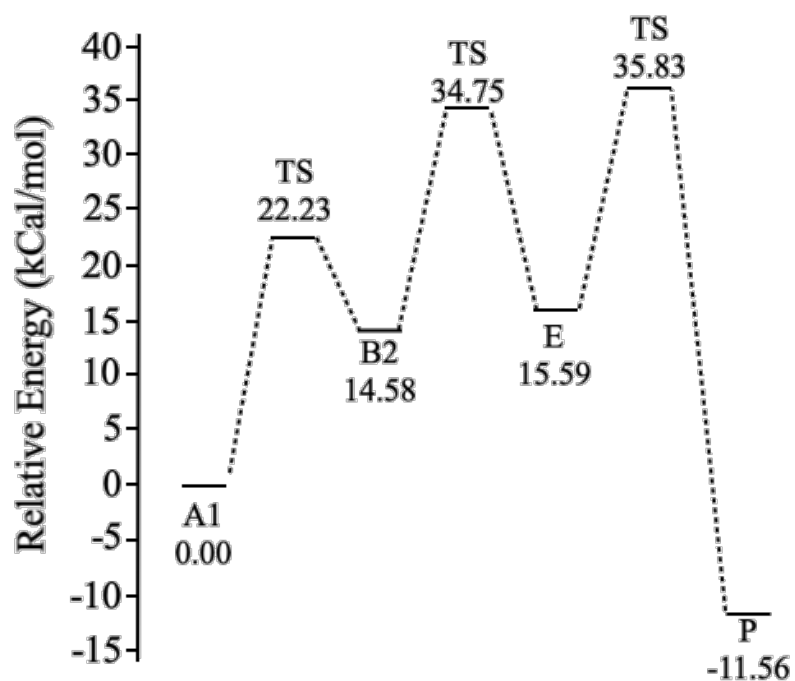
Figure 39. Energy Diagram A$_1$ → B$_2$ → E$_1$ → P$_1$

The numerical table in **table 17** can be visualized in the energy diagram in **figure 39**.

Noted from **table 17**, the transition state (**figure 31b**) following **A1** is from the mapping

performed from **A2-B1** (**figure 13**). This transition state is very comparable to the one attained

from the neb mapped by Dr. Bartolotti from **A3-B2**. It is also comparable to the reaction directly

between **A1** and **B1** (**figure 31a**). Transition state **A2-B1** in alignment to the either two options

shows an RMSD average of 0.788 (range of 0.779 – 0.797). The goal of choosing a transition

state connecting these two was to: 1) ensure the structures were reasonable to be assumed on the

same MEP, so in turn 2) less neb simulations needed to be added in. As the remaining species

connect in this diagram, the transitions states are the ones refined from the projected mapping of

the shown complex.

From the energy diagram in **figure 39**, it is clearly noted that the rate-determining step (RDS) occurs during the last step from **E → P**, with an energy barrier of 35.83 kcal/mol. This could be largely due to the ligand and chlorines coordinating position to platinum, and with further minimum optimization studies, the step may not hold true as the RDS. In precedent to investigating the overall C-H functionalization reaction, of the two steps involved we can denote the transformation of the Pt-C bond to a C-C bond is the RDS strictly in the sense of functionalization. The mechanism from **B** to **E** involves the 1,2-migration step, where a relatively stabilizing C-Pt bond is broken to form the desired C-C bond. This step shows a barrier of 34.75 kcal/mol, and would be notable competitive with the barrier traveling from **E-P** if complex **P** wasn't such a stable, low lying, energy species.

Alternative pathway to the one shown above would be seen by the insertion of complex **D** into the mechanism. In **table 18** the data used to generate the energy diagram in **figure 40** is shown. All relative energies are compared, as before, to complex **A1**.

Table 18. Data Used to Generate the Energetic Diagram in **Figure 40**.

| A1 - TS(a2b1) - B2 - TS(b2d) - D - TS(de2) - E2 - TS(E2) - P			
basis set	Optimized ZPC-E (Hartree)	relative E (Hartree): E - E(A_1)	Relative E (kcal/mol)
A_1 ZPC - E	-1879.334449	0	0
TS_{A2B1} ZPC - E	-1879.299025	0.0354236	22.22862781
B_2 ZPC- E	-1879.311212	0.023237	14.58142663
TS_{B2D} ZPC - E	-1879.31059	0.0238593	14.97192548
D ZPC- E	-1879.328965	0.0054842	3.441384858
TS_{DE2} ZPC- E	-1879.275282	0.0591667	37.12763675
E_2 ZPC- E	-1879.304761	0.0296879	18.62942444
TS_{E2P} ZPC-E	-1879.27765	0.0567988	35.64175819
P ZPC- E	-1879.352878	-0.0184285	-11.56404961
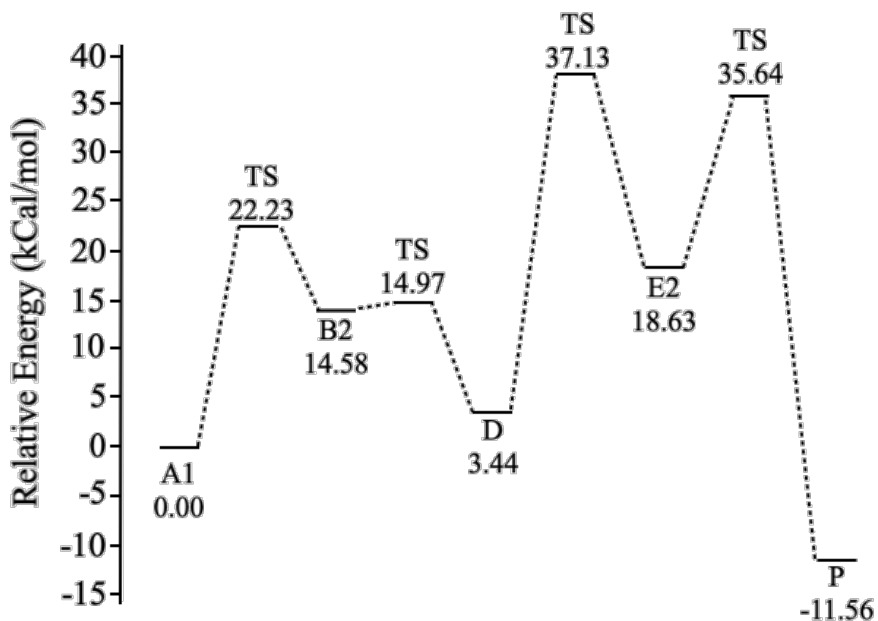
Figure 40. Energy Diagram $A_1 \rightarrow B_2 \rightarrow D \rightarrow E_2 \rightarrow P_1$

An alternate approach to the first mechanistic approach would to account for complex **D** being involved in the reaction between the 1,2 migration from complex **B** to **E**. The experimental environment is synthesizing these complexes in a solution with free chlorines. Therefore to assume that complex **B2** follows a chloride trapping to form the oxidative addition product **D** is very reasonable assumption. In turn, if this would to occur then the overall RDS is overall due to the 1,2-migration mechanism that follows from complex **D1** to **E2** (transition state in **figure 38b**). By the involvement of complex **E2** to achieve the more reasonable transition state between **D** and **E** species, it shines light onto the fact the system simulated may have chlorines optimized in numerous locations, with varying locations connecting. Since this study was performed in an implicit PCM model, it may be a worthwhile to investigation the use of explicit solvents.

Based on comparison of energy diagrams, following A $\rightarrow$ B $\rightarrow$ E $\rightarrow$ P is 1.30 kcal/mol lower in the over highest energy barrier to overcome, in addition to less steps involved. The Pt-catalyzed transformation process is shown to follow a 3 step process: (1) nucleophilic

substitution of the acyl group to form the five-coordinate acylplatinum complex **B**, (2) 1,2-migration of the acyl group from platinum to the metalated carbon to form a platinacyclpropane complex **E**, and (3) the dissociation of **E** or re-aromatization of the platinacyclopropoane through nucleophilic attack by the chloride ion to produce complex **P**.

REFERENCES

1) D. Balcells, E. Clot, O. Eisenstein, *Chem. Rev*. **2010**, *110*, 749-823.

2) R. G. Bergman, *Nature* **2007**, *446*, 391-393.

3) R. H. Crabtree, *J. Organomet. Chem.* **2004**, *689*, 4083-4091.

4) J. A. Labinger, J. E. Bercaw, *Nature* **2002**, *417*, 507-514.

5) A. E. Shilov, G. B. Shul'pin, *Chem. Rev.* **1997**, *97*, 2879-2932.

6) Labinger, J. A.; Bercaw, J. E. Nature 2002, 417, 507.

7) Ellman, J. C-H Functionalization, 2014.

8) a) A. E. Shilov, G. B. Shul'pin, *Chem. Rev.* **1997**, 97, 2879; b) Y. Guari, S. Sabo-Etienne, B. Chaudret, *Eur. J. Inorgo. Chem.* **1999**, 1047.

9) a) R. H. Crabtree, *Chem. Rev*. **1985**, 85, 245; b) F. Kakiuchi, S. Murai, *Top. Organomet. Chem.* **1999**, *3*, 47; c) R. H. Crabtree, *J. Chem. Soc. Dalton Trans*. **2001**, 2437; d) V. Ritleng, C. Sirlin, M. Pfeffer, *Chem. Rev*. **2002**, *102*, 1731; e) J. A. Labinger, J. E. Bercaw, *Nature* **2002**, *417*, 507.

10) Blanksby, S.J., Ellison, G.B. *Acc. Chem. Res.* **2003**, *36*, 255-263.

11) (a) F. W. Patureau and F. Glorius, *Angew. Chem., Int. Ed*., **2011**, *50*, 1977–1979; (b) H. Huang, X. Ji, W. Wu and H. Jiang, *Chem. Soc. Rev*., **2015**, *44*, 1155–1171; (c) J. Mo, L. Wang, Y. Liu and X. Cui, *Synthesis*, **2015**, *47*, 439–459.

12) Crabtree, R. H., J. *Chem. Soc., Dalton Trans*. **2001**, 2437-2450.

13) Dick, A. R.; Sanford, M. S., *Tetrahedron* **2006**, *62*, 2439-2463.

14) (a) Doyle, M. P., *Chem. Rev*. **1986**, *86*, 919-939; (b) Davies, H. M. L.; Beckwith, R. E. J., *Chem. Rev*. **2003**, *103*, 2861-2904; (c) Davies, H. M. L.; Manning, J. R., *Nature* **2008**, *451*,

417-424; (d) Doyle, M. P.; Duffy, R.; Ratnikov, M.; Zhou, L., *Chem. Rev.* **2010**, *110*, 704-724.

15) (a) Breslow, R.; Gellman, S. H., *J. Am. Chem. Soc.* **1983**, *105*, 6728-6729; (b) Du Bois, J., *Org. Process Res. Dev.* **2011**, *15*, 758-762; (c) Roizen, J. L.; Harvey, M. E.; Du Bois, J., *Acc. Chem. Res.* **2012**, *45*, 911-922.

16) (a) Shilov, A. E.; Shteinman, A. A., *Coord. Chem. Rev.* **1977**, *24*, 97-143

17) Hartwig, J. F.; Larsen, M. A., *ACS Central Science* **2016**, *2*, 281-292.

18) (a) Jazzar, R.; Hitce, J.; Renaudat, A.; Sofack-Kreutzer, J.; Baudoin, O., *Chem. Eur. J.* **2010**, *16*, 2654-2672; (b) Baudoin, O., *Chem. Soc. Rev.* **2011**, *40*, 4902-4911.

19) Labinger, J. A. *Chem Rev.* **2016**, *117,* 8483-8496.

20) Garnett, J. L.; Hodges, R. J. *J. Am. Chem. Soc.* **1967**, *89*, 4546− 4547.

21) Gol'dshleger, N. F.; Eskova, V. V.; Shilov, A. E.; Shteinman, A. A. *Zh. Fiz. Khim.* **1972**, *46*, 1353.

22) (a) Vidossich, P.; Ujaque, G.; Lledós, A. *Chem Commun.* **2012**, *48*, 1979-1981. (b) Zhu, H.; Ziegler, T. *J. Organomet. Chem.* **2006**, *691*, 4486-4497.

23) Crosby, S. H.; Clarkson, G. J.; Rourke, J. P. *J. Am. Chem. Soc.* **2009**, *131*, 14142-14143

24) Campora, J.; Lopez, J. A.; Palma, P.; Valerga, P.; Spillner, E.; Carmona, E. *Angew. Chem., Int. Ed.* **1999**, *38*, 147-151.

25) Keyes, L.; Wang, T.; Patrick, B. O.; Love, J. A. *Inorg. Chim. Acta* **2012**, *380*, 284−290.

26) Crespo, M.; Anderson, C. M.; Kfoury, N.; Font-Bardía, M.; Calvet, T. *Organometallics* **2012**, *31*, 4401−4404.

27) Niu, S.; Hall, M. B. *Chem. Rev.* **2000**, *100*, 353-405.

28) Hill, G.; Puddephatt, R. *Organometallics* **1997**, *17,* 1478− 1486.

29) Ellis, C.; Ess, D. *J. Org. Chem.* **2011**, *76*, 7180-7185.

30) Johnson, J. A.; Li, N.; Sames, D. *J. Am. Chem. Soc.* **2002**, *124*, 6900.

31) Lewars, E. G. *Computational Chemistry: Introduction to the Theory and Applications of Molecular and Quantum Mechanics*, 2nd ed., Springer, **2011**.

32) F. Jensen, *Introduction to Computational Chemistry,* 2nd ed., Wiley, **2007**.

33) Field, MJ.; Bash, PA.; Karplus, M. *Comp Chem.* **1990**, vol 11, No. 6, 700-733.

34) Warshel, A.; Levitt, M. *J. Mol. Biol.* **1976**, No. 103, 227–249.

35) C. J. Cramer, *Essentials of Computational Chemistry: Theories and Models,* Wiley, **2005**.

36) A. Szabo, N. S. Ostlund, *Modern Quantum Chemistry: Introduction to Advanced Electronic Structure Theory,* Dover Publications, New York, 1982.

37) Gilbert, A. Introduction to Computational Quantum Chemistry: Theory. *Lecture.*

38) Liehr, A. D. *Annals of Physics,* **1957**, *1*(3), 221–232.

39) Bunker, P. R.; Moss, R. E. *Molecular Physics***1977**, *33*(2), 417–424.

40) Libretexts. 10.1: The Born-Oppenheimer Approximation.

41) Mack, J. An Overview of Computational Chemistry. *Lecture.*

42) D. R. Hartree, "The wave mechanics of an atom with a non-Coulomb central field part I theory and methods". Proc. Camb. Philos. Soc. 1928, 24(01), 89-110.

43) V. Fock, "Näherungsmethode zur lösung des quantenmechanischen mehrkörperproblems". Z. Phys. 1930, 61(1-2), 126-148.

44) J. C. Slater, "Note on hartree's method". Phys. Rev. 1930, 35(2), 0210-0211.

45) P. Fulde, *The Independent-Electron Approximation. In: Electron Correlations in Molecules and Solids*, Springer Series in Solid-State Sciences, Vol 100, Springer, **1995**.

46) P. Atkins and J. de Paula. Atkins' Physical Chemistry. Oxford University Press, 9th edition, 2010.

47) D. P. Tew, W. Klopper, T. Helgaker, "Electron correlation: The many-body problem at the heart of chemistry". J. Comput. Chem. 2007, 28(8), 1307-1320.

48) K. Raghavachari, J. B. Anderson, "Electron correlation effects in molecules". J. Phys. Chem. 1996, 100(31), 12960-12973.

49) J. A. Pople, J. S. Binkley, R. Seeger, "Theoretical models incorporating electron correlation". Int. J. Quantum Chem. 1976, 10(S10), 1-19.

50) P.-O. Löwdin, "Quantum theory of many-particle systems. III. Extension of the HartreeFock scheme to include degenerate systems and correlation effects". Phys. Rev. 1955, 97(6), 1509.

51) J. C. Slater, "The self-consistent field and the structure of atoms". Phys. Rev. **1928**, 32(3), 0339-0348.

52) J. C. Slater, "The theory of complex spectra". Phys. Rev. **1929**, 34(10), 1293-1322.

53) (a) Pyykko, P. *Chem. Rev*. **1988**, *88(3)*, 563-594. (b) Pitzer, K. *Acc. Chem. Res*. **1979**, *12(8)*, 272- 276. (c) Kaltsoyannis, N. *J Chem Soc Dalton* **1997**, *1*, 1-11. (d) Pyykko, P.; Desclaux, J. *Acc. Chem. Res*. **1979**, *12(8)*, 276-281. (e) J. S. Thayer, "Relativistic effects and the chemistry of the heavier main group elements". In Relativistic methods for chemists (Eds.: M. Barysz, Y. Ishikawa), Springer Netherlands, Dordrecht, 2010, 63-97. (f) Pyykkö, P. *Adv. Quantum Chem*. **1978**, *11*, 353. (g) Pyykkö, P.; Snijders, J.; Baerends, E. *Chem. Phys. Lett*. **1981**, *83*, 432. (h) Pyykkö, P. *Relativistic theory of atoms and molecules*, **1986**. (i) Pyykkö, P. *ESF Commun*. **1993**, *28*, 20. (j) Pyykkö, P. *Relativistic theory of atoms and molecules II*, **1993**. (k) Pyykkö, P. *Relativistic theory of atoms and molecules III*, **2000**. (l) Pyykko, P. *Annu. Rev. Phys. Chem*. **2012**, *63(1)*, 45-64. (m) Pyykkö, P. *Chem. Rev*. **2012**, 112.

54) Kohn, W.; Sham, L. J. Physical Review 1965, 137, A1697.(prev 23)

55) Zhao, Y.; Truhlar, D. *Theor Chem Account* **2008**, *120*, 215-241.

56) Tirado-Rives, J.; Jorgenen, W. *J. Chem. Theory Comput.* **2008**, *4*, 297-306.

57) Xu, X.; Truhlar, D. *J. Chem. Theory Comput.* **2011**, *7 (9)*, 2766–2779.

58) (a) Chang, C.; Pelissier, M.; Durand, P. *Phys. Scr.* **1986**, *34(5)*, 394. (b) Faas, S.; Snijders, J.; Vanlenthe, J.; Vanlenthe, E.; Baerends, E. *Chem. Phys. Lett.* **1995**, *246(6)*, 632-640. (c) Van Lenthe, E.; Snijders, J.; Baerends, E. *J. Chem. Phys*. **1996**, *105(15)*, 6505.

59) Kim, Y.; Corchado, J.; Villa, J.; Xing, J.; Truhlar, D. *J. Chem. Phys.* **2000**, *112*, 2718.

60) van Duin, A.; Dasgupta, S.; Lorant, F.; Goddard III, W. *J. Phys. Chem*. A, **2001**, *105*, 9396.

61) Cossi, M.; Barone, V.; Cammi, R.; Tomasi, J. *Chem. Phys. Lett*. **1996**, *255*, 327.

62) (a) Benassi, R.; Ferrari, E.; Lazarri, S.; Spagnolo, F.; Saladini, M. *J. Mol. Struct.* **2008**, 168, 892. (b) Barone, V.; Crescenzi, O.; Improta, R. *Quantitative structure-activity relationships* **2002**, *105*, 21. (c) Sadlej, J.; Pecul, M.; Mennucci, B.; Cammi, R. *Continuum solvation models in chemical physics* **2007** Wiley, New York, p 125.

63) Merz, T.; Bierhance, G.; Flach, E.-C. *Physical Sciences Reviews* **2018**, *3*(11).

64) Henkelman, G.; Jónsson, H. *J. Chem. Phys*. **2000**, *113*, 9978.

65) (a) Henkelman, G.; Jónsson, H. *J. Chem. Phys.* **1999**, *111*, 7010. (b) Munro, L.; Wales, D. *Phys*. *Rev. B.* **1999**, *59*, 3969.

66) Trygubenko, S.; Wales, D. *J. Chem. Phys*. **2004**, *120*, 2082.

67) Henkelman, G.; Uberuaga, B.; Jónsson, H. *J. Chem. Phys*. **2000**, *113*, 9901.

68) Peng, C.; Schlegel, H. *Israel J. Chem.* **1993**, *33*, 449-454.

69) (a) Wales, D.; J. *Chem. Phys.* **1989**, *91*, 7002. (b)Tsai, C.; Jordan, K. *J. Phys. Chem.* **1993**, *97*, 11227.

70) Schlegel, H. B. *J. Comput. Chem.* **1982**, *3*, 214.

71) Gaussian 16, Revision B01 , M. J. Frisch, G. W. Trucks, H. B. Schlegel, G. E. Scuseria, M. A. Robb, J. R. Cheeseman, G. Scalmani, V. Barone, G. A. Petersson, H. Nakatsuji, X. Li, M. Caricato, A. V. Marenich, J. Bloino, B. G. Janesko, R. Gomperts, B. Mennucci, H. P. Hratchian, J. V. Ortiz, A. F. Izmaylov, J. L. Sonnenberg, D. Williams-Young, F. Ding, F. Lipparini, F. Egidi, J. Goings, B. Peng, A. Petrone, T. Henderson, D. Ranasinghe, V. G. Zakrzewski, J. Gao, N. Rega, G. Zheng, W. Liang, M. Hada, M. Ehara, K. Toyota, R. Fukuda, J. Hasegawa, M. Ishida, T. Nakajima, Y. Honda, O. Kitao, H. Nakai, T. Vreven, K. Throssell, J. A. Montgomery, Jr., J. E. Peralta, F. Ogliaro, M. J. Bearpark, J. J. Heyd, E. N. Brothers, K. N. Kudin, V. N. Staroverov, T. A. Keith, R. Kobayashi, J. Normand, K. Raghavachari, A. P. Rendell, J. C. Burant, S. S. Iyengar, J. Tomasi, M. Cossi, J. M. Millam, M. Klene, C. Adamo, R. Cammi, J. W. Ochterski, R. L. Martin, K. Morokuma, O. Farkas, J. B. Foresman, and D. J. Fox, Gaussian, Inc., Wallingford CT, 2016.

72) Labinger, J. A.; Bercaw, J. E. *Nature* **2002**, *417*, 507-514.

73) Bergman, R. G. *Nature*, **2007**, *446*, 391-393.

74) (a) Chatt, J.; Davidson, J. *J. Chem. Soc.* **1965**, 843-855. (b) Goldberg, A.; Goldman, K *ACS Symposium Series* **2004**, 885.

75) Periana, R. A.; Taube, D. J.; Gamble, S.; Taube, H.; Satoh, T.; Fujii, H. *Science* **1998**, *280*, 560-564.

76) Chen, H.; Schlechet, S.; Semple, T. C.; Hartwig, J. F. *Science* **2000**, *287*, 1995-1997

77) Mkhalid, I. A. I.; Barnard, J. H.; Marder, T. B.; Murphy, J. M.; Hartwig, J. F. *Chem. Rev.* **2010**, *110*, 890-931.

78) McAteer, D.; Javed, E.; Yumin, L.; *Huo, S. *Org. Lett.* **2017**, *19*, 1606-1609.

79) Wu, X.-F. *Chem. - Eur. J.* **2015**, *21*, 12252−12265.

80) (a) Fang, P.; Li, M.; Ge, H. *J. Am. Chem. Soc.* **2010**, *132*, 11898− 11899. (b) Yang, Z.; Chen, X.; Liu, J.; Gui, Q.; Xie, K.; Li, M.; Tan, Z. *Chem. Commun.* **2013**, *49*, 1560−1562. (c) Yao, J.; Feng, R.; Wu, Z.; Liu, Z.; Zhang, Y. *Adv. Synth. Catal.* **2013**, *355*, 1517−1522. (d) Miao, J.; Ge, H. *Org. Lett.* **2013**, *15*, 2930−2933.

81) Alfonso, D. R.; Jordan, K. D. J. *Comput. Chem.* **2003**, *24*, 990−6.

82) For ground-breaking work, see: Murai, S.; Kakiuchi, F.; Sekine, S.; Tanaka, Y.; Kamatani, A.; Sonoda, M.; Chatani, N. Nature 1993, 366, 529−531.

83) For selected reviews, see: (a) Dyker, G. Angew. Chem., Int. Ed. 1999, 38, 1698−1712. (b) Chen, X.; Engle, K. M.; Wang, D.-H.; Yu, J.- Q. Angew. Chem., Int. Ed. 2009, 48, 5094−5115. (c) Daugulis, O.; Do, H.-Q.; Shabashov, D. Acc. Chem. Res. 2009, 42, 1074−1086. (d) Lyons, T. W.; Sanford, M. S. Chem. Rev. 2010, 110, 1147−1169. (e) Colby, D. A.; Bergman, R. G.; Ellman, J. A. Chem. Rev. 2010, 110, 624−655. (f) Sun, C.-L.; Li, B.-J.; Shi, Z.-J. Chem. Rev. 2011, 111, 1293−1314. (g) Ackermann, L. Chem. Rev. 2011, 111, 1315−1345. (h) Engle, K. M.; Mei, T.-S.; Wasa, M.; Yu, J.-Q. Acc. Chem. Res. 2012, 45, 788−802. (i) Arockiam, P. B.; Bruneau, C.; Dixneuf, P. H. Chem. Rev. 2012, 112, 5879−5918. (j) Rouquet, G.; Chatani, N. Angew. Chem., Int. Ed. 2013, 52, 11726−11743. (k) Kakiuchi, F.; Kochi, T.; Murai, S. Synlett 2014, 25, 2390−2414. (l) Zhang, X.-S.; Chen, K.; Shi, Z.-J. Chem. Sci. 2014, 5, 2146−2159. (m) Zhang, M.; Zhang, Y.; Jie, X.; Zhao, H.; Li, G.; Su, W. Org. Chem. Front. 2014, 1, 843−895.

84) For a previous report of platinum-catalyzed ortho-silylation of aromatic aldimines and related reactions, see: (a) Williams, N. A.; Uchimaru, Y.; Tanaka, M. J. Chem. Soc., Chem.

Commun. 1995, 1129− 1130. (b) Tsukada, N.; Hartwig, J. F. J. Am. Chem. Soc. 2005, 127, 5022−5023.

85) For Pt-catalyzed sp3 C−H functionalizations, see: (a) Periana, R. A.; Taube, D. J.; Gamble, S.; Taube, H.; Satoh, T.; Fujii, H. Science 1998, 280, 560−564. (b) Yang, S.; Li, Z.; Jian, X.; He, C. Angew. Chem., Int. Ed. 2009, 48, 3999−4001.

86) Jónsson, H.; Mills, G.; Jacobsen, K. (**1998**) Nudged elastic band method for finding minimum energy paths of transitions. Classical and Quantum Dynamics in Condensed Phase Simulations: pp. 385-404.

87) Dassault Systèmes BIOVIA, Marerial Studios, 4.1.1, San Diego: Dassault Systèmes, 2008.

88) Gaussian 16, Revision B.01, Frisch, M. J.; Trucks, G. W.; Schlegel, H. B.; Scuseria, G. E.; Robb, M. A.; Cheeseman, J. R.; Scalmani, G.; Barone, V.; Petersson, G. A.; Nakatsuji, H.; Li, X.; Caricato, M.; Marenich, A. V.; Bloino, J.; Janesko, B. G.; Gomperts, R.; Mennucci, B.; Hratchian, H. P.; Ortiz, J. V.; Izmaylov, A. F.; Sonnenberg, J. L.; Williams-Young, D.; Ding, F.; Lipparini, F.; Egidi, F.; Goings, J.; Peng, B.; Petrone, A.; Henderson, T.; Ranasinghe, D.; Zakrzewski, V. G.; Gao, J.; Rega, N.; Zheng, G.; Liang, W.; Hada, M.; Ehara, M.; Toyota, K.; Fukuda, R.; Hasegawa, J.; Ishida, M.; Nakajima, T.; Honda, Y.; Kitao, O.; Nakai, H.; Vreven, T.; Throssell, K.; Montgomery, J. A., Jr.; Peralta, J. E.; Ogliaro, F.; Bearpark, M. J.; Heyd, J. J.; Brothers, E. N.; Kudin, K. N.; Staroverov, V. N.; Keith, T. A.; Kobayashi, R.; Normand, J.; Raghavachari, K.; Rendell, A. P.; Burant, J. C.; Iyengar, S. S.; Tomasi, J.; Cossi, M.; Millam, J. M.; Klene, M.; Adamo, C.; Cammi, R.; Ochterski, J. W.; Martin, R. L.; Morokuma, K.; Farkas, O.; Foresman, J. B.; Fox, D. J. Gaussian, Inc., Wallingford CT, 2016.

89) Gaussian 09, Revision A.02, M. J. Frisch, G. W. Trucks, H. B. Schlegel, G. E. Scuseria, M. A. Robb, J. R. Cheeseman, G. Scalmani, V. Barone, G. A. Petersson, H. Nakatsuji, X. Li, M. Caricato, A. Marenich, J. Bloino, B. G. Janesko, R. Gomperts, B. Mennucci, H. P. Hratchian, J. V. Ortiz, A. F. Izmaylov, J. L. Sonnenberg, D. Williams-Young, F. Ding, F. Lipparini, F. Egidi, J. Goings, B. Peng, A. Petrone, T. Henderson, D. Ranasinghe, V. G. Zakrzewski, J. Gao, N. Rega, G. Zheng, W. Liang, M. Hada, M. Ehara, K. Toyota, R. Fukuda, J. Hasegawa, M. Ishida, T. Nakajima, Y. Honda, O. Kitao, H. Nakai, T. Vreven, K. Throssell, J. A. Montgomery, Jr., J. E. Peralta, F. Ogliaro, M. Bearpark, J. J. Heyd, E. Brothers, K. N. Kudin, V. N. Staroverov, T. Keith, R. Kobayashi, J. Normand, K. Raghavachari, A. Rendell, J. C. Burant, S. S. Iyengar, J. Tomasi, M. Cossi, J. M. Millam, M. Klene, C. Adamo, R. Cammi, J. W. Ochterski, R. L. Martin, K. Morokuma, O. Farkas, J. B. Foresman, and D. J. Fox, Gaussian, Inc., Wallingford CT, 2016.